NAWC-TR-99-

ADAPTIVE RECONFIGURABLE CONTROL BASED ON A REDUCED ORDER SYSTEM IDENTIFICATION FOR FLUTTER AND AEROSERVOELASTIC INSTABILITY SUPPRESSION

C. NAM
P.C. CHEN
D.D. LIU
ZONA Technology, Inc.
7430 E. Stetson Drive, Ste. 205
Scottsdale, AZ 85251-3540

R. M. YURKOVICH
J. URNES
The Boeing Company
P.O. Box 516
St Louis, Mo. 63166-0516

JUNE 2000

PHASE I FINAL REPORT FOR THE PERIOD NOV 1999 - MAY 2000

NAVAL AIR WARFARE CENTER AIRCRAFT DIVISION
HWY 547, BUILDING 129
LAKEHURST NJ 08733-5082

REPORT DOCUMENTATION PAGE

Form Approved
OMB No. 0704-0188

1. AGENCY USE ONLY (*Leave Blank*)	2. REPORT DATE	3. REPORT TYPE AND DATES COVERED
	19 JUN 2000	FINAL 12 MAY 1999 – 12 NOV 2000

4. TITLE AND SUBTITLE
ADAPTIVE RECONFIGURABLE CONTROL BASED ON A REDUCED ORDER SYSTEM IDENTIFICATION FOR FLUTTER AND AEROSERVOELASTIC INSTABILITY SUPPRESSION
PHASE I, FINAL REPORT

5. FUNDING NUMBERS
C N68335-00-C-0126
PR N68335-9307-0778
JO C000033874

6. AUTHOR(S)
C. Nam, P. C. Chen, and D. D. Liu, ZONA Technology, Inc.;
R. Yurkovich and J. Urnes, The Boeing Company/St. Louis

7. PERFORMING ORGANIZATION NAME(S) AND ADDRESS(ES)
ZONA Technology, Inc.
7434 E. Stetson Drive, Suite 205
Scottsdale, AZ 85251
Tel 480-945-9988 / Fax 480-945-6588

8. PERFORMING ORGANIZATION REPORT NUMBER
ZONA 00-19

9. SPONSORING/MONITORING AGENCY(S) AND ADDRESS(ES)
Naval Air Warfare Center Aircraft Division
Contracts Division (Code 25223DV)
Hwy 547, Building 129
Lakehurst, NJ 08733-5082
POC: Roger A. Burton, Tel 301-757-0858 / Fax 301-342-7607

10. SPONSORING/MONITORING AGENCY REPORT NUMBER

11. SUPPLEMENTARY NOTES

12a. DISTRIBUTION/AVAILABILITY STATEMENT
APPROVED FOR PUBLIC RELEASE; DISTRIBUTION UNLIMITED.

12b. DISTRIBUTION CODE

13. ABSTRACT (*Maximum 200 words*)

This report documents the design of a reconfigurable adaptive control (RAC) system for flutter/aeroservoelasticity (ASE) instability suppression of battle-damaged aircraft and limit cycle oscillation (LCO) suppression of aircraft/store configurations. With the F/A-18 as a baseline aircraft, rapid suppression of its critical damage/flutter and LCO (at 5.6 and 8.8 Hz) has been successfully demonstrated through eight cases of numerical simulations studied. The developed RAC system is a modular control design in that the flutter/LCO control can readily be combined with the rigid-body flight (RBF) control, thereby minimizing the impact on the existing flight control system for retrofit. The RAC system consists of a newly developed on-line modal parameter estimation (MPE) for system identification and on-line modified model-following reconfigurable (MMFR) algorithm for rapid flutter/LCO control (0.2 and 0.8 sec). A massive screening technique using an expedient nonlinear unsteady transonic method (ZTAIC) to generate plant matrices permits efficient identification of critical damage cases of flutter/ASE instability. Reduced-order techniques using proper orthogonal decomposition (POD) and minimum state (MIST) methods reduce the system to seven states. This allows the on-line algorithm to be operated within fractions of one second. The number of sensor locations are minimized to two at wing-tip for flutter/LCO control; and to four with two additional existing sensors in the fuselage for LCO/RBF dynamic control. Effective control surfaces for all cases considered are found to be the aileron and the trailing-edge flap rather than the leading edge flap. Essential tasks of phase II will be performed jointly with Boeing/St Louis with emphasis on nonlinear control analysis including actuator loading, control surface rates, 80Hz software update and software analysis for implementing LCO and flutter controllers in the FSFCC.

14. SUBJECT TERMS
Adaptive Reconfigurable Control, Battle Damaged Structure, Wing/Store Limit Cycle Oscillation (LCO), Flutter/ASE/LCO Suppression, Reduced-Order Plant Matrices, Modular ASE Controller

15. NUMBER OF PAGES
74

16. PRICE CODE

17. SECURITY CLASSIFICATION OF REPORT	18. SECURITY CLASSIFICATION OF THIS PAGE	19. SECURITY CLASSIFICATION OF THIS ABSTRACT	20. LIMITATION OF ABSTRACT
UNCLASSIFIED	UNCLASSIFIED	UNCLASSIFIED	SAR

FOREWORD

This Phase I SBIR final technical report entitled "*Adaptive Reconfigurable Control Based on a Reduced Order System Identification for Flutter and Aeroservoelastic Instability Suppression,*" has been prepared by ZONA Technology, Inc. (ZONA), with the participation of The Boeing Company (Boeing), St. Louis, MO, under contract number N68335-00-C-0126, sponsored by the Naval Air Warfare Center Aircraft Division (NAWCAC), Lakehurst, NJ. This report presents the findings as of May 17, 2000, from a research and development program begun November 17, 1999.

Dr. Changho Nam of ZONA was the Principal Investigator, Mr. P.C. Chen and Dr. D.D. Liu of ZONA were co-principal investigators; Mr. Rudy Yurkovich and Mr. Jim Urnes of Boeing/St. Louis were co-investigators of the ZONA team. Mr. Roger A. Burton of NAWCAD, (Code 4.3.2.6) was the Government Technical Monitor. Professor Marc Bodson of the University of Utah was the consultant. The authors thank Dr. Rick Lind and Mr. Marty Brenner of NASA/Dryden for their technical support. They also thank Mr. Roger Burton and Dr. Marc Steinberg of NAVAIR for their valuable comments and suggestions throughout the course of this development.

This report is CDRL Item 0001AF and documents the entire work under the Phase I effort. It is published for the dissemination of technical information. The findings and conclusions are those of the authors and do not necessarily represent the views of the United States Government. Distribution of this report shall be in accordance with the Distribution Statement of the Report Documentation page found on the cover hereof.

TABLE OF CONTENTS

TABLE OF CONTENTS (continued)

ACRONYMS

AIL	Aileron
ASE	Aeroservoelasticity
CFL3D	High-level computational fluid dynamics code by NASA (Ref 19)
FEM	Finite Element Model
FSFCC	Fleet Support Flight Control Computer
ILEF	Inboard Leading Edge Flap
LCO	Limit Cycle Oscillation
MATLAB	Matrix Laboratory (An interactive system and programming language for general scientific and technical computation.)
MIST	Minimum State (code by Karpel – Refs 23, 24)
MMFR	Modified Model-Following Reconfigurable (algorithm)
MPE	Modal Parameter Estimation (algorithm)
NASTRAN	Structural FEM software product of MSC
OLEF	Outboard Leading Edge Flap
POD	Proper Orthogonal Decomposition (a rigorous reduced-order technique – Ref 20)
RAC	Reconfigurable Adaptive Control
RBF	Rigid Body Flight (dynamics or control)
TEF	Trailing Edge Flap
ZAERO	ZONA's aeroelasticity and unstable aerodynamic software system covering all Mach ranges including ZONA6, ZONA7, ZTAIC and ZONA7U for complex aircraft configuration with external stores (Ref 6-10)
ZONA	ZONA Technology, Inc.
ZONA6	Generates unsteady subsonic aerodynamics for complex aircraft configuration with external stores (Ref 6)
ZTAIC	ZONA's Transonic Aerodynamic Influence Coefficient code; Generates unsteady transonic aerodynamics for complex aircraft configuration (Ref 7)

SECTION 1

INTRODUCTION

This final technical report describes work by ZONA Technology, Inc. (ZONA) under an SBIR Phase I contract N68335-9387-0778, entitled "*Adaptive Reconfigurable Control Based on a Reduced-Order System Identification for Flutter and Aeroservoelastic Instability Suppression*".

The overall Phase I technical objective is to design an adaptive reconfigurable control system and demonstrate its feasibility for flutter and aeroservoelastic (ASE) instability as well as limit cycle oscillation (LCO) suppression.

The F/A-18 is selected as a baseline aircraft, and the specific objectives are to:

- Model and parameterize different types of failure, structural damage and for a wide range of store configurations
- Develop an efficient on-line system identification of flutter, ASE instability and Limit Cycle Oscillation (LCO)
- Design a fast and robust adaptive control system for flutter, ASE and LCO suppression
- Combine the flexible and rigid body systems and demonstrate the viability in the control algorithms and stability, robustness and performance of the combined closed-loop system.

In this Phase I effort, we have accomplished the following:

- Designed optimum sensor locations using a short-time Fourier analysis technique (2 sensors at the wing tip and 2 sensors on the fuselage)
- Developed a new recursive system identification algorithm called Modal-based Parameter Estimation (MPE) for flexible system identification (converged time within 0.2 sec)
- Developed a new adaptive reconfigurable control system called Modified Model-Following Reconfigurable (MMFR) Control for fast and robust flutter/ASE/LCO instability suppression (converged time within 0.8 sec)
- Combined the flexible system with the rigid body flight dynamic system for real-time simulation using MATLAB/SIMULINK

1.1 Background

Modern combat aircraft are required to achieve aggressive maneuverability and high agility performance, while maintaining handling qualities over a wide range of flight conditions. These design goals tend to result in more flexible and less inherently stable aircraft. In the presence of system failures, battle damage, and other disturbance uncertainties, aircraft instabilities related to rigid body motion, flutter and aeroelastic modes with control feedback (aeroservoelastic instability) are likely to occur individually or collectively. The purpose of a reconfigurable flight control system is to obtain greater survivability for damaged aircraft undergoing these event-driven instabilities. Such instabilities call for the challenging design of an efficient, fast system

identification algorithm and an effective fault tolerant controller. In addition, reconfigurable flight control systems usually reduce the need for other forms of reliability improvement features such as redundant actuators. Thus, proved maintainability and reduced cost are expected to result from this technology. Clearly, reconfiguration is a desirable flight control system feature for current aircraft application and for next-generation aircraft design.

1.2 Damage/Failure Induced Flutter and Aeroservoelastic Instability

In September 1997, a USAF F-117A stealth fighter crashed at a Baltimore air show due to violent oscillations of the left wing which broke off 2.5 ft inboard of the elevon (Ref 1, AW&ST Sep. 22, p. 30). In the accident report, it was found that several fasteners used to attach the elevon hydraulic actuator to local wing structure were missing. The disappearance of these fasteners reduced the actuator-to-elevon stiffness, which had been found earlier to cause elevon-wing flutter. This accident clearly indicates that a structural failure as such could result in a catastrophic flutter. This kind of structural failure can originate from poor maintenance or a fatigue problem, but a similar type of structural failure can also be caused by battle damage as well as a system failure.

In general, aeroelastic instabilities including flutter can be induced by control system failure and/or structural failure caused by battle damage. When structural damage occurs, the shifts in vibration frequencies and gains can cause closed-loop instabilities that ultimately result in a critical types of limit cycle oscillations. These oscillations may cause further structural degradation and even the collapse of the airframe. This type of problem is commonly known as an aeroservoelastic (ASE) instability. Unlike the rigid body flight instability, the ASE instability, including flutter as a special case, derives from the close coupling of the structures, unsteady aerodynamic and the flight control system. The ASE instability occurs in the higher frequency range; hence, it must be suppressed within a much shorter time period than that to control the rigid body fight instability.

1.3 Limit Cycle Oscillation (LCO) of Wing with External Stores

Limit Cycle Oscillation (LCO) has been a persistent problem on several current fighter aircrafts and is generally encountered with external store configurations. Denegri (Ref 2) provided a detailed description of the aircraft/store LCO phenomenon. Norton (Ref 3) gave an excellent overview of LCO of fighter aircraft carrying external stores and its sensitivity to store carriage configuration and mass properties.

LCO can be characterized as sustained periodic oscillations which neither increase or decrease in amplitude over time for a given flight condition. Using a refined aerodynamic model of the aircraft and stores, ZONA (Chen, Sarhaddi and Liu – Ref 4) has shown that wing/store LCO is a post-flutter phenomenon whenever the flutter mode contains low unstable damping. This type of flutter mode is called "*hump mode*". Since the aircraft structure usually contains structural nonlinearity such as friction damping, this amplitude-dependent friction damping can stop the growth of amplitude (due to flutter), thus the structural system would result in steady-state

oscillation. This is known as LCO. By contrast, a typical flutter mode is a result of growth of amplitude largely due to destabilizing negative aerodynamic damping, hence a drastic increase in damping beyond the neutral stability point, or the flutter point (g = 0). A typical flutter mode and hump mode are shown in Figure 1.1.

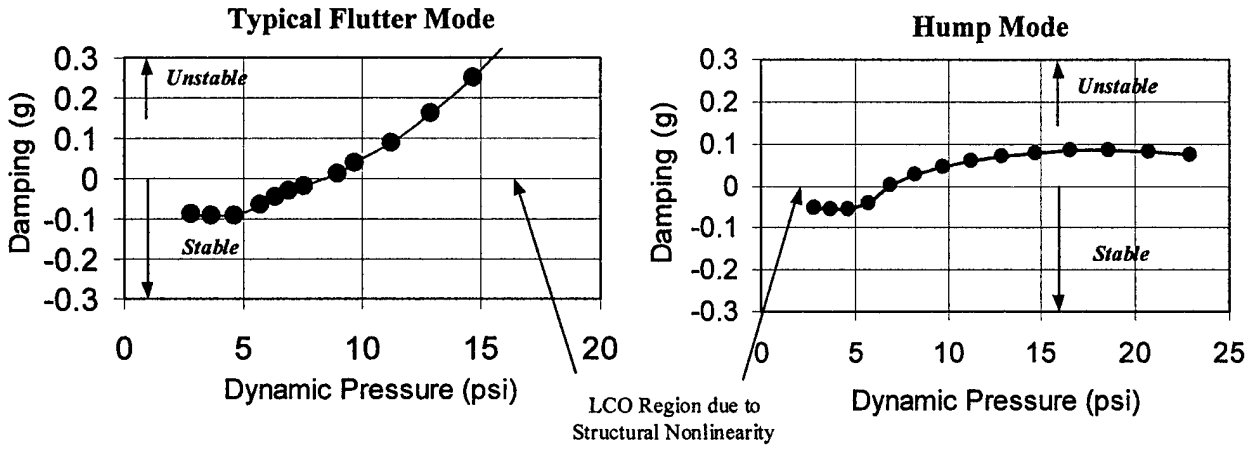

Figure 1.1 Typical Flutter Mode and Hump Mode by Flutter Analysis

Admitting nonlinear friction damping, Denegri (Ref 5) also showed consistent trends that hump mode can be used to correlate the flutter solutions with LCO flight test data of F-16's. Since the structural characteristic varies for different aircraft/store configurations, it is unlikely that the fixed-gain type of control system would work for wing/store LCO suppression in general. It appears that an adaptive controller with an online system identification process would be most appropriate for LCO suppression of a wide range of aircraft/store configurations.

1.4 Technical Issues and Challenges

Active suppression of an aeroelastic/aeroservoelastic system with changing parameters presents challenging problems to be resolved. Several pertinent technical issues are addressed as follows.

- *Real-Time Adaptive Control for a Flexible-Dynamic System*

  Since a wide range of aircraft/store configurations and system failure/damaged cases represent the plant with time varying or changing parameters, it is necessary to develop an unplanned control algorithm that does not require an accurate prior knowledge of the plant to be controlled in real time. A violent flutter will induce a rapidly growing amplitude. Thus a conservative estimate of the structural failure time should be a few cycle of oscillation beyond flutter onset. This would restrict a control elapse time to be no more than one second.

- *System Identification of Flexible System*

  A flutter solution usually derives from many structural modes. Hence, the number of parameters for flutter analysis in its system identification is many times greater than that of a rigid-body system. This renders the system identification problem for flutter suppression much more difficult to handle. Identification of flexible modes requires the design of optimum sensor locations and a robust system identification algorithm.

- *Transonic Unsteady Aerodynamics of Fighters with External Stores*

  The aerodynamics required for rigid-body flight dynamics of a flight vehicle can be usually obtained by wind-tunnel testing. The aeroelastic and aeroservoelastic responses of a fighter with stores require no accurate prediction of unsteady aerodynamics. In the transonic flight regime, nonlinear unsteady transonic aerodynamics for a flight vehicle should be solved by accurate yet efficient computational methods (codes). Current high-level Computational Fluid Dynamics (CFD) methods such as a Navier-Stokes solver is limited by grid generation procedure and computer capacity; hence their capability is confined to problems with simple geometry. For fighters with external stores, it is proven that CFD method would be impractical to generate useful unsteady transonic aerodynamic data in terms of engineering set up (grid generation) time and computing time. For this reason, a more efficient transonic unsteady method (code) is sought.

- *ASE System Matrix Generation*

  Accurate representation of an aeroelastic/aeroservoelastic system normally requires many structural modes, typically up to 40 modes or more for the whole aircraft structure. For real time control, it is necessary to largely reduce the size of the plant matrices while still maintaining the key characteristics of the system. Furthermore, the ASE system matrices must include both rigid-body and flexible modes in the plant, control system, and the gust response so that its closed-loop ASE control system can handle the rigid-body flight dynamics with proper flexible mode coupling.

1.5 Required Software Tools

Three engineering disciplines in terms of software tools are employed for the present study, namely MSC/NASTRAN, ZAERO and MATLAB. The functionality of each software tool and the interrelationship between them are depicted in Figure 1.2. The MSC/NASTRAN is used to perform the structural finite element (FEM) analysis and generate the generalized mass and stiffness matrices as well as mode shapes of the aircraft structure. MATLAB is employed to develop the system identification and adaptive control algorithm interactively. The real time simulation tool box SIMULINK of MATLAB is used to perform real time simulation of the closed-loop system and to assess its robustness, stability and performance. ZAERO is a ZONA commercialized software system that integrates the essential disciplines required by aeroelastic and aeroservoelastic design/analysis.

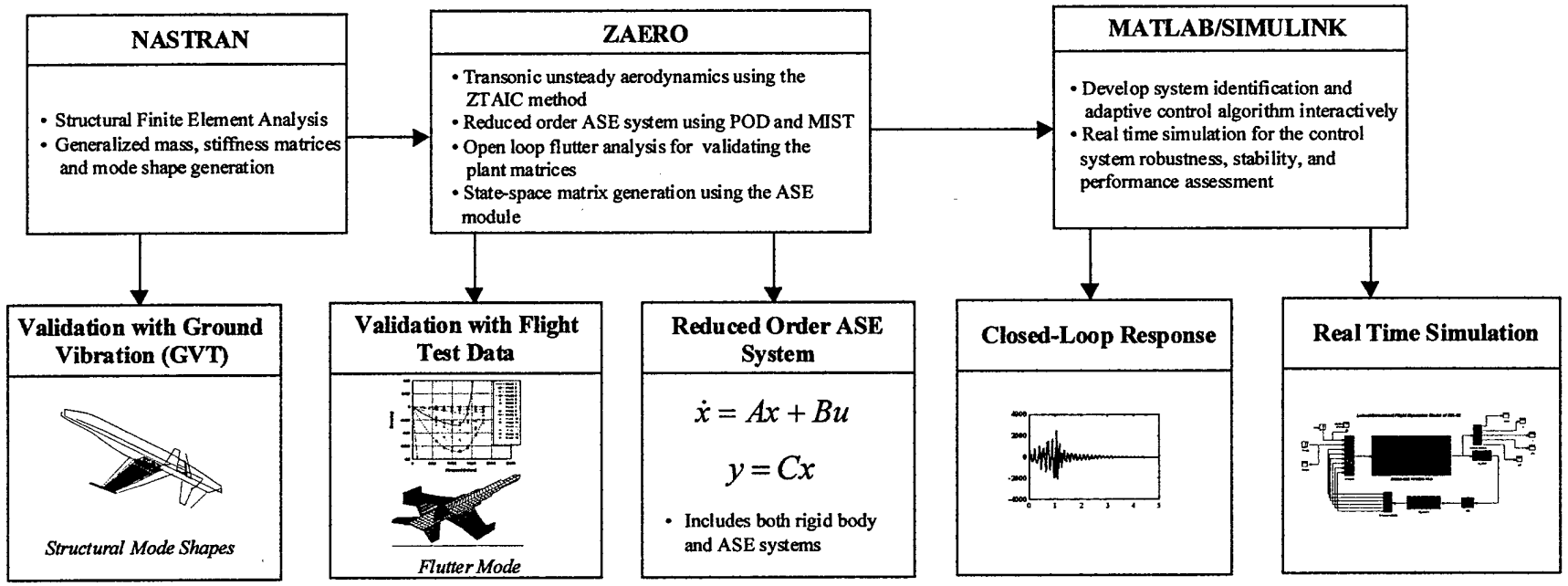

Figure 1.2 Required Software Tools

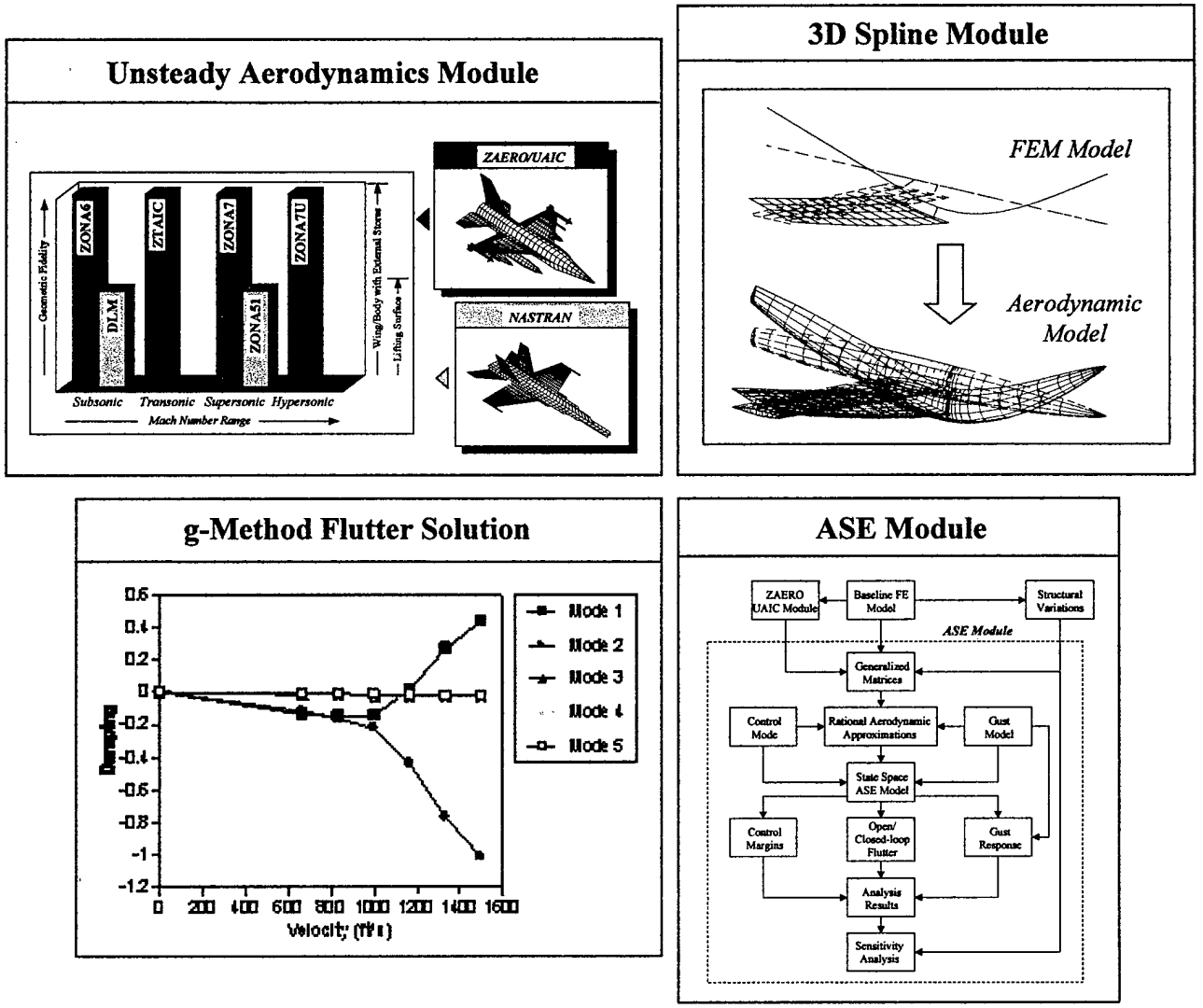

Figure 1.3 Four Major Modules of ZAERO

Figure 1.3 shows the four major modules of ZAERO. The unsteady aerodynamic module consists of four methods covering the entire Mach number range; ZONA6 (Ref 6), ZTAIC (Ref 7), ZONA7 (Ref 8) and ZONA7U (Ref 9) for subsonic, transonic, supersonic and hypersonic unsteady aerodynamics, respectively.

Since aircraft/store LCO usually occurs in the transonic flight conditions, the nonlinear ZTAIC (ZONA's Transonic Aerodynamic Influence Coefficient) method is selected to generate the transonic unsteady aerodynamics. The nonlinear ZTAIC method solves the transonic perturbation potential equation based on a "*steady aerodynamic background flow*" that is externally provided by options of CFD solutions or wind tunnel measured data.

The 3D spline module provides the displacement and force transferal between the structural FEM and the aerodynamic models. An exact and robust method, the g-method flutter solution technique (Ref 10) computes the true aerodynamic damping that is essential for predicting accurate "*hump mode*" for LCO correlation.

The ASE module is based on state-space formulations. The structure is represented by a set of baseline normal modes serving as generalized coordinates. The unsteady aerodynamic forces are represented by minimum-state rational approximations of the ZAERO module generated transcendental frequency domain generalized force coefficient matrices. The control system is represented by a state-space realization of a user-defined series of polynomial transfer functions.

A gust filter is defined such that a white-noise input produces an approximation of either Dryden's or von Kalman's power spectral density of atmospheric continuous gusts. The stability analysis and constraints are based on root-loci curves, Nyquist curves and transfer-function singular values in the frequency domain. The gust response analysis and sensitivities are based on the stochastic Lyapunov formulation. There are several options for the reduction of the order of the state-space equations. These options allow a combination of modal truncation, static residualization and dynamic residualization. The ASE module is applicable to open loop as well as closed loop systems. The total ASE module flow chart is presented in Figure 1.4.

1.6 Overall Design Strategy

Figure 1.5 presents a block diagram depicting the overall design strategy of the Phase I effort for an adaptive reconfigurable control design. This block diagram consists of 9 blocks that can be further divided into two parts; the off-line analysis (Blocks 1 ~ 3) and the on-line control (Blocks 4 ~ 9).

The objective of the off-line analysis is to generate a reduced order system matrix database that can enhance the efficiency of the on-line adaptive control algorithm. NASTRAN and ZAERO will be used as the essential software system for the off-line analysis. Three blocks are involved in the off-line analysis: *the off-line flutter/ASE instability screening* (Block 1) to identify all critical cases of flutter/ASE instability and LCO prediction of various aircraft/store configurations; *the optimum sensor location & database of critical modes* (Block 2) to select optimum sensor locations and collect critical modes; and *reduced-order plant equations* (Block 3) to generate the reduced-order system matrix database by a Proper Orthogonal Decomposition (POD) technique.

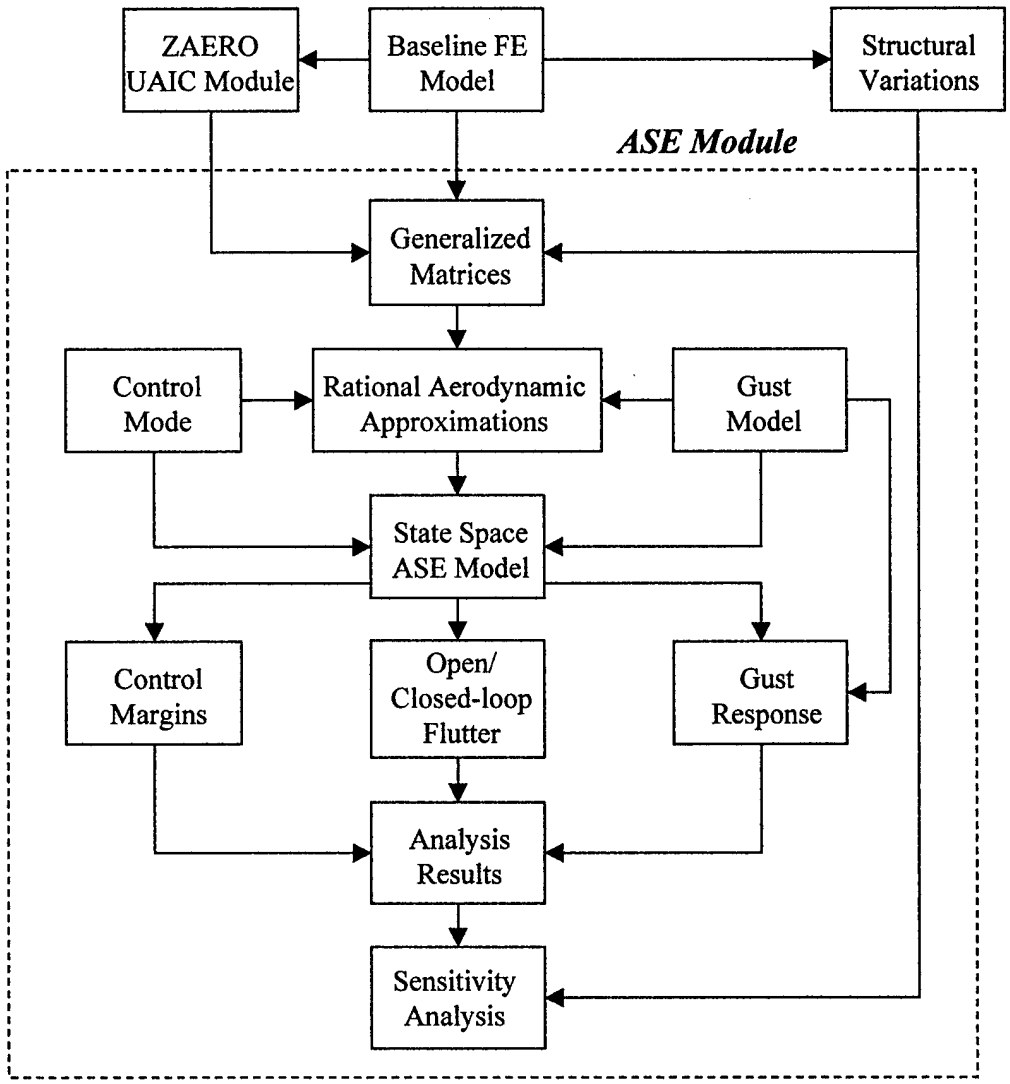

Figure 1.4 ASE Module Flow Chart

The objective of the on-line control is to design an efficient adaptive reconfigurable control system whose stability, robustness and performance can be assessed through the off-line numerical simulation. The on-line control consists of six blocks: *reduced order system matrix database* (Block 4) generated by the off-line analysis; *critical modes identification system* (Block 5) to search for critical modes and to select the system matrices as initial guess for parameter estimation; *recursive parameter estimation* (Block 6) to track the time varying parameters; *reconfigurable control system* (Block 7) to minimize the output response for flutter, ASE instability and LCO suppression, *switch-on control* (Block 8) to turn on the reconfigurable control system by thresholding the impact response and growing oscillatory response; and *automated log-off system* (Block 9) to switch off the reconfigurable control system whenever the plant is stable. In the following sections, the formulation and methodologies of the above nine blocks will be discussed in detail.

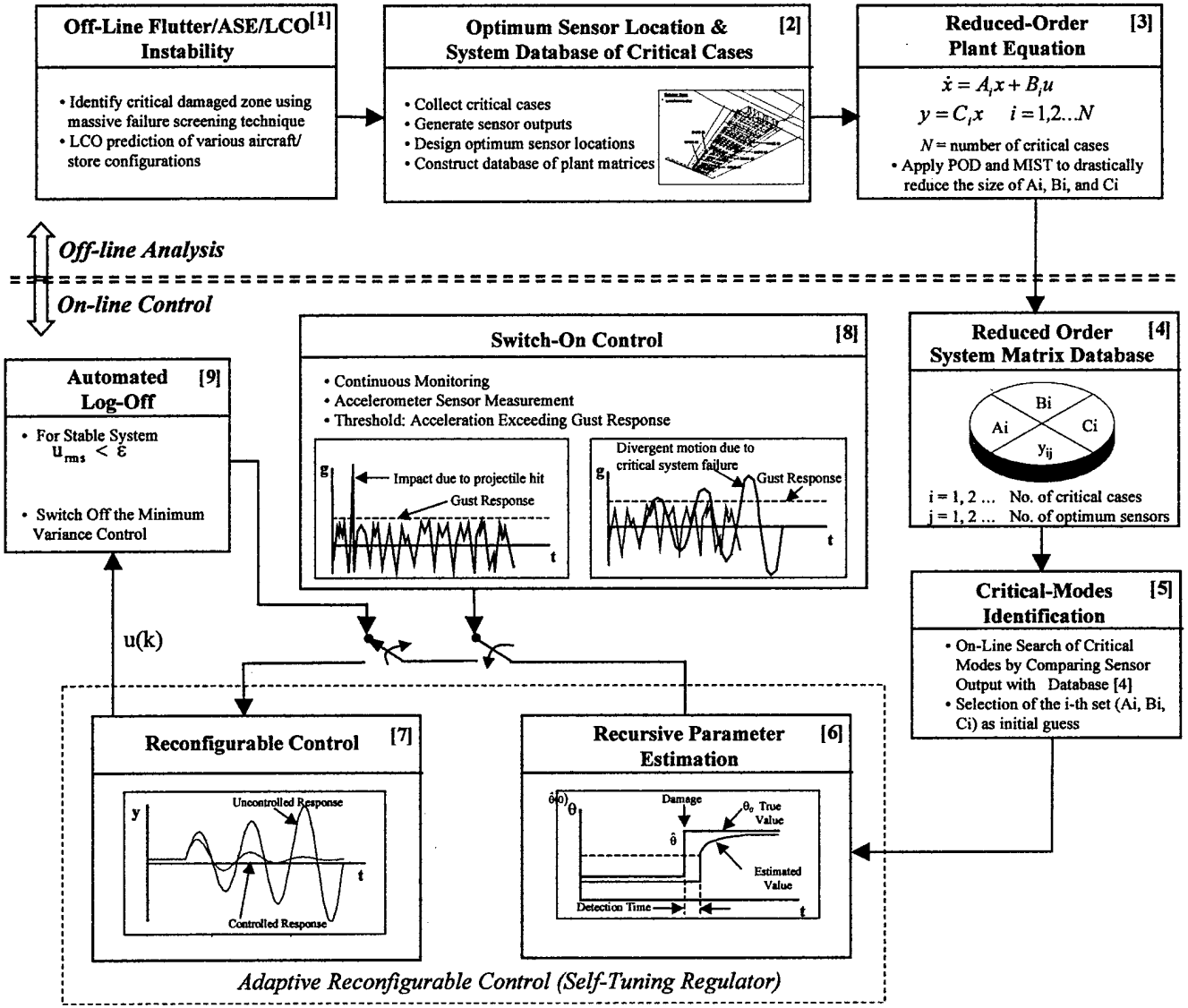

Figure 1.5 Overall Design Strategy

SECTION 2

RECONFIGURABLE CONTROL AND SYSTEM IDENTIFICATION ALGORITHM OF THE ASE SYSTEM

There are some major fundamental differences in formulating the Reconfigurable Adaptive Control (RAC) algorithm for the flexible system and the rigid-body system of a flight vehicle. These differences include:

- *States of the flexible system are not directly measurable.*

  For rigid-body flight dynamics, all states (α, β, p, q, r, ..., etc.) are physical parameters and can be directly measured. For flexible-system dynamics, the states of an aeroservoelastic system are defined in generalized coordinates (defined as modal parameters), which do not have explicit physical correspondence, and therefore are not suitable for direct measurement.

- *Restrictive finite number of sensors would not accurately measure a flexible system.*

  This calls for the design of optimum number of sensors and their locations. This optimum result must be further verified through the recursive parameter estimation on various damaged structure and LCO cases.

- *Response frequency of a flexible system is much higher than that of a rigid-body system.*

  Since flutter may induce a rapid growing amplitude, the flexible control system requires much shorter elapse time than the rigid body system. Even with a given sampling frequency of 80 Hz, this short elapse time would still impose a stringent requirement to attain a viable control system. Furthermore, since the actuator control frequency normally falls in the range of 4 ~ 10 Hz, certain types of violent flutter such as stabilator flutter may not be controllable.

- *The flexible system has less tolerance in error between the estimated and reference signals.*

  For an initially unstable system, the flexible system requires a more robust system identification technique for accurate parameter estimation. Inaccurate parameter estimation particularly in the initial state could lead to a structural failure before the control system becomes effective. For example, using the Modified Sequential Least Square method (MSLS – Refs 12, 13), it is shown in Figure 2.1 that the large error between the estimated and reference sensor signals in the initial state leads to an uncontrollable ASE system.

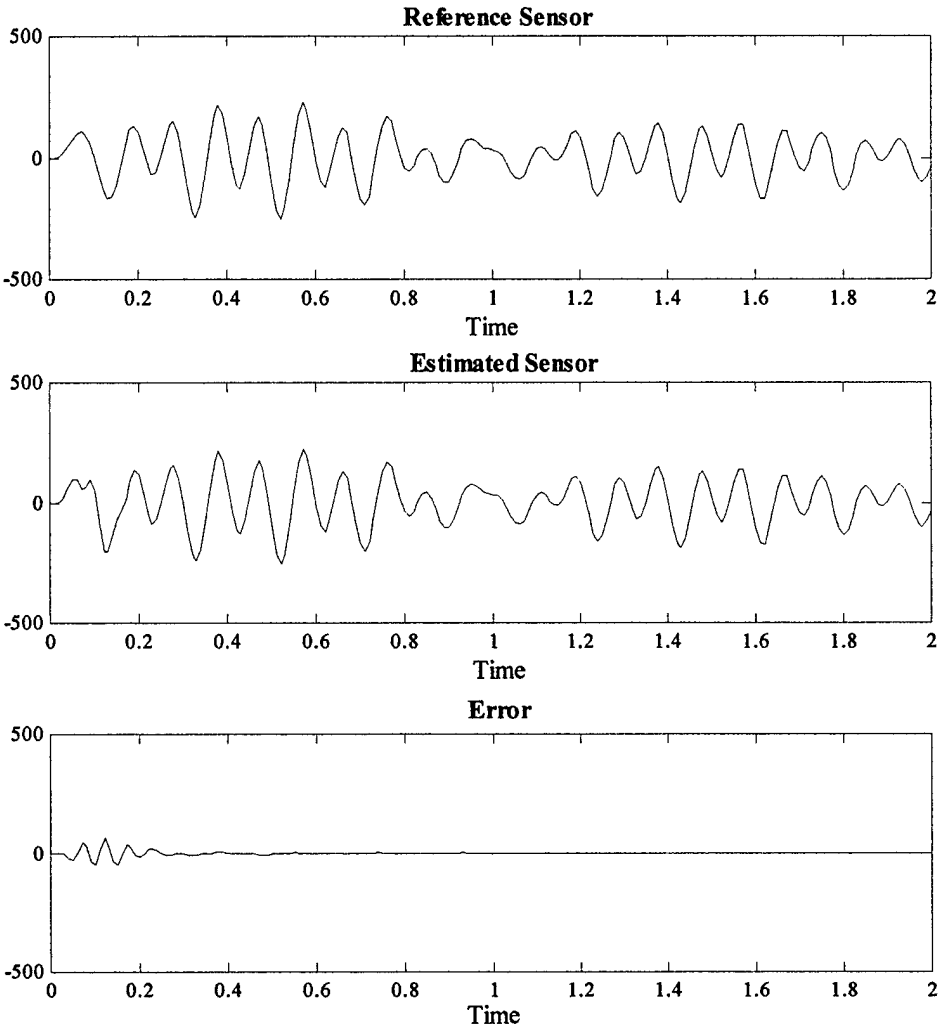

Figure 2.1 Large Error by MSLS Leads to an Uncontrollable System

The above discussion suggests that most of the Adaptive Fault-Tolerant control algorithm for rigid-body flight dynamic control can not be directly applied to an ASE control system. To achieve a robust, fault-tolerant control for an ASE system as such, we have developed a new recursive system identification algorithm called *Modal-Based Parameter Estimation* (MPE) for ASE system identification and an adaptive reconfigurable control system called *Modified Model-Following Reconfigurable* (MMFR) control. Many researchers have adopted the model-following control algorithm for rigid-body flight dynamic system (Refs 14-18). However, applying such an algorithm for the present ASE control system requires considerable modification according to the present physical requirements.

MMFR control is formulated based on the fact that the mathematical model for adaptive control system is usually obtained by the on-line system identification process using input-output signals. Usually, the mathematical model from system identification is greatly dependent on the

pattern and the magnitude of the applied input signals. Especially, the on-line recursive identification method uses the limited input signals to excite the system in a finite time. Therefore, the mathematical model obtained by the recursive identification method is less accurate than that obtained by the off-line system identification method. For this reason, great care must be taken to design a control system for the recursively identified model.

Applying MMFR control to the on-line identified system, we have also developed a recursive system identification method using the input-output responses data set, whereby an estimator is adopted to accommodate the noise effects from output information.

2.1 Modified Model-Following Reconfigurable (MMFR) Control Algorithm

Consider the following discretized system

$$x_{k+1} = Ax_k + Bu_k \tag{2.1}$$

$$y_k = Cx_k \tag{2.2}$$

where $x_k \in R^n$, $u_k \in R^m$, $y_k \in R^p$, and A, B, C are system, input influence, and output influence matrices, respectively.

The discretized system matrix A is a state transition matrix, and is always nonsingular. Therefore, the former output variables can be reconstructed with the state variables and inputs as follows:

$$y_{k-j} = CA^{-j}x_k - \sum_{i=0}^{j-1} CA^{-j+i}Bu_{k-i-1}, \quad j = 0, \cdots, q-1 \tag{2.3}$$

In the matrix form, the above equation can be expressed as

$$Y_k = Hx_k + PW_k \tag{2.4}$$

where

$$Y_k = \begin{bmatrix} y_k \\ y_{k-1} \\ \vdots \\ y_{k-q+1} \end{bmatrix}, \; H = \begin{bmatrix} C \\ CA^{-1} \\ \vdots \\ CA^{-q+1} \end{bmatrix}, \; W_k = \begin{bmatrix} u_{k-1} \\ u_{k-2} \\ \vdots \\ u_{k-q+1} \end{bmatrix},$$

$$P = \begin{bmatrix} 0 & 0 & 0 & 0 \\ -CA^{-1}B & 0 & 0 & 0 \\ \vdots & & \ddots & \vdots \\ -CA^{-q+1}B & -CA^{-q+2}B & & -CA^{-1}B \end{bmatrix}$$

Note from Eq (2.4) that the state variable x_k can be estimated for the given input and output trajectories. If the size of matrix H is $n \times n$ and the rank of system matrix is n, the state variable x_k can be uniquely determined by using Y_k and W_k.

Since Eq (2.4) shows the relation between the state variables and the input/output signals, the following equation is also satisfied,

$$\begin{aligned} Y_{k+1} &= H\, x_{k+1} + P\, W_{k+1} \\ &= HAH^{+}(Y_k - P\, W_k) + HB\, u_k + P\, W_{k+1} \end{aligned} \tag{2.5}$$

where H^{+} denotes the pseudo-inverse of matrix H.

If the rank of matrix H^{+} equals the system order n, then the solution x_k satisfying Eq (2.4) is uniquely determined. However, too many parameters are required to represent the system using Eq (2.5). Here, simple manipulation is performed to reduce the number of parameters.

By definition of W_k, the following input history equation can be constructed,

$$W_{k+1} = \begin{bmatrix} u_k \\ 0 \\ \vdots \\ 0 \end{bmatrix} + \begin{bmatrix} 0 & 0 & 0 & 0 \\ I_{m\times m} & 0 & 0 & 0 \\ 0 & \ddots & 0 & 0 \\ 0 & 0 & I_{m\times m} & 0 \end{bmatrix} W_k = I_m\, u_k + J_m\, W_k \tag{2.6}$$

where $I_m = \begin{bmatrix} I_{m\times m} & 0 & \cdots & 0 \end{bmatrix}^T$, $I_{m\times m}$ is a $m \times m$ unit matrix. With Eq (2.6), Eq (2.5) can be rewritten as

$$\begin{aligned} Y_{k+1} &= HAH^{+}(Y_k - P\, W_k) + \begin{bmatrix} CB\, u_k \\ 0 \\ \vdots \\ 0 \end{bmatrix} + P\, J_m\, W_k \\ &= HAH^{+}(Y_k - P\, W_k) + I_p CB\, u_k + P\, J_m\, W_k \end{aligned} \tag{2.7}$$

where $I_p = \begin{bmatrix} I_{p\times p} & 0 & \cdots & 0 \end{bmatrix}^T$, and $I_{p\times p}$ is a $p \times p$ unit matrix.

Now, the output variable y_{k+1} can be obtained by pre-multiplying ${I_p}^T$ to Eq (2.7). By considering the structure of matrix P, we have

$$y_{k+1} = {I_p}^T HAH^{+}(Y_k - P\, W_k) + CB\, u_k \tag{2.8}$$

Note from Eq (2.7) that the matrix HAH^{+} plays the same role as a system matrix. Assume that Eq (2.5) is expressed as follows by using input and output histories:

$$\begin{aligned} Y_{k+1} &= M_Y\, Y_k + M_W\, W_k + M_u\, u_k \\ &= M_Y(H\, x_k + P\, W_k) + M_W\, W_k + M_u\, u_k \end{aligned} \tag{2.9}$$

where

$$M_Y H = HA, \quad M_u = I_p CB, \quad M_Y P + M_W = PJ_m \tag{2.10}$$

Note from Eq (2.10) that matrix M_Y has the following structure:

$$M_Y = HAH^+ + WZ \tag{2.11}$$

where $ZH = 0$. Note that the matrix W is a design parameter computed in consideration of the structure of matrix H. If the size of matrix H is $n \times n$, and the rank of matrix H is n, then the solution is uniquely determined. By selecting the matrix W appropriately, the matrix M_Y can be constructed in the following form:

$$M_Y = HAH^+ + WZ = J_p + I_p\, \alpha \tag{2.12}$$

where $\alpha = [\alpha_1 \quad \cdots \quad \alpha_q]$, and $\alpha_i \in R^{p \times p}$.

Using Eq (2.12), we find M_W can be given as

$$\begin{aligned} M_W &= PJ_m - (J_p + I_p\, \alpha)P \\ &= (PJ_m - J_p P) - I_p\, \alpha\, P \end{aligned} \tag{2.13}$$

In consideration of the structures of P, J_m, and I_p, we have

$$PJ_m - J_p P = 0 \tag{2.14}$$

Therefore, we have

$$M_W = -I_p\, \alpha\, P \tag{2.15}$$

By substituting Eqs. (2.10), (2.12), and (2.15) into Eq (2.9), we have

$$Y_{k+1} = (J_p + I_p\, \alpha) Y_k - I_p\, \alpha\, P\, W_k + I_p\, CB\, u_k \tag{2.16}$$

In matrix form, Eqs. (6) and (16) can be rewritten

$$\begin{bmatrix} Y_{k+1} \\ W_{k+1} \end{bmatrix} = \begin{bmatrix} J_p + I_p\, \alpha & -I_p \alpha\, P \\ 0 & J_m \end{bmatrix} \begin{bmatrix} Y_k \\ W_k \end{bmatrix} + \begin{bmatrix} I_p\, CB \\ I_m \end{bmatrix} u_k \tag{2.17}$$

Note that Eq (2.17) has the same form as the equation of discretized system. Therefore, the control input can be designed as

$$u_k = -K_1 Y_k - K_2 W_k = -K \begin{bmatrix} Y_k \\ W_k \end{bmatrix} \tag{2.18}$$

One way to determine the control gain matrices is to design a control system by applying LQR theory to Eq (2.17). It is very easy to design a LQR control system that guarantees the closed-loop system stability, however computation time increased due to the large system order.

The estimator for the system shown in Eq (2.16), can be constructed as follows:

$$\hat{Y}_{k+1} = (J_p + I_p \alpha)\hat{Y}_k - I_p \alpha P W_k + I_p CB u_k + L(Y_k - \hat{Y}_k) \tag{2.19}$$

Let us introduce the estimation error $E_k = Y_k - \hat{Y}_k$. Then, the estimator error equation can be obtained by using Eqs. (2.16) and (2.19) as

$$E_{k+1} = (J_p + I_p \alpha - L)E_k \tag{2.20}$$

Assume that the estimator gain L_0 stabilizes the system matrix $(J_p + I_p \alpha_0)$ where α_0 is an identified parameter matrix using the initial model (one of the critical damage case), and L_0 is the estimator gain matrix designed by using the initial model. Then, the state estimator gain L at the current step can be designed as

$$L = I_p \alpha - I_p \alpha_0 + L_0 \tag{2.21}$$

The above equation provides an efficient algorithm for designing estimator gain matrix for the system obtained by the recursive identification method.

The closed-loop stability of the controller and estimator depend on the accuracy of the mathematical model under consideration. The recursive identification method is usually less accurate than the off-line system identification, because the excitation input signals in the on-line identification are rather limited. For example, the system responses are obtained by using input signals that have certain frequencies, and the mathematical model is identified using this input-output information. This model may not represent system responses accurately for the input signals that have other frequency bands. Therefore, the model following control scheme is adopted here in order to attain a more robust control system.

Let us define y^*_{k+1} as the desired output for the system to be followed. In this project, y^*_{k+1} is designed by applying the control input (see Eq (2.18)) to the model (see Eq (2.16)) obtained by using the initial critical damage case model, and therefore y^*_{k+1} should be the expected output responses when the system is applied by the control input. The output response can be written as

$$y_{k+1} = \alpha\, Y_k - \alpha\, P\, W_k + CB\; u_k \tag{2.22}$$

The feedback control input stabilizing Eq (2.22) can be chosen by Eq (2.18) as

$$u_k^* = -K_1 Y_k - K_2 W_k \tag{2.23}$$

Using Eq (2.23) into Eq (2.22) yields the desired model responses as

$$y_{k+1}^* = \alpha\, Y_k - \alpha\, P\, W_k + CB\; u_k^* \tag{2.24}$$

The objective of the model following control scheme is to make the system output follow the model output, i.e.,

$$\begin{aligned} y_{k+1}^* &= y_{k+1} \\ &= \alpha\, Y_k - \alpha\, P\, W_k + CB\; u_k \end{aligned} \tag{2.25}$$

The control input can be determined by applying the pseudo-inverse as

$$u_k = (CB)^+ (y_{k+1}^* - \alpha\, Y_k + \alpha\, P\, W_k) \tag{2.26}$$

Note that the existence of solution u_k is heavily dependent on the structure of matrix CB. When the number of outputs is greater than the number of inputs, the model following can be achieved in the least square sense, thereby the control input can be over-designed. On the other hand, when the number of outputs is less than the number of inputs, there exist several solutions for the input to make the system outputs follow the desired outputs. In this case, the control inputs can be designed such that the magnitude of control inputs may be minimized. Accordingly, consider the following objective function,

$$J = (y_{k+1}^* - \bar{y}_{k+1})^T Q\, (y_{k+1}^* - \bar{y}_{k+1}) + u_k{}^T R\, u_k \tag{2.27}$$

where the first term is related to the model following performance, the second term is related to control energy minimization, Q and R are positive definite weighting matrices, and the estimated output in the next step $\bar{y}_{k+1}$ is defined as follows:

$$\bar{y}_{k+1} = \alpha\, \hat{Y}_k - \alpha\, P\, W_k + CB\; u_k \tag{2.28}$$

Note in the above equation that the estimated output from Eq (2.19) is used instead of using the identified model, Eq (2.16). Substituting Eq (2.28) into Eq (2.27), and by applying the optimality condition to the resulting equation, the control input can be obtained as

$$u_k = (R + B^T C^T Q C B)^{-1} B^T C^T Q (y_{k+1}^* - \alpha\, \hat{Y}_k + \alpha\, P\, W_k) \tag{2.29}$$

2.2 Modal-Based Parameter Estimation (MPE) for System Identification

In the system identification algorithm, the mathematical model is obtained by using input and output responses. The identified model can be used to investigate characteristics of the system. Eq (2.22) can be rewritten as

$$y_{k+1} = \begin{bmatrix} \alpha & CB & -\alpha P \end{bmatrix} \begin{bmatrix} Y_k \\ u_k \\ W_k \end{bmatrix} = \theta \, \phi_k \tag{2.30}$$

where θ is a parameter matrix to be identified. In Eq (2.30), the number of parameters to represent α is $(p \times pq)$, $(p \times m)$ for CB, and $\{p \times (q-1)m\}$ for αP. Therefore, the total number of parameters in Eq (2.30) is $\{p \times (pq + qm)\}$. If pq is equal to the system order n, then the total number of parameters becomes the same as the number of parameter required for system identification.

To identify the parameters, we use s-sets of data. The chosen data sets satisfy the following equation:

$$Y = \begin{bmatrix} y_{k+1} & y_{k+2} & \cdots & y_{k+s} \end{bmatrix} = \theta \begin{bmatrix} \phi_k & \phi_{k+1} & \cdots & \phi_{k+s-1} \end{bmatrix} = \theta \, \Phi \tag{2.31}$$

Eq (2.31) is $p \times s$ constraint equations, and the number of parameters is $p \times (p+m)q$. For obtaining a better solution, s should be greater than $(p+m)q$. If not, there exists a uniqueness problem, and the identified model may not well represent the real system.

Consider the system that the parameters to be identified are time-varying. In this case, the identified parameter matrix $\theta(k-1)$ in the $(k\text{-}1)$ step and the current parameter matrix $\theta(k)$ satisfy the following relation:

$$Y - \theta(k-1)\Phi = \delta\theta \, \Phi \tag{2.32}$$

where $\delta\theta = \theta(k) - \theta(k-1)$. The least square solution of $\delta\theta$ can be obtained as follows:

$$\delta\theta = (Y - \theta(k-1)\Phi) \, \Phi^T (\Phi\Phi^T)^{-1} \tag{2.33}$$

By using Eq (2.33), the current parameter matrix can be updated by using the following recursive equation:

$$\begin{aligned} \theta(k) &= \theta(k-1) + \kappa \, \delta\theta \\ &= \theta(k-1) + \kappa \, (Y - \theta(k-1)\Phi) \, \Phi^T (\Phi\Phi^T)^{-1} \end{aligned} \tag{2.34}$$

where the positive scalar $\kappa < 1$ is the step-size for the parameter identification.

SECTION 3

IDENTIFICATION OF CRITICAL DAMAGE ZONE USING MASSIVE FAILURE SCREENING TECHNIQUE; *OFF-LINE ANALYSIS*

Figure 3.1 shows the F/A-18 structural finite element model and the aerodynamic model that are provided by Boeing/St. Louis. To identify critical damage cases for which flutter instability occurs in all possible patterns of a battle-damaged wing structure would be virtually impossible. To simplify the investigation procedure, it is assumed that the damage results from a single projectile hit which could blow a hole through the underside of the wing. Accordingly, a massive failure screening technique can be introduced for efficient identification of critical locations of the hole leading to flutter and aeroservoelastic (ASE) instability.

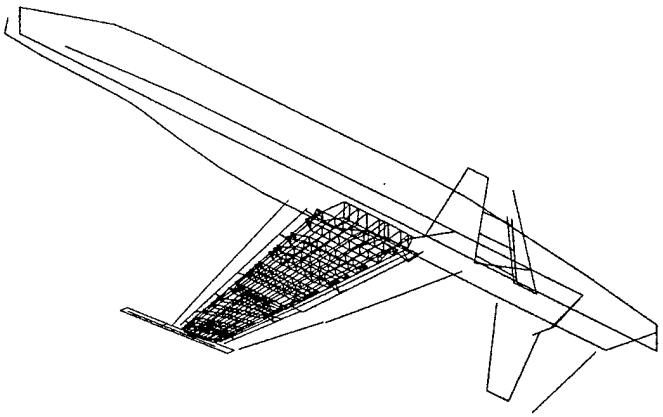

Finite Element Model of the F/A-18 Model

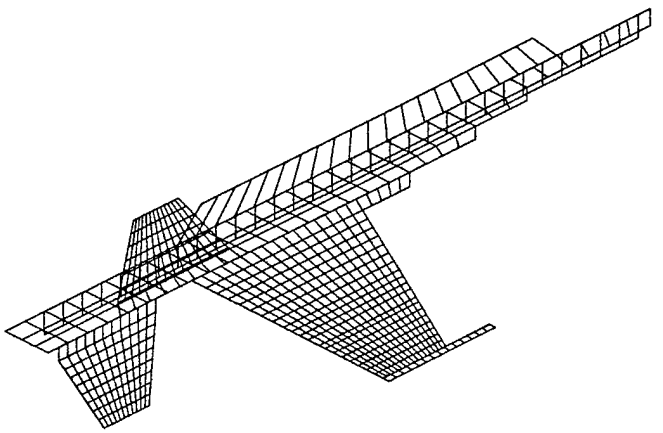

Aerodynamic Model of the F/A-18 Model

Figure 3.1 The F/A-18 FEM and Aerodynamic Models

3.1 Massive Failure Screening Technique

ZONA's massive failure screening technique assumes that accurate flutter and ASE analyses can be performed through changes in the mass ($\Delta\mathbf{M}$) and stiffness ($\Delta\mathbf{K}$) matrices alone using the vibration mode shapes of the baseline model (i.e., an unimpaired wing with no hole in its structure). This circumvents the process of physically changing the structural model to account for each hole position and size.

In this sense, the massive failure screening technique provides an effective means to rapidly find critical flutter and ASE instabilities by moving the location and size of the damage hole over the wing surface systematically as depicted by Figures 3.2 and 3.3.

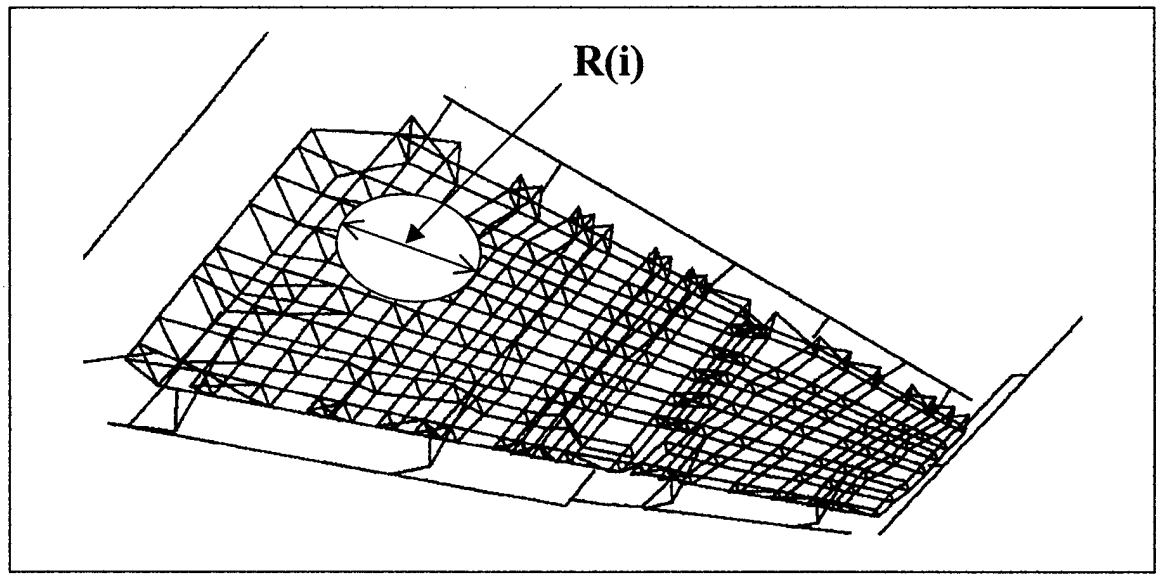

Figure 3.2 Massive Failure Screening Technique

The flutter equation of the massive screening technique is given by

$$\Phi^T(M-\Delta M)\Phi\ddot{q}+\Phi^T(K-\Delta K)\Phi q = q_\infty Q(ik)q \tag{3.1}$$

where

$\Delta M = \sum_{i=1}^{R_I}(M_{ee})_i$ is the mass matrix of all the elements located within the hole,

$\Delta K = \sum_{i=1}^{R_I}(K_{ee})_i$ is the stiffness matrix of all the elements located within the hole

$Q(ik)$ is the generalized aerodynamic forces (GAF), and

Φ is the vibration mode shapes of the baseline model (without a hole).

Note that the massive screening technique only requires that the vibration modes of each damaged case be represented by those of an unimpaired wing (baseline model). By using the so-called "pseudo hole" approach (see what follows) introduced in Eq (3.1), the massive failure screening technique can be conducted without the physical modeling of each of the damage cases with a different FEM model.

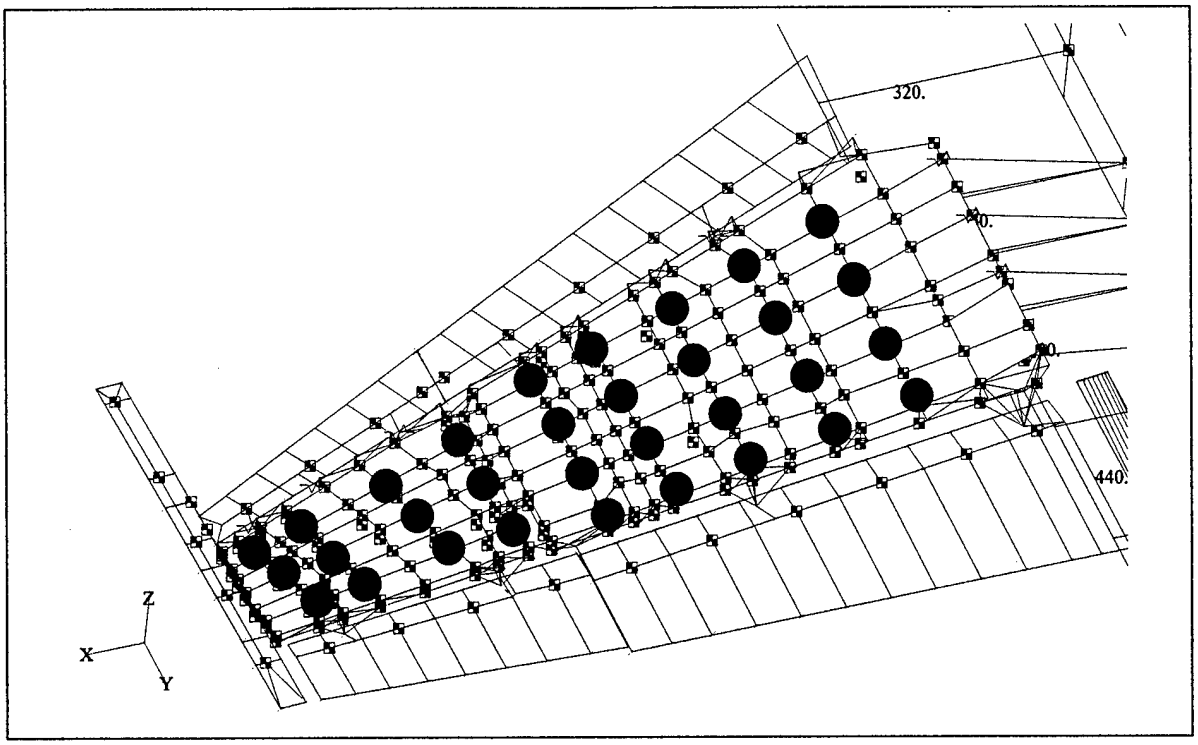

Figure 3.3 32 Damaged Cases of the F/A-18 Model

To do this, first we define 32 damaged locations on the wing as shown in Figure 3.3. A 20 inch diameter hole is located at each of the 32 damaged locations. Next, the mass ($\Delta\mathbf{M}$) and stiffness ($\Delta\mathbf{K}$) matrices of the elements located within each hole are extracted from the finite element model. Using Eq 3.1, flutter analysis is performed for these 32 damaged cases. For each flutter analysis, a total of 50 elastic modes of the baseline model is used.

With the massive failure screening technique, three critical damaged zones are identified. Figure 3.4 shows the locations and the respective flutter speeds of the damaged structure resulting from these three damage zones.

Here, the "pseudo hole" approach is defined by the massive failure screening technique to use unimpaired wing modes with the damaged hole represented by Eq (3.1), where ΔM and ΔK are set to zero. The "actual hole" approach is defined by performing the flutter analysis to use the actual impaired wing modes as computed by the FEM analysis with an actual hole in the structural model.

(a) Damaged Structure Case 1:
Hole at (91, 472, 107) R = 20″

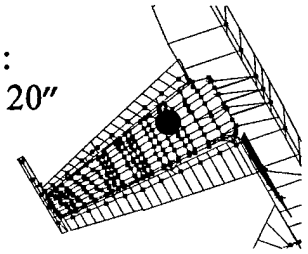

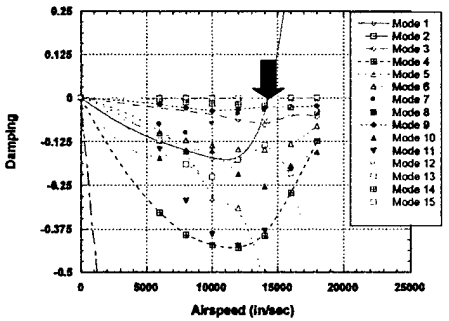

Flutter Mode

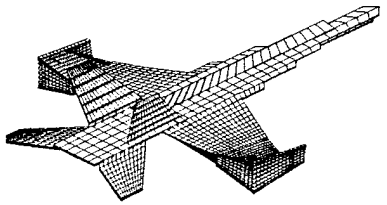

(b) Damaged Structure Case 2:
Hole at (139, 501, 105) R = 20″

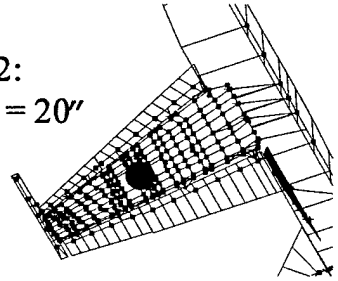

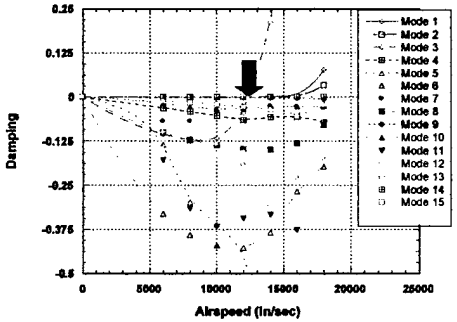

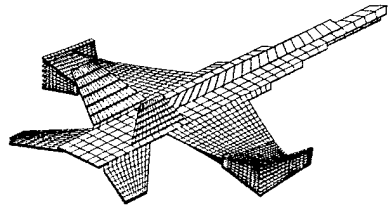

(c) Damaged Structure Case 3:
Hole at (166, 505, 104) R = 20″

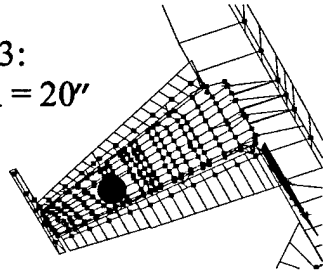

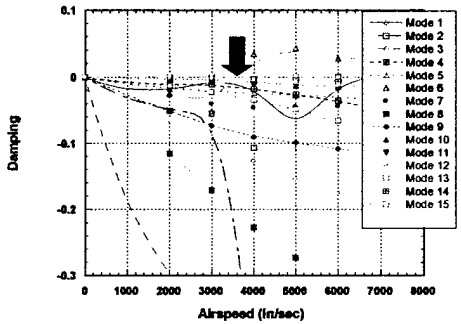

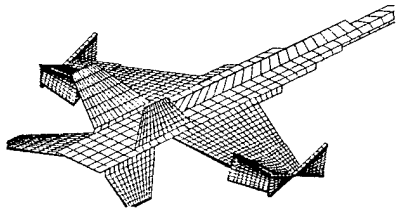

Figure 3.4 Three Critical Damage Zones of the F/A-18 Structure

Note that the pseudo-hole and the actual hole approaches are pertinent to the structural model but not to the aerodynamic model. All flutter mode results presented from Figures 3.4 through 3.10 adopt the physical aerodynamic-model presentation. Hence, no actual hole is seen in these figures (those representing flutter modes).

To validate the present massive failure screening technique, it is important to compare results of the pseudo hole approach with that of the actual hole approach. Thus, the following three damaged structure cases are selected for this purpose.

3.2 Damaged Structure Case 1

In this case a 20 inch diameter hole is created in the F/A-18 wing structure at a location of x=91, y=472 and z=107.8 inches, or (91,472,107.8) inches. A hole in this region has the effect of weakening the structure around the leading edge flap leading to lower stiffness. Due to the lower stiffness in this region, the F/A-18 structural model develops an additional lower elastic mode that corresponds to an inboard lading edge flap mode.

Figure 3.5 shows the mode shapes 3, 4, 5, and 6 of the case 1 scenario. The effect of the hole on the leading edge flap region is clearly seen.

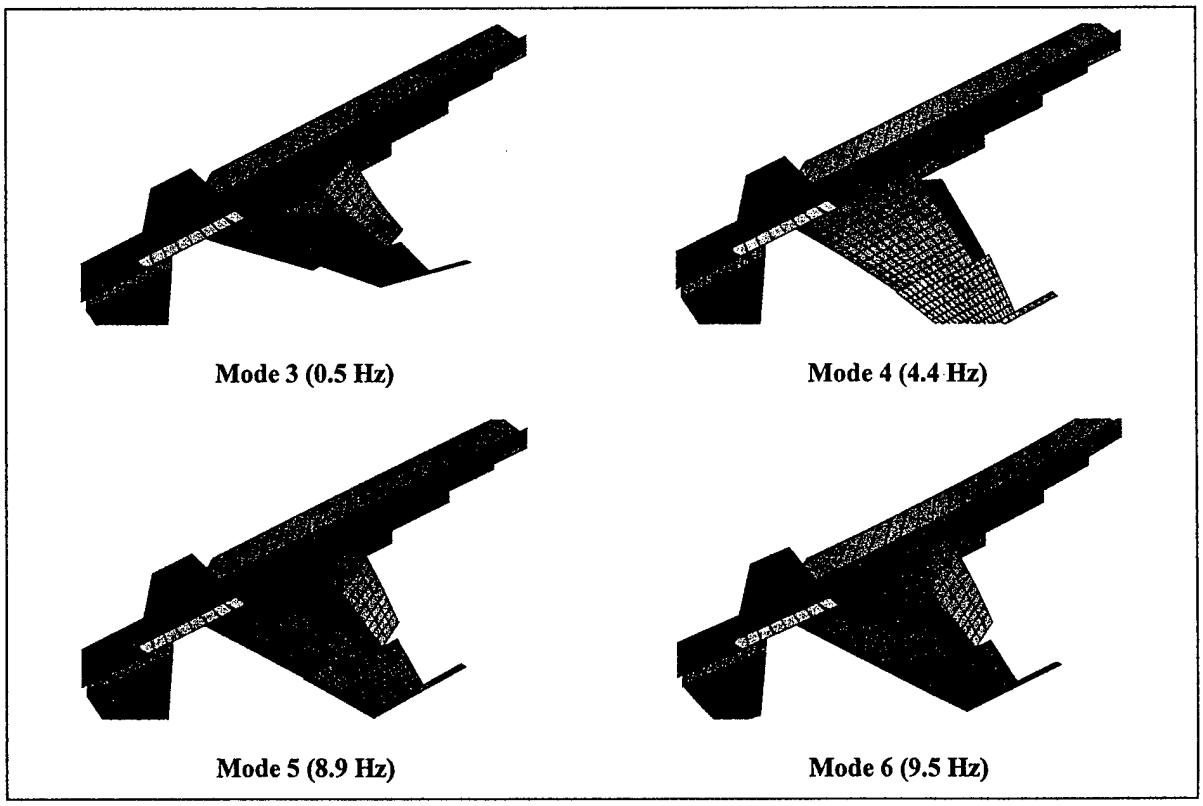

Figure 3.5 Natural Frequencies and Vibration Modes of the F/A-18 Model with a Hole Located at (91, 472, 107.8)

Actual Hole vs. Pseudo Hole Results

Although an additional lower elastic mode is found in the F/A-18 model with the actual hole approach, the flutter speed of the pseudo hole model (14,233 in/sec) is almost the same as that of the actual hole model (14,280 in/sec). The flutter mode shape plots, shown in Figure 3.6, also shows that the result from pseudo hole model is in excellent agreement with that of the actual hole model.

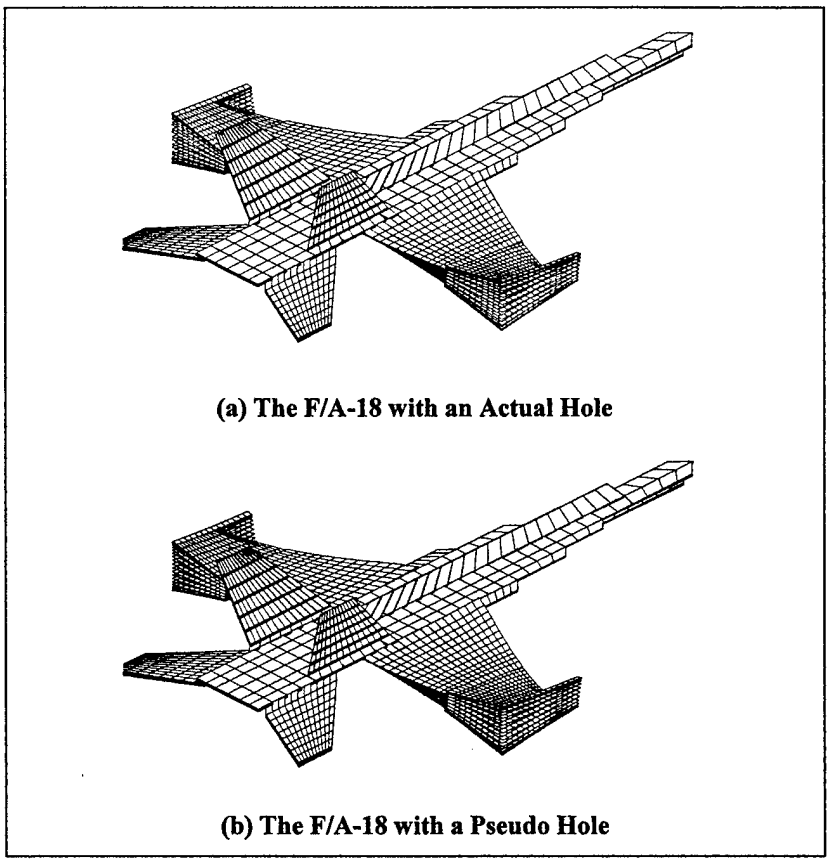

(a) The F/A-18 with an Actual Hole

(b) The F/A-18 with a Pseudo Hole

Figure 3.6 Flutter Mode Shape Comparison: (a) The F/A-18 Model with an Actual Hole, (b) The F/A-18 model with a Pseudo Hole at (91, 472, 107.8)

3.3 Damaged Structure Case 2

In this case, a 20 inch diameter hole is created in the F/A-18 wing structure around the wing mid-span region at a location of x=139, y=501.4, and z=105.3 inches, or (139,501.4,105.3) inches. Here, the finite element vibrational analysis yields two additional lower order modes. These two lower order modes result from the fact that the connection between the inner and outer wing sections are weakened.

Figure 3.7 shows the mode shapes 3, 4, 5, and 6 of the case 2 scenario. The effect of the hole on the trailing edge flap region is clearly seen.

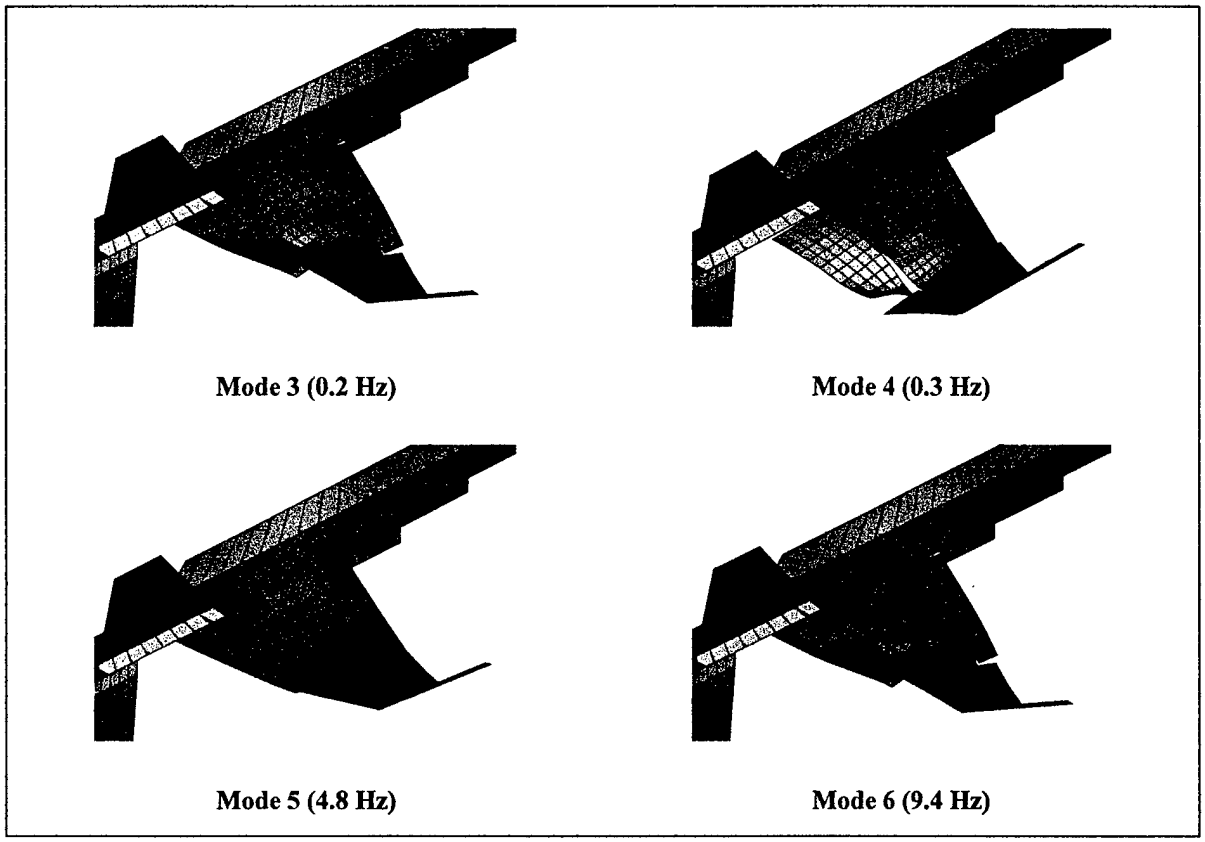

Figure 3.7 Natural Frequencies and Vibration Modes of the F/A-18 Model with a Hole Located at (139, 501.4, 105.3)

Actual Hole vs. Pseudo Hole Results

With two additional lower elastic modes appearing in the F/A-18 model with an actual hole around mid-span, the flutter speed of the pseudo hole model (12,251 in/sec) is again almost the same as that of the actual hole model (12,356 in/sec) as shown in Figure 3.8. The flutter mode shape plots, shown in Figure 3.8, also show that the result from the pseudo hole model is in excellent agreement with that of the actual hole model.

3.4 Damaged Structure Case 3

In this case, a 20 inch diameter hole is located in the F/A-18 wing structure at x = 166, y = 500, and z = 104 inches, or (166,500,104) inches. With the assigned hole, the structural elements connecting the inner wing and outer wing become much softer. In addition, the structural elements which are connected to the actuator become softer as well.

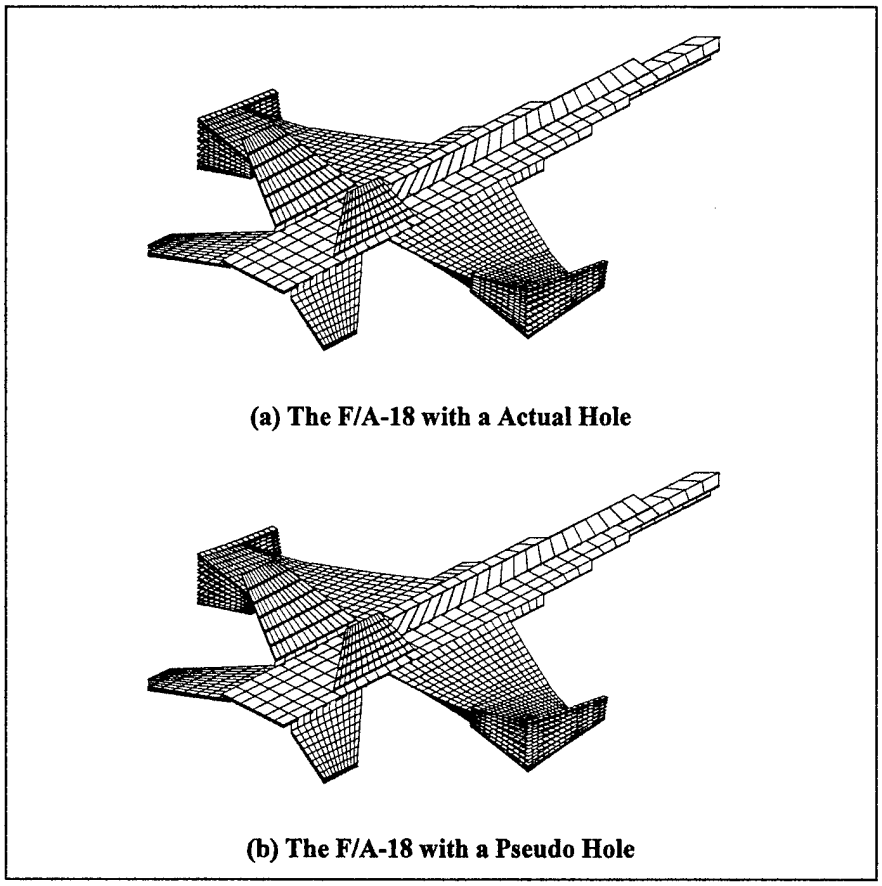

(a) The F/A-18 with a Actual Hole

(b) The F/A-18 with a Pseudo Hole

Figure 3.8 Flutter Mode Shape Comparison: (a) The F/A-18 Model with an Actual Hole, (b) The F/A-18 model with a Pseudo Hole at (139, 501.4, 105.3)

For accurate prediction of flutter speed, accurate system matrices, parameter estimation, and active control system, the vibration analysis is conducted using the actual hole approach. Figure 3.9 shows the first 4 elastic modes for this critical damage case in which the natural frequencies are dramatically reduced. As shown in the figure, the dominant vibration modes are aileron dominant.

The modal reduction is conducted using 50 vibration modes. The flutter speed is calculated by the actual hole approach. Figure 3.10 (a) and (b) show the damping changes for the different airspeeds and indicate the flutter mode. The calculated flutter speed is 3,599 in/sec, which is only 20 % of the flutter speed of the baseline model without damage. The flutter mode is an aileron dominant mode as shown in Figure 3.10 (b).

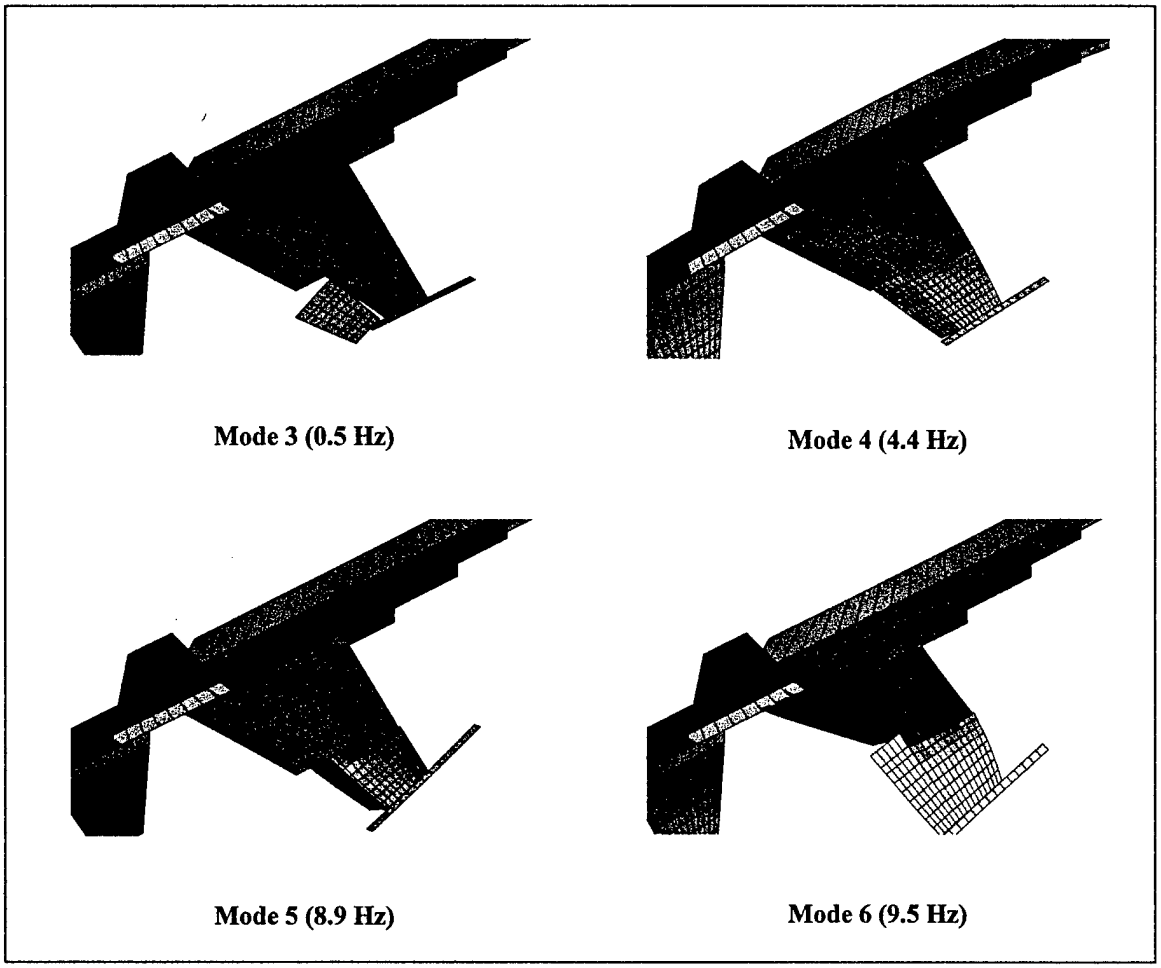

Figure 3.9 First 4 Lower Elastic Modes of the Critically Damaged theF/A-18 Case 3 (Actual Structural Approach)

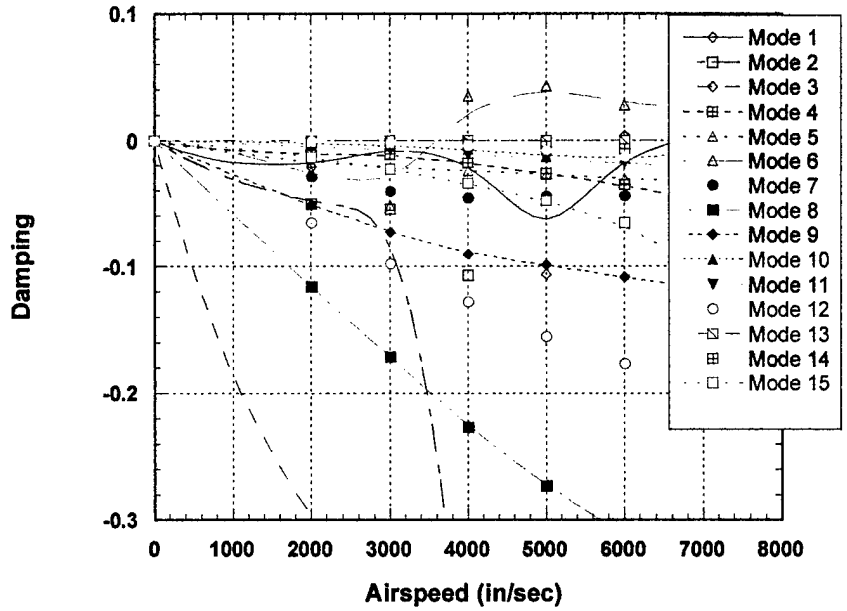

(a) Damping versus Airspeed

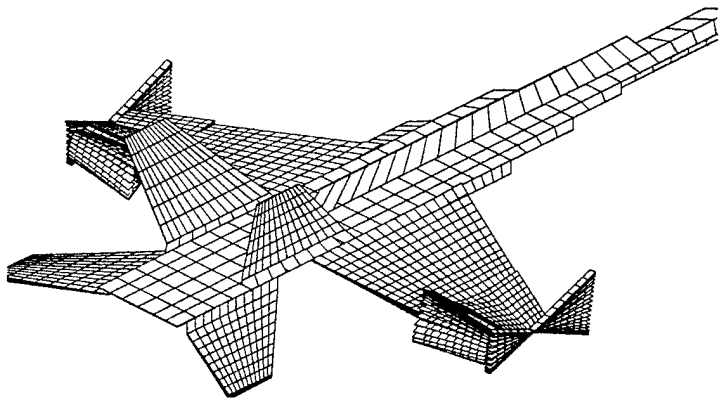

(b) Flutter Mode Shape

Figure 3.10 Flutter Results of Critically Damaged the F/A-18 Case: (a) Damping versus Airspeed, (b) Flutter Mode Shape

SECTION 4

CORRELATION OF THE F/A-18 / STORE LCO PREDICTIONS WITH FLIGHT TEST DATA

It is known that the F/A-18 with underwing stores may encounter Limit Cycle Oscillation (LCO). Two types of LCO frequencies are observed during flight tests: one occurs at 5.6 Hz for cases of wing/store with tip missile; the other occurs at 8.8 Hz for cases of wing/store with tip launcher only. Figure 4.1 shows five selected the F/A-18 / Store configurations experiencing LCO in the transonic flight regime.

Case	Store Configuration	LCO Frequency	Flight Condition
1. 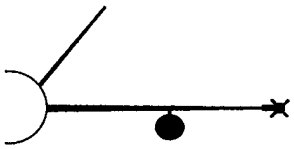	Wing Tip: Launcher + Missile Outboard Pylon: MK-84 Inboard Pylon: None	5.6 Hz	$M \approx 0.88 - 1.0$
2. 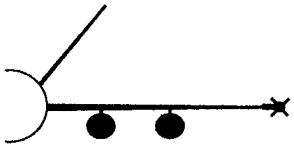	Wing Tip: Launcher + Missile Outboard Pylon: MK-84 Inboard Pylon: MK-84	5.6 Hz	$M \approx 0.88 - 1.0$
3. 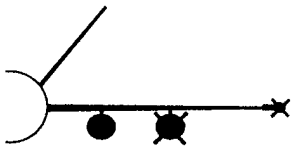	Wing Tip: Launcher + Missile Outboard Pylon: AGM-88 Inboard Pylon: MK-84	5.6 Hz	$M \approx 0.88 - 1.0$
4. 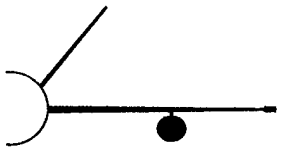	Wing Tip: Launcher Only Outboard Pylon: MK-83 Inboard Pylon: None	8.8 Hz	$M > 0.9$
5. 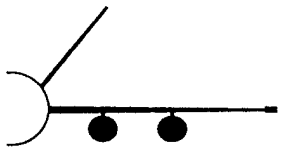	Wing Tip: Launcher Only Outboard Pylon: MK-83 Inboard Pylon: MK-83	8.8 Hz	$M > 0.9$

Figure 4.1 Five Selected F/A-18 / Store LCO Cases

To suppress LCO using reconfigurable adaptive control, it is necessary to validate the accuracy of the plant matrices generated by ZAERO/ASE module. This is done by correlating the predicted flutter results of the five selected LCO cases with the flight test data. Since the LCO cases considered occur in transonic flight regime, the nonlinear ZTAIC method is employed to generate the transonic unsteady aerodynamics of the plant. Figure 4.2 shows the aerodynamic models of the five LCO cases where the external stores, launchers and pylons are included in these models.

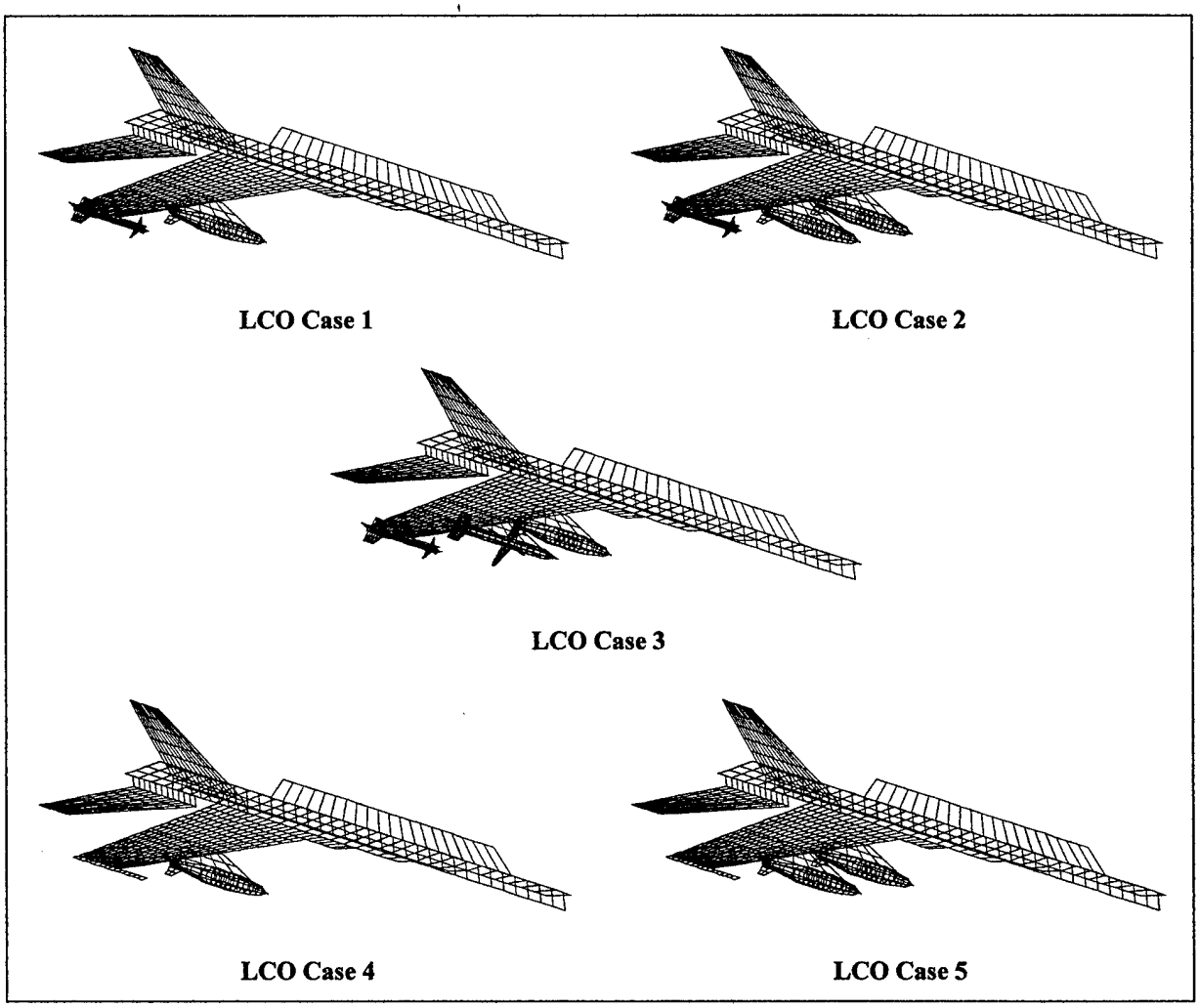

Figure 4.2 Aerodynamic Models of the Five LCO Cases

As discussed earlier, ZTAIC computes the transonic unsteady aerodynamics based on an externally provided "*steady aerodynamic background flow*", which is computed by using the CFL3D Navier-Stokes solver (Ref 19). Figure 4.3 shows the CFL3D computed steady pressure distributions at 50% span of the F/A-18 wing at Mach numbers 0.85, 0.9, 0.95, 0.97 and 1.05. It

can be seen that the transonic shock waves already appears at Mach number 0.85 and moves to trailing edge in low supersonic flow (M=1.05). This is a strong indication that the nonlinear transonic shock could be a "triggering" agent of the F/A-18 wing/store LCO. Such nonlinear aerodynamics must be accounted for by effective unsteady aerodynamic computation. ZONA elected to use the nonlinear ZTAIC method for its proven accuracy and computing efficiency.

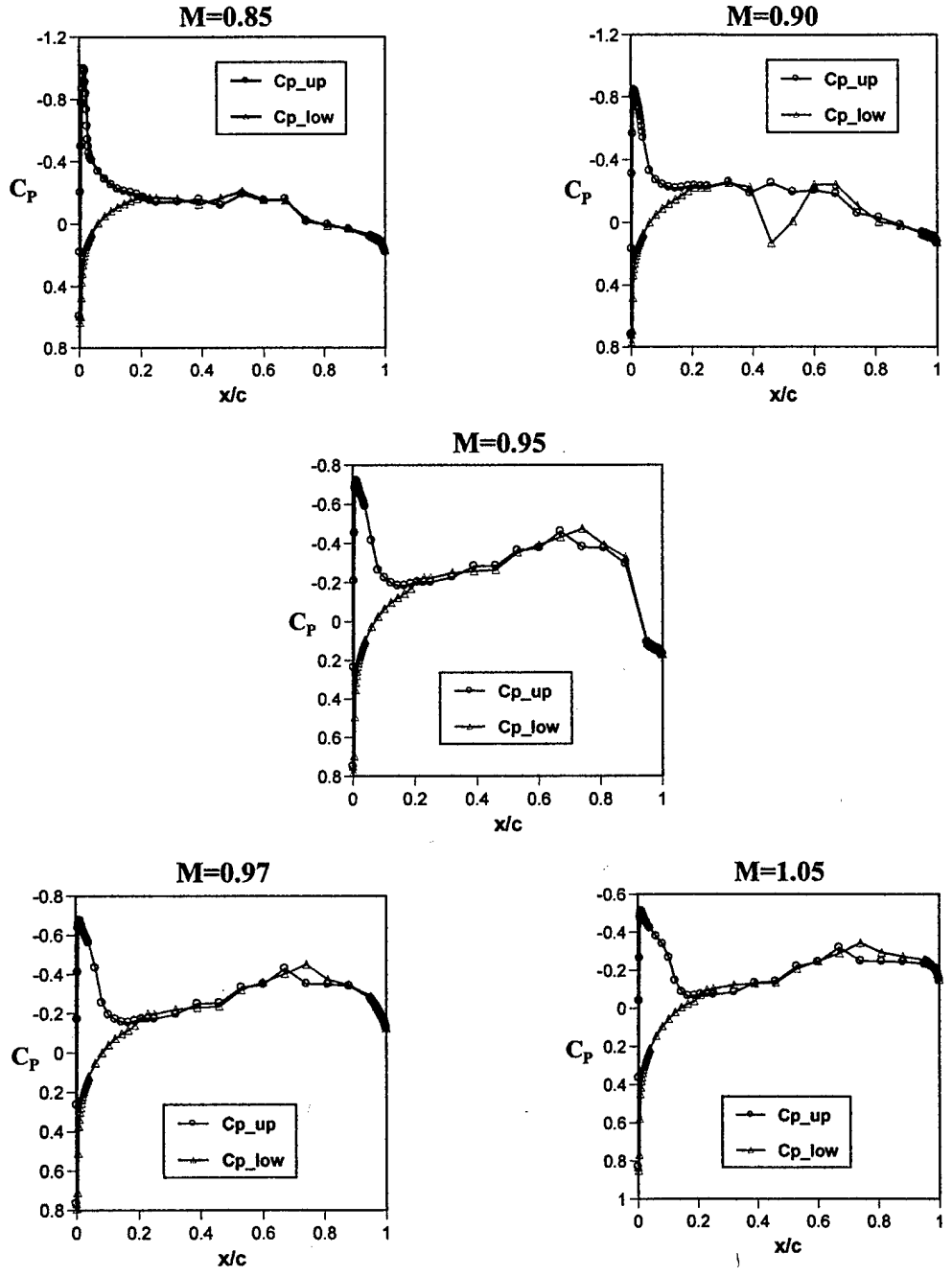

Figure 4.3 Steady-Pressure Distributions on the F/A-18 Wing (at 50% Span)

4.1 ZTAIC Unsteady Aerodynamics

As discussed earlier, flutter analysis can be used for the correlation with LCO if a hump mode is predicted. Obtained with the ZTAIC generated transonic unsteady aerodynamics, the flutter results of LCO Case 1 and Case 5 at M = 0.9 are presented in Figures 4.4 and 4.5, respectively.

In Figures 4.4 and 4.5, the flutter results obtained with the linear aerodynamic method ZONA6 is also presented (no transonic shock included). It can be seen that the flutter frequencies predicted by the nonlinear ZTAIC methods correlate well with the flight test LCO frequencies (5.6 Hz for LCO Case1 and 8.8 Hz for LCO Case 5). But the linear method fails to predict a hump flutter mode. The hump (flutter) mode is obtained by nonlinear ZTAIC method resulting a low-level distabilizing aerodynamic damping which confines the system oscillation to the region below that of actual flutter. As discussed earlier, the divergent oscillation induced by such a low distabilizing aerodynamic damping could be "balanced-off" by an amplitude-dependent friction damping in the structure thus resulting in a steady-state oscillation, i.e., LCO.

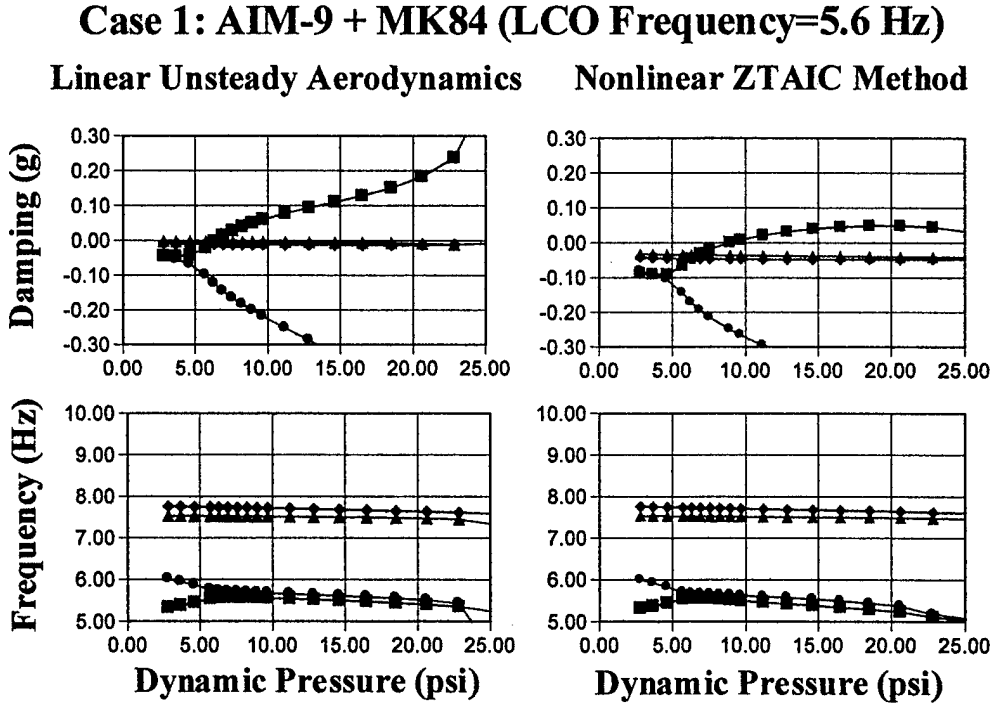

Figure 4.4 Flutter Results Using Linear and Nonlinear ZTAIC Methods of LCO Case 1 at M=0.9

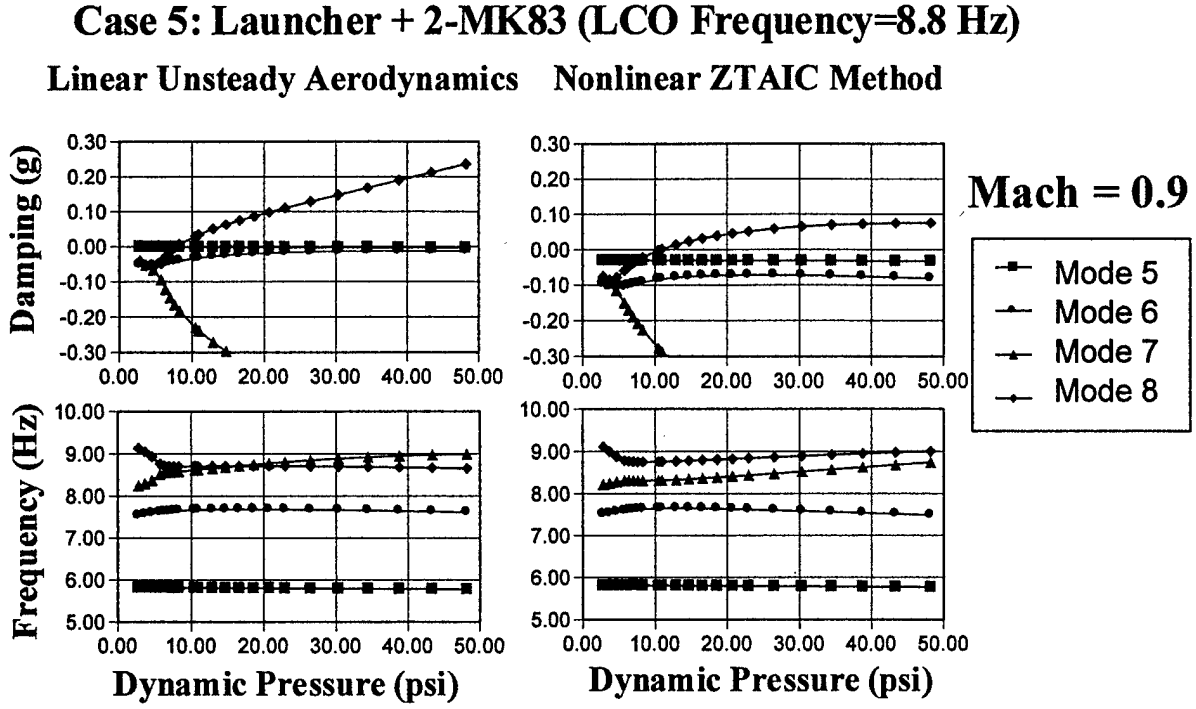

Figure 4.5 Flutter Results Using Linear and Nonlinear ZTAIC Methods of LCO Case 5 at M=0.9

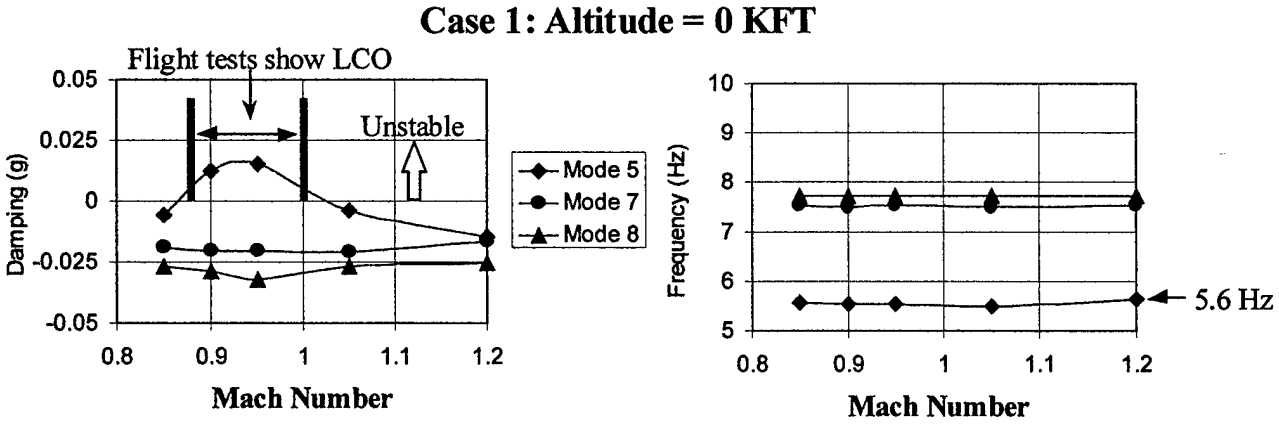

Figure 4.6 Damping and Frequency vs. Mach Number of LCO Case 1

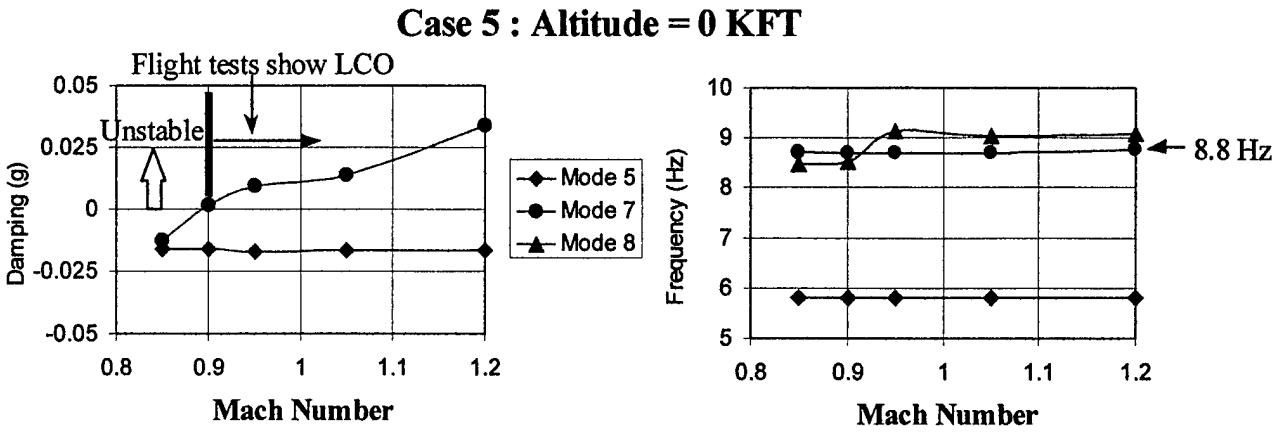

Figure 4.7 Damping and Frequency vs. Mach Number of LCO Case 5

4.2 Correlation of Flutter Results with LCO Flight Test Data

Figure 4.6 shows the flutter results in terms of damping and frequency vs. Mach number for LCO Case 1 at sea level as computed by using the nonlinear ZTAIC method. These results suggest that LCO starts at M ≈ 0.88 and dissapears in the low supersonic flow regime. The flutter frequency remains at 5.6 Hz throughout the entire Mach range. The predicted flutter results are in excellent agreement with the flight test data shown in Figure 4.1.

Figure 4.7 shows the flutter results in terms of damping and frequency vs. Mach number for LCO Case 5 at sea level. These results show that LCO starts at M ≈ 0.9 and becomes more severe due to the increase of damping as Mach number increases. The flutter frequency however remains at 8.8 Hz throughout the entire Mach range. Again, this finding confirms the flight test data shown in Figure 4.1.

4.3 LCO Modes of Five LCO Cases

The LCO modes predicted by ZAERO using the nonlinear ZTAIC method for five selected LCO cases are depicted in Figure 4.8. These LCO modes are all anti-symmetric which agree with the flight test data. Further results of the damping and frequency diagrams of LCO Case 2, 3 and 4 will be presented in the next section.

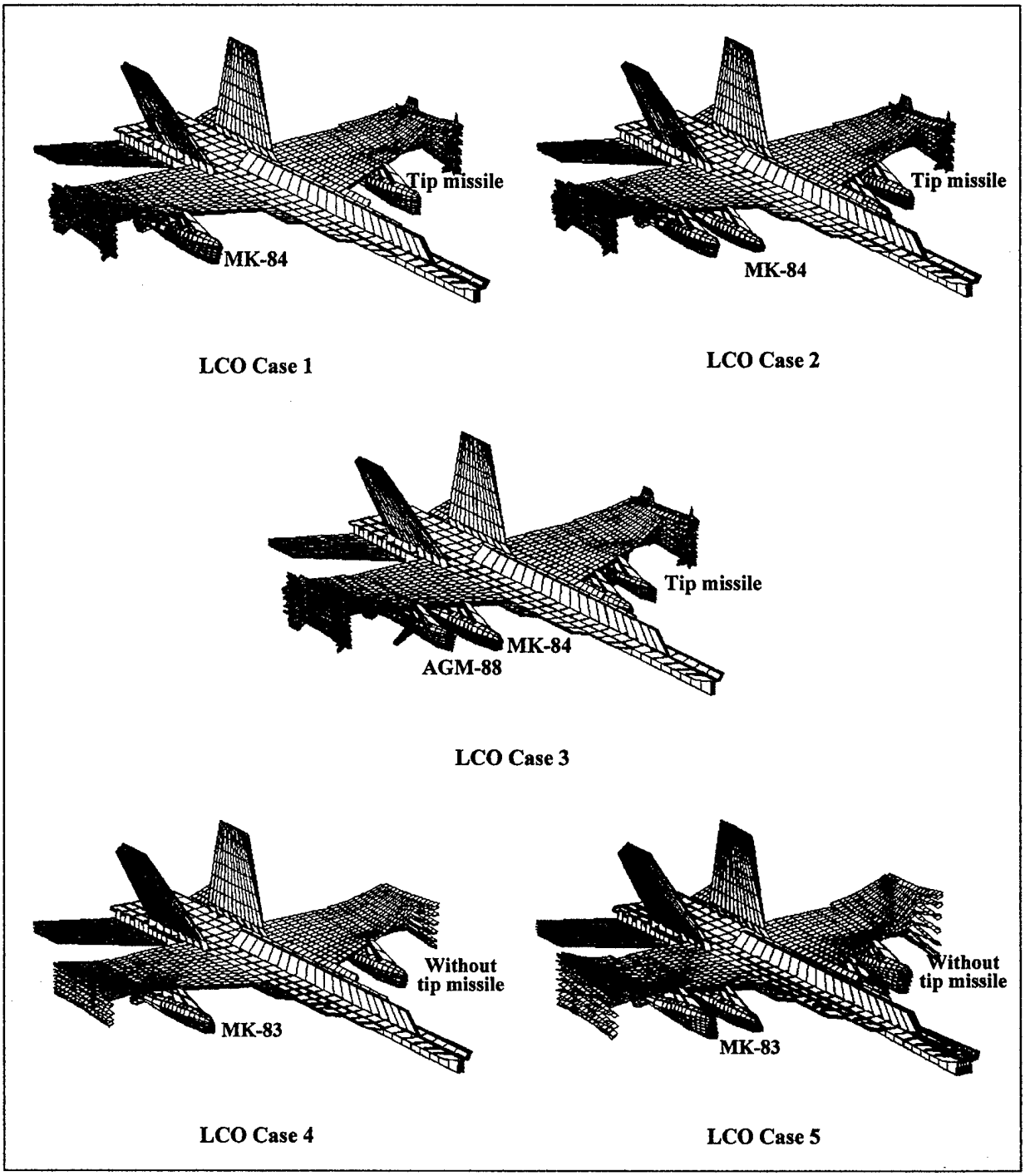

Figure 4.8 The F/A-18 with Stores and LCO Modes of the Five LCO Cases

SECTION 5

REDUCED-ORDER PLANT MATRIX GENERATION

The plant matrices of the three damage cases and five LCO cases are generated using the ASE module in ZAERO. The ASE module generates the ASE system matrices in a state space form as:

$$\begin{aligned} \{\dot{x}\} &= [A]\{x\} + [B]\{u\} \\ \{y\} &= [C]\{x\} + [D]\{u\} \end{aligned} \tag{5.1}$$

NASTRAN FEM analysis provides 40 structural modes of the F/A-18 FEM model for the flutter analysis; hence the number of states in Eq 5.1 amounts to 80 structural states. Using such a large system matrix for real-time control is unlikely to be feasible. To reduce the size of the ASE matrices, we employed two methods for system matrix reduction: the Proper Orthogonal Decomposition (POD) technique (Refs 20-22) for structural state reduction; the Minimum State (MIST) method (Ref 23) for aerodynamic state reduction. The objective of using POD and MIST is to achieve a minimum number of state for the ASE system matrices while preserving the essential dynamic characteristics of the plant.

5.1 Proper Orthogonal Decomposition (POD) Technique for Structural State Reduction

The idea behind the POD technique is a simple one. We first calculate the response of the plant at M different combinations of frequency and excitation. The solutions (also called "snapshots") are denoted by $\mathbf{q}^m$ for $m = 1, 2, \ldots, M$. These snapshots are then linearly combined to form a smaller number of basis vectors ϕ_K for $k = 1, 2, \ldots, K$, where $K < M$. In other words,

$$\phi_K = \sum_{m=1}^{M} \mathbf{q}^m \, \mathbf{v}_k^m = \mathbf{S}\,\mathbf{V}_k, \qquad k = 1, 2, 3, \ldots, K \tag{5.2}$$

where $\mathbf{v}_k^m$ is the contribution of the m^{th} snapshot to the k^{th} basis vector. $\mathbf{S}$ represents the matrix whose columns are the vectors of the snapshot. It is assumed that the vector $\mathbf{V}_k$ has been suitably scaled so that the vectors ϕ_K are unit length. The vectors $\mathbf{V}_k$ are selected so that they lie along the principle axis of the space spanned by $\mathbf{S}$, that is, the quantity $\left\| \mathbf{S}^T \mathbf{S}\, \mathbf{V}_k \right\|$ is extremized subject to the constraint that ϕ_K is unit length. Thus, introducing the Lagrange multiplier λ_k, we find the vector $\mathbf{V}_k$ that makes z stationary, where

$$z = \mathbf{V}_k \mathbf{S}^T \mathbf{S}\, \mathbf{S}^T \mathbf{S}\, \mathbf{V}_k - \lambda_k \left(\mathbf{V}_k \mathbf{S}^T \mathbf{S}\, \mathbf{S}\, \mathbf{V}_k - 1 \right) \tag{5.3}$$

Taking the variation of z and settling the result to zero gives:

$$\mathbf{S}^T \mathbf{S}\, \mathbf{V}_k = \lambda_k \mathbf{V}_k \tag{5.4}$$

Eq 5.4 defines an eigenvalue problem for the eigenvectors $\mathbf{V}_k$ and eigenvalues λ_k. Those eigenvectors with the largest values of λ_k give the largest values in the vector $\mathrm{V_k}$. In other words, the snapshots $\mathbf{q}^m$ tend to lie in a sub-space spanned by the basis vectors ϕ_K with the largest eigenvalues λ_k.

5.2 Minimum State (MIST) Method for Aerodynamic State Reduction

Since the ZAERO/unsteady aerodynamic module computes the unsteady aerodynamic force matrices in the frequency domain, transformation from frequency domain to continuous time domain requires a rational aerodynamic approximation. However, rational aerodynamic approximation creates additional states (called aerodynamic states) in the ASE state space equation, minimizing these additional states which would be a major concern for designing an effective closed-loop control system.

The MIST method expresses the rational aerodynamic approximation in the following form:

$$[\mathbf{Q}(p)] = [\mathbf{A}_0] + [\mathbf{A}_1]\, p + [\mathbf{A}_2]\, p^2 + [\mathbf{D}] \left[[\mathbf{I}]\, p - [\mathbf{R}] \right]^{-1} [\mathbf{E}]\, p \tag{5.5}$$

where p is the non-dimensional Laplace parameter and $\mathbf{Q}(p)$ is the unsteady aerodynamic forces in the continuous time domain.

Eq 5.5 shows that the number of aerodynamic states is equal to the order of the aerodynamic root matrix $[\mathbf{R}]$. Using a physical weighting technique (Ref 24) for determining the optimum values of matrices $[\mathbf{D}]$ and $[\mathbf{E}]$, it can be shown that good aerodynamic approximation can be achieved by using minimum order of $[\mathbf{R}]$.

5.3 Verification of Reduced Order Plant Matrices by Open-Loop ASE Analysis

Using the POD technique and MIST method, it is found that the number of states can be reduced to 7, rendering a smallest possible size of ASE matrices for feasible real-time control. These 7 states consist of 6 structural states (3 POD modes) and 1 aerodynamic state. The reduced-order ASE matrices are then verified by the comparison of flutter results between the flutter analysis (40 structural modes) and the reduced-order open-loop ASE analysis (3 POD modes and 1 aerodynamic state). This comparison is shown in Figure 5.1 for five LCO Cases considered. Excellent agreement of the flutter prediction results in using the 40-modes flutter analysis as opposed to using the reduced-order open-loop ASE analysis is achieved. Similar good agreement were obtained for the previous three critical damage cases, but these results are not presented here.

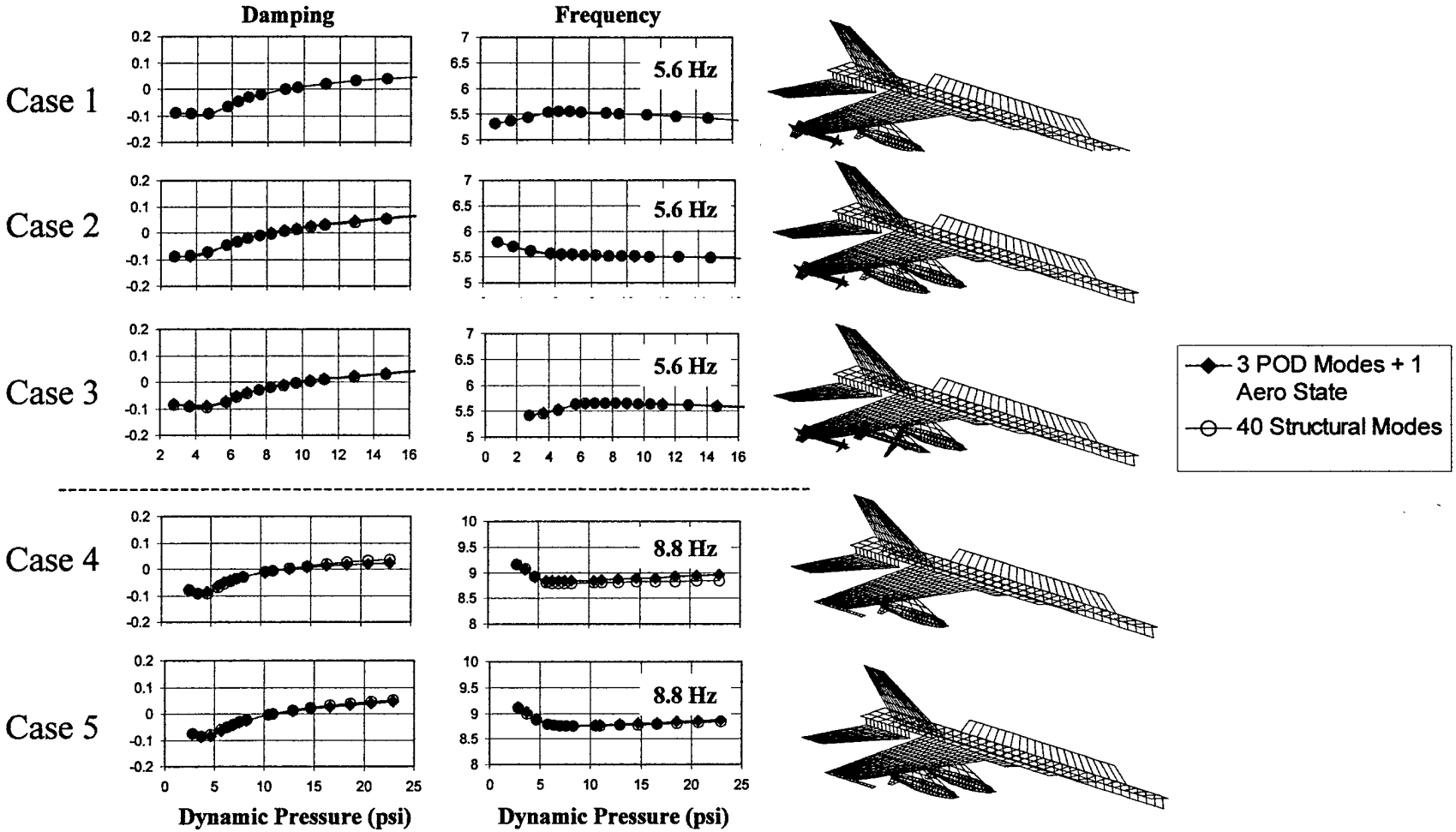

Figure 5.1 Comparison of the Flutter Results: 40-Modes Flutter Analysis vs. Reduced-Order ASE Analysis

SECTION 6

OPTIMUM SENSOR LOCATIONS BY SHORT-TIME FOURIER ANALYSIS

The sensor locations need to be determined for accurate sensor response and rapid identification. Once determined, the sensor output signal will be used for critical modes identification. Also, these sensors must be able to effectively measure and feedback the signals in real time. Although all of the modes show up in the sensors, dominant modes measured by each sensor yield different sensor signal, which depends on the sensor location.

As a first step, we assumed that the sensors are placed uniformly over the main wing area as shown in Figure 6.1. Figure 6.1 shows 10 accelerometers which are uniformly placed over the wing region and 3 rate gyros at the outboard/trailing edge(TE) region. For critical damage case, the frequency distributions of each sensor signal due to disturbances are calculated in terms of its normalized magnitude *Mj* and phase angle Φ_j.

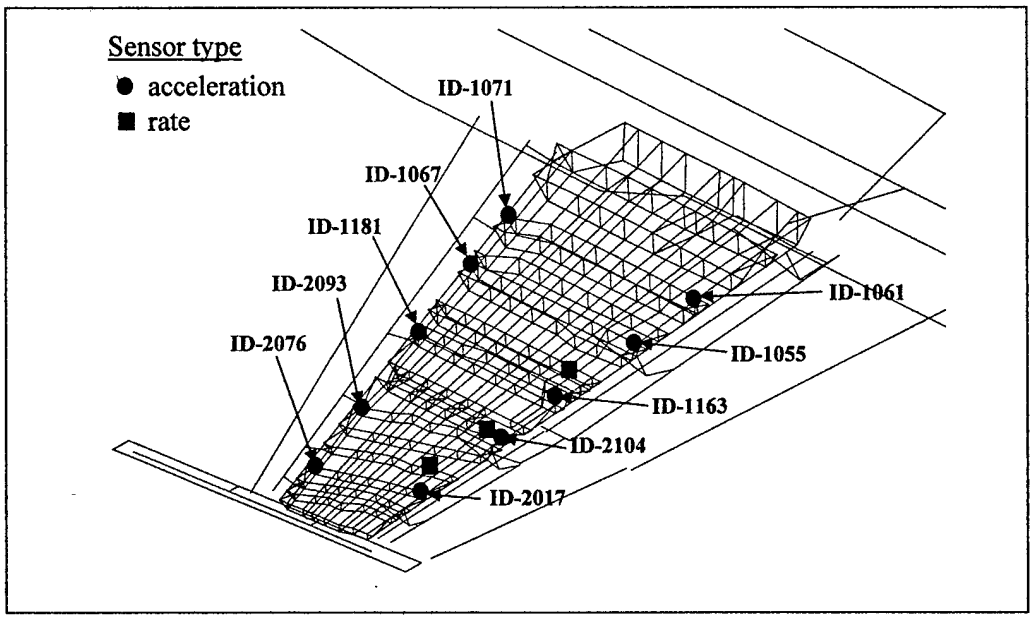

Figure 6.1 10 Accelerometers and 3 Rate Gyro Locations Placed on the F/A-18 Wing Model

Table 1 shows the typical results. This table contains the magnitude and phase angle of the sensors due to the disturbances of the F/A-18 model with critical damage (CASE 22) (CASE 22: *damage is located at x=166, y=505, z=104 inches; Hole Diameter=20 inches, see Section 3*). It was assumed that the disturbance frequency is around 11 Hz, which is close to the flutter frequency. By comparing their magnitudes, sensors located at (ID2093, ID2076, ID1055, ID1163, ID2104, ID2017) are selected for critical damage identification. Those locations are the outboard regions of the LE(leading edge)/TE(trailing edge) of the wing. The phase angles are

also calculated and compared. However, it was found that the phase angle can not match the data with reasonable accuracy. It was then decided to use the magnitude (matched well with the data) alone for the damage identification parameter.

Table 6.1 Magnitude and Phase Angle of the Sensors due to Disturbances (Critical Damage Case 22, V=3000 in/sec, Sea Level)

Structural ID No. (coordinate)	Magnitude	Phase Angle
1071 (89.0, 454.1, 110.3)	3.11	179.42
1067 (111.1, 462.1, 108.8)	2.72	-179.71
1181 (145.2, 474.5, 106.4)	12.06	-164.22
2093 (179.5, 487.9, 104.4)	85.25	-161.62
2076 (208.1, 499.2, 102.9)	118.05	-160.81
1061 (85.3, 516.8, 110.5)	27.69	20.01
1055 (110.9, 520.1, 108.7)	52.70	18.52
1163 (245.2, 524.4, 106.3)	115.84	17.34
2104 (170.8, 507.1, 105.5)	314.59	19.49
2017 (199.3, 531.3, 104.7)	487.54	18.85

6.1 Algorithm of Short-Time Fourier Analysis

If one assumes that excitation of a single mode occurs, then the problem can be reduced to detection the presence of a sine-wave of unknown magnitude, frequency, and phase in additive white noise. The sensor signals are approximated by a sum of sine waves. For each sensor signal, the sine wave reads:

$$\hat{y}_j(k) = \hat{M}_j \sin\left(\omega_j\, k\, t_s + \hat{\Phi}_j\right), \quad \begin{array}{l} k = 1, 2, \ldots, \text{number of sampling data} \\ j = 1, 2, \ldots, \text{number of sensors} \end{array} \tag{6.1}$$

where $\hat{y}_j$, ω_j, $\hat{M}_j$, $\hat{\Phi}_j$ and t_s are the approximated sensor signal, frequency, magnitude, phase angle and the sampling time, respectively. A single sine wave regression analysis is used to estimate the frequency ω_j of the sensors, and short-time Fourier analysis is used to estimate the magnitude $\hat{M}_j$ of the signals by recursive procedure.

Each sensor signal can be represented in state-space form as:

$$\hat{x}_i(k) = \begin{bmatrix} C_i & S_i \\ -S_i & C_i \end{bmatrix} \hat{x}_i(k-1) + \sum_{k=1}^{N+1} \frac{2}{N} \begin{bmatrix} C_i^l \\ -S_i^l \end{bmatrix} \{y(k-l+1) - \hat{y}(k-l+1)\} \tag{6.2}$$

where

$$\hat{y}(k) = [1 \quad 0]\begin{Bmatrix}\hat{x}_1(k-1)\\ \hat{x}_2(k-1)\end{Bmatrix} \tag{6.3}$$

$$\begin{aligned} C_i^l &= \cos(l\omega\Delta t) \\ S_i^l &= \sin(l\omega\Delta t) \end{aligned} \tag{6.4}$$

N is the window block, y is the measured signal and $\hat{y}$ is the estimated signal. The magnitude is determined from the following equation:

$$\hat{M}_i(k) = \sqrt{\hat{x}_1(k)^2 + \hat{x}_2(k)^2} \tag{6.5}$$

Once the estimated magnitudes $\hat{M}_j$ are determined for all sensors, they are compared with those of the system matrix database. On-line selection of the best system matrix will be based on the least of norm error.

6.2 Sensor Location Selection

Figure 6.2 shows the numerical simulation results for critical damage identification. The critically damaged F/A-18 wing model (CASE 22) is used for this simulation. Figure 6.2 indicates the time history of the estimated magnitude of the sensor signal that are obtained from the short time Fourier analysis. The disturbance frequency is around 11 Hz which is very close to the flutter frequency. It was assumed that the sampling frequency is 80 Hz and that N=40. As shown in Figure 6.2, the numerical simulation establishes that the magnitude of the sensors can be estimated very accurately; therefore, the algorithm can effectively be used to identify the critical damage case.

Based on the short-time Fourier analysis, it is found that the four sensors at wing-tip (ID-2076, ID-2017, ID-2093, and ID-2104) are selected for system identification. However, based on Boeing's suggestions, two existing sensors in the fuselage are subsequently selected to replace two wing-tip sensors, namely ID-2093 and ID-2104.

(a) ID2093, Mag_{EXACT}=85

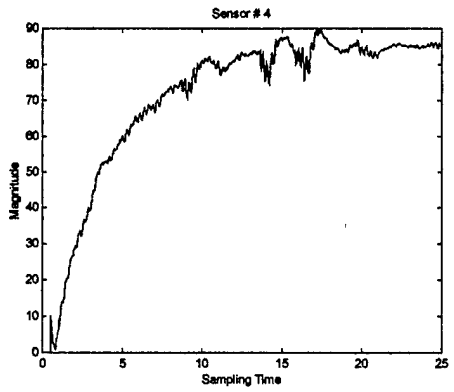

(b) ID2076, Mag_{EXACT}=118

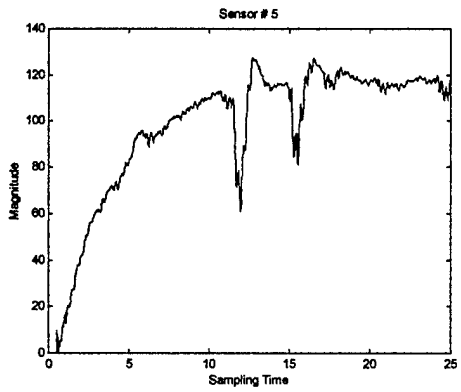

(c) ID1055, Mag_{EXACT}=52

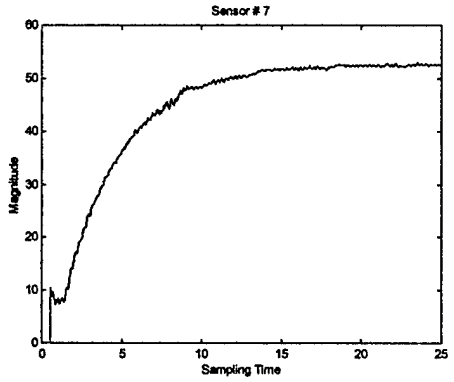

(d) ID1163, Mag_{EXACT}=115

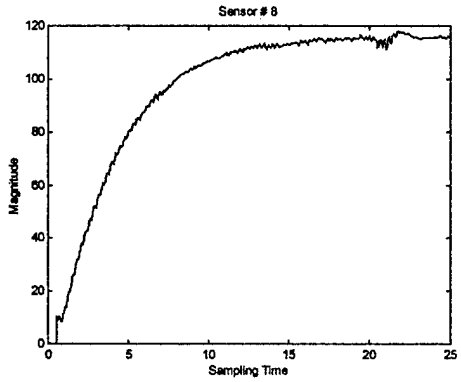

(e) ID2104, Mag_{EXACT}=314

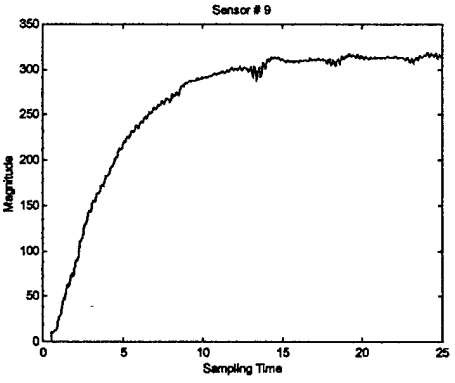

(f) ID2017, Mag_{EXACT}=487

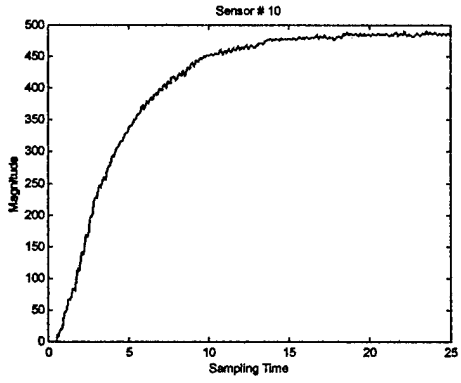

Figure 6.2 Time Response of the Estimated Magnitude of the Sensors Obtained from the Short-Time Fourier Analysis

SECTION 7

COMBINING FLIGHT DYNAMICS WITH ASE STATE SPACE EQUATIONS

To retrofit a production aircraft such as F/A-18 with an ASE reconfigurable adaptive control system, it is important to develop it with a modular architecture that can minimize the impact on the existing flight dynamics control system. Such a modular ASE/flight dynamics control system is proposed in Figure 7.1.

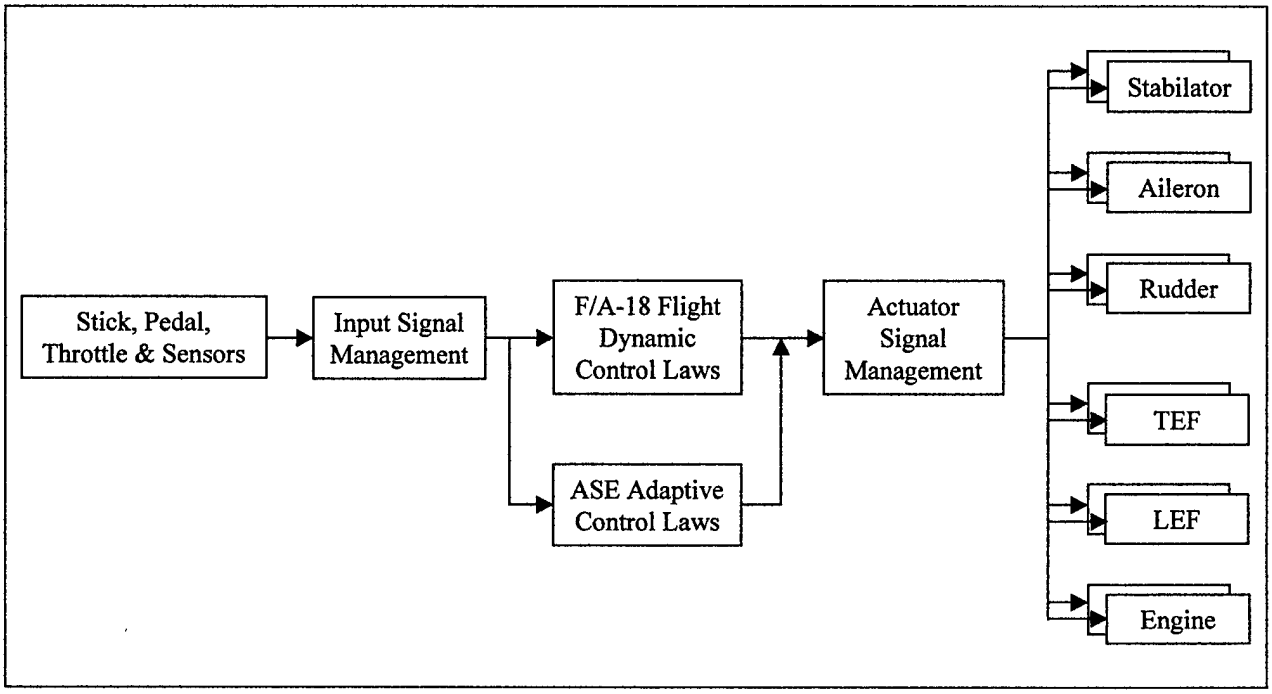

Figure 7.1 Modular ASE/Flight Dynamics Control System

This modular control system has the following merit:

- Minimum modification to the existing flight dynamic control system implies minimum cost.
- It is easier to verify the performance of the flight control laws with and without the ASE control system through a real-time simulation.
- The ASE control system can be switched off via a pilot disengagement.

The first step of achieving such a modular ASE control system is to generate the ASE state space equation such that its states of the rigid-body modes can be expressed in terms of the airframe states while keeping the states of the flexible modes unaltered. Once this is accomplished, the matrices A_{FD}, B_{FD} and C_{FD} in the flight dynamics state-space equations, expressed in the following equation

$$\begin{aligned}\{\dot{\mathbf{x}}_{FD}\} &= [A_{FD}]\{\mathbf{x}_{FD}\} + [B_{FD}]\{u\} \\ \{\mathbf{y}_{FD}\} &= [C_{FD}]\{\mathbf{x}_{FD}\}\end{aligned} \tag{7.1}$$

can be used to replace their corresponding submatrices in the ASE state space equations shown as follows

replaced by $[A_{FD}]$

replaced by $[B_{FD}]$

$$\begin{Bmatrix}\dot{\mathrm{x}}_{\mathrm{R}} \\ \dot{\mathrm{x}}_{\mathrm{e}}\end{Bmatrix} = \begin{bmatrix}A_{RR} & A_{\mathrm{Re}} \\ A_{eR} & A_{ee}\end{bmatrix}\begin{Bmatrix}\mathrm{x}_{\mathrm{R}} \\ \mathrm{x}_{\mathrm{e}}\end{Bmatrix} + \begin{bmatrix}B_R \\ B_e\end{bmatrix}\{\mathrm{u}\}$$

replaced by $[C_{FD}]$

$$\begin{Bmatrix}\mathrm{y}_{\mathrm{R}} \\ \mathrm{y}_{\mathrm{e}}\end{Bmatrix} = \begin{bmatrix}C_{RR} & C_{\mathrm{Re}} \\ C_{eR} & C_{ee}\end{bmatrix}\begin{Bmatrix}\mathrm{x}_{\mathrm{R}} \\ \mathrm{x}_{\mathrm{e}}\end{Bmatrix} \tag{7.2}$$

where the subscripts R and e denote the rigid-body states and flexible system states, respectively.

In the following section, this generalization of the ASE state space equations will be subjected to two coordinate transformation in order to be properly defined in the airframe states.

7.1 Coordinate Transformations of the Rigid-Body Modes

For a free-free structure, the NASTRAN FEM analysis can generally provide six rigid-body modes whose degrees of freedom (d.o.f.) are expressed in the generalized coordinates $\{\mathbf{q}\}$ as shown in Figure 7.2 (a).

The generalized coordinates of the rigid-body d.o.f. relate that the six rigid-body modes are expressed in the principle-axis coordinate. A coordinate transformation can be formulated to transform $\{\mathbf{q}\}$ to the rigid-body d.o.f. in the body axis $\{\mathbf{x}_{\mathrm{R}}\}$ (see Figure 7.2 (b)). In fact, such a coordinate transformation has already been included in the ZAERO software system which reads

$$\{\mathbf{q}\} = [R_p]^{-1}[R_{\mathrm{B}}]\{\mathbf{x}_{\mathrm{R}}\} \tag{7.3}$$

where $[R_p]$ and $[R_{\mathrm{B}}]$ are the 6 x 6 rigid-body displacements at a reference grid point of the FEM model in the generalized coordinates and body axis, respectively.

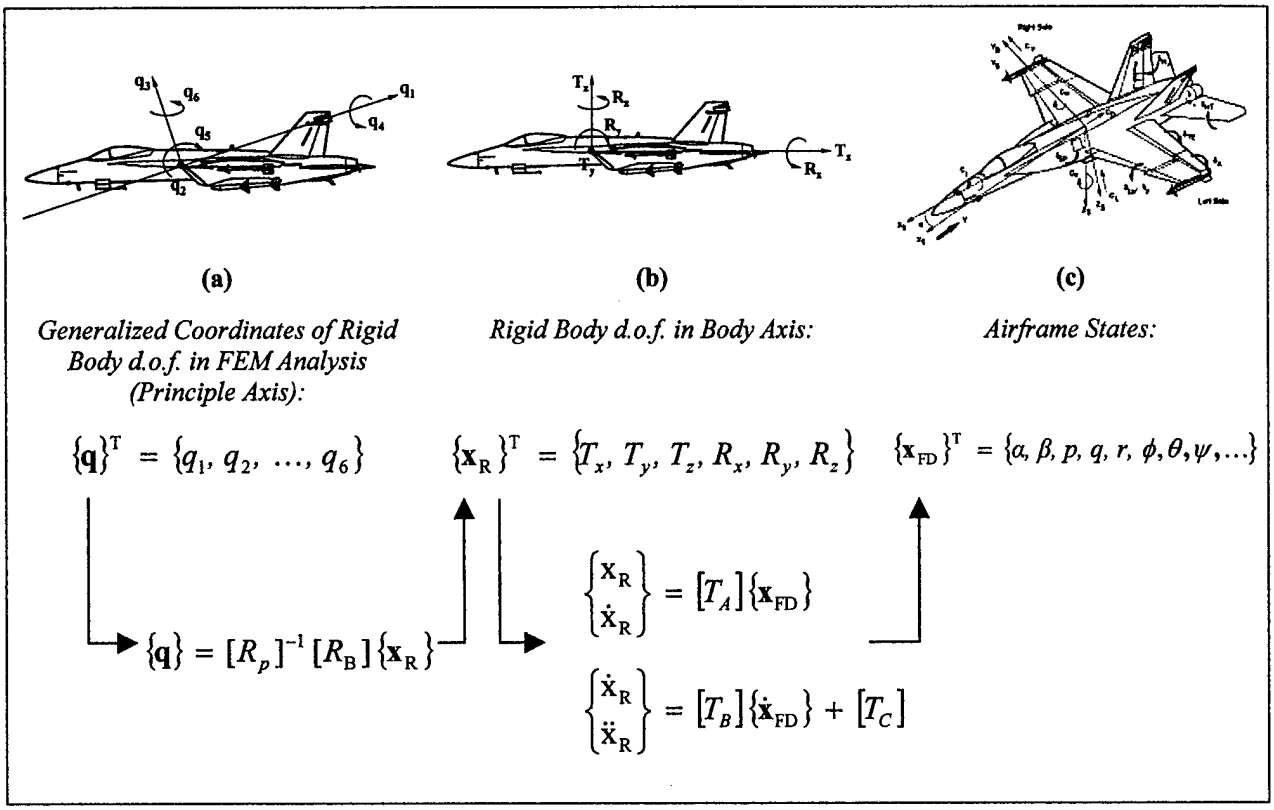

Figure 7.2 Coordinate Transformations from Rigid-Body Generalized coordinates to Airframe States

Transformation from the body axis to the airframe states depends on the definition of the airframe states. Generally, three transformation matrices are sufficient to express $\{\mathbf{x}_R\}$ in terms of airframe states $\{\mathbf{x}_{FD}\}$ (see Figure 7.2. (c)). These three transformation matrices $[T_A]$, $[T_B]$, and $[T_C]$ are shown in the following equations

$$\begin{Bmatrix} \mathbf{x}_R \\ \dot{\mathbf{x}}_R \end{Bmatrix} = [T_A]\{\mathbf{x}_{FD}\}$$
$$\begin{Bmatrix} \dot{\mathbf{x}}_R \\ \ddot{\mathbf{x}}_R \end{Bmatrix} = [T_B]\{\dot{\mathbf{x}}_{FD}\} + [T_C] \tag{7.4}$$

An example of these three matrices for lateral/directional airframe state is given in the next section.

7.2 Coordinate Transformations for the Lateral/Directional Airframe States

The objective of this example is to transform the three rigid-body d.o.f. (T_y, R_x, R_z) of NASTRAN generated anti-symmetric rigid-body modes, namely y translation, roll and yaw modes to the five lateral/directional states, $\{\mathbf{x}_{FD}\}^T = \{\beta, p, r, \varphi, \psi\}$.

First, the transformation of Eq (7.3) from the generalized coordinates to the body axis of the three anti-symmetric rigid-body d.o.f. results in the conversion of the generalized mass matrix to physical mass and moments of inertia, i.e.

$$\begin{bmatrix} \ddots & & \\ & m_i & \\ & & \ddots \end{bmatrix} \rightarrow \begin{bmatrix} M & 0 & 0 \\ 0 & I_{xx} & -I_{xz} \\ 0 & -I_{xz} & I_{zz} \end{bmatrix} \tag{7.5}$$

where m_i is the diagonal terms of the generalized mass matrix, and M, I_{xx}, I_{xz} and I_{zz} are the physical mass and moments of inertia of the aircraft.

This transformation also converts the definition of the rigid-body static aerodynamic stability and damping derivatives from the generalized coordinates to the body axis.

Since the $[\mathbf{A}_0]$ and $[\mathbf{A}_1]$ matrices of the Minimum State (MIST) method for rational aerodynamic approximation are associated with the aerodynamic stiffness and damping, they can be correlated with the static aerodynamic stability and damping derivatives as

$$[\mathbf{A}_0] = -\begin{bmatrix} 0 & 0 & Y_\beta \\ 0 & 0 & L_\beta \\ 0 & 0 & N_\beta \end{bmatrix} \tag{7.6}$$

$$[\mathbf{A}_1] = -\begin{bmatrix} (1/b)Y_\beta, & (V/b)Y_p, & (V/b)(Y_{\dot\beta} + Y_r) \\ (1/b)L_\beta, & (V/b)L_p, & (V/b)(L_{\dot\beta} + L_r) \\ (1/b)N_\beta, & (V/b)N_p, & (V/b)(N_{\dot\beta} + N_r) \end{bmatrix} \tag{7.7}$$

where

b = reference length

V = air speed

and Y, L and N are the side force, roll moment and yaw moment, respectively.

Eqs 7.6 and 7.7 suggest that the wind tunnel measured static aerodynamic stability and damping derivatives can be used to replace the ZAERO computed derivatives so that the resulting plant

matrix of the rigid-body d.o.f. is identical to that of the flight dynamics. In fact, this is an existing option in the ZAERO software system.

The three transformation matrices $[T_A], [T_B]$, and $[T_C]$ for lateral/directionl states can be established by using the following flight dynamics equations,

$$R_x = -\phi, \qquad \frac{\dot{T}_y}{V} = \beta, \qquad \dot{R}_x = -p - r\tan\theta$$

$$\dot{R}_z = -R\sec\theta \tag{7.8}$$

and

$$\ddot{T}_y = -g\cos\theta + V\dot{\beta} + Vr$$

Thus, the three transformation matrices of the five states from body axis $\{x_R, \dot{x}_R\}^T = \{R_x, R_z, \dot{T}_y, \dot{R}_x, \dot{R}_z\}$ to the airframe states $\{\mathbf{x}_{FD}\}^T = \{\beta, p, r, \varphi, \psi\}$ are:

$$\mathbf{T}_A = \begin{bmatrix} 0 & 0 & 0 & -1 & 0 \\ 0 & 0 & 0 & 0 & 0 \\ V & 0 & 0 & 0 & 0 \\ 0 & -1 & -\tan\theta & 0 & 0 \\ 0 & 0 & -\sec\theta & 0 & 0 \end{bmatrix}, \quad \mathbf{T}_B = \begin{bmatrix} 0 & 0 & 0 & -1 & 0 \\ 0 & 0 & 0 & 0 & -1 \\ V & 0 & 0 & 0 & 0 \\ 0 & -1 & -\tan\theta & 0 & 0 \\ 0 & 0 & -\sec\theta & 0 & 0 \end{bmatrix}, \quad \mathbf{T}_C = \begin{bmatrix} 0 & 0 & 0 & 0 & 0 \\ 0 & 0 & 0 & 0 & 0 \\ 0 & 0 & V & -g\cos\theta & 0 \\ 0 & 0 & 0 & 0 & 0 \\ 0 & 0 & 0 & 0 & 0 \end{bmatrix} \tag{7.9}$$

With these transformation matrices, the ASE state-space equation, Eq 7.2, becomes

$$\begin{Bmatrix} \dot{\mathbf{x}}_{FD} \\ \dot{\mathbf{x}}_e \end{Bmatrix} = \begin{bmatrix} T_B^{-1}[A_{RR}T_A \;\; -T_C], & T_B^{-1}A_{Re} \\ A_{eR}T_A, & A_{ee} \end{bmatrix} \begin{Bmatrix} \mathbf{x}_{FD} \\ \mathbf{x}_e \end{Bmatrix} + \begin{bmatrix} T_B^{-1}B_R \\ B_e \end{bmatrix} \{u\}$$

$$\begin{Bmatrix} \mathbf{y}_R \\ \mathbf{y}_e \end{Bmatrix} = \begin{bmatrix} C_{RR}T_A, & C_{Re} \\ C_{eR}T_A, & C_{ee} \end{bmatrix} \begin{Bmatrix} \mathbf{x}_{FD} \\ \mathbf{x}_e \end{Bmatrix} \tag{7.10}$$

Since the rigid-body states of the ASE state-space equations now arrive at the same definition of the airframe states, the submatrices $T_B^{-1}[A_{RR}T_A \;\; -T_C]$, $T_B^{-1}B_R$, and $C_{RR}T_A$ can be replaced by the matrices $[A_{FD}], [B_{FD}]$, and $[C_{FD}]$ of the airframe states in Eq 7.1. Moreover, Eq 7.10 indicates that the modular ASE control system can be formally obtained to combine with the existing flight dynamic control system. Note further that the coupling between these two systems is obtained through the off-diagonal submatrices in Eq 7.10.

SECTION 8

NUMERICAL SIMULATION OF CRITICAL DAMAGE/LCO CASES WITHOUT RIGID BODY STATES

In this section, the MATLAB numerical simulation of the three critical damage cases and the five LCO cases at M = 0.9, sea level are demonstrated. Two sensors at wing tip and two sensors in the fuselage are used for system outputs (Figure 8.1). Four control surfaces, namely aileron (AIL), trailing edge flap (TEF), inboard leading edge flap (ILEF) and outboard leading edge flap (OLEF) are employed for control input. Note that the rudders and horizontal tails are not included in all cases.

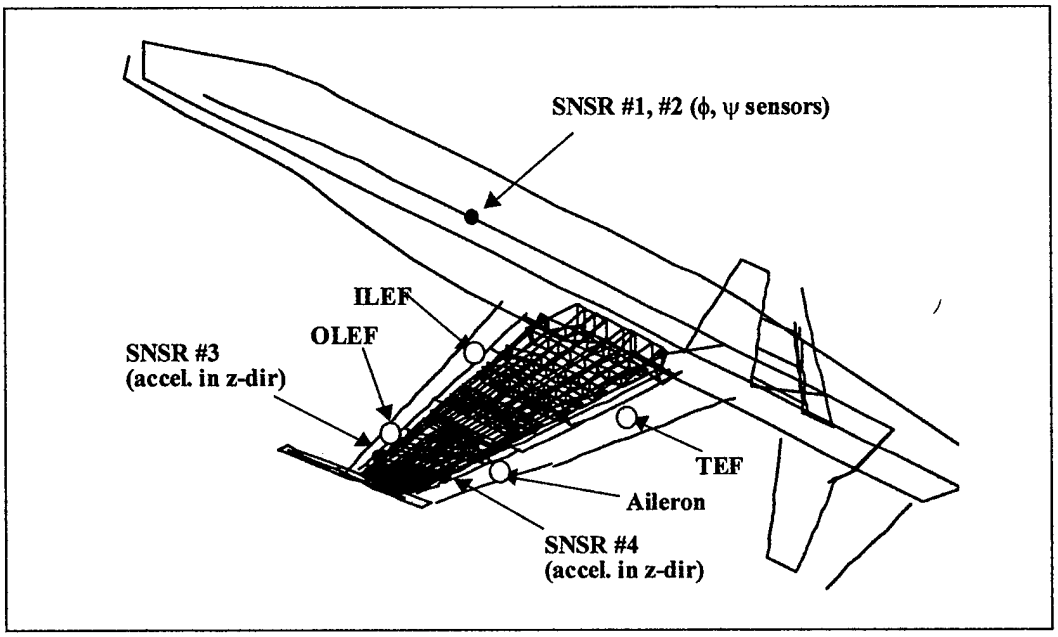

Figure 8.1 Sensors Placed on the F/A-18 Wing Model

Reduced-order ASE system matrices are first generated in the off-line analysis. The plant matrices include three flexible modes (excluding rigid-body degrees of freedom) and one aerodynamic states. A MATLAB database is established which contains the ASE system matrices of the three critical damage cases and five LCO cases. These ASE system matrices are used to provide the initial parameters for system identification.

8.1 Flutter Suppression of the Three Critical Damage Cases

The two wing-tip sensor outputs of the open-loop and closed-loop systems are presented in Figures 8.2, 8.4, and 8.6 of the critical damage cases 1, 2 and 3, respectively; and their corresponding control input time histories of the four control surfaces are in Figures 8.3, 8.5 and 8.7.

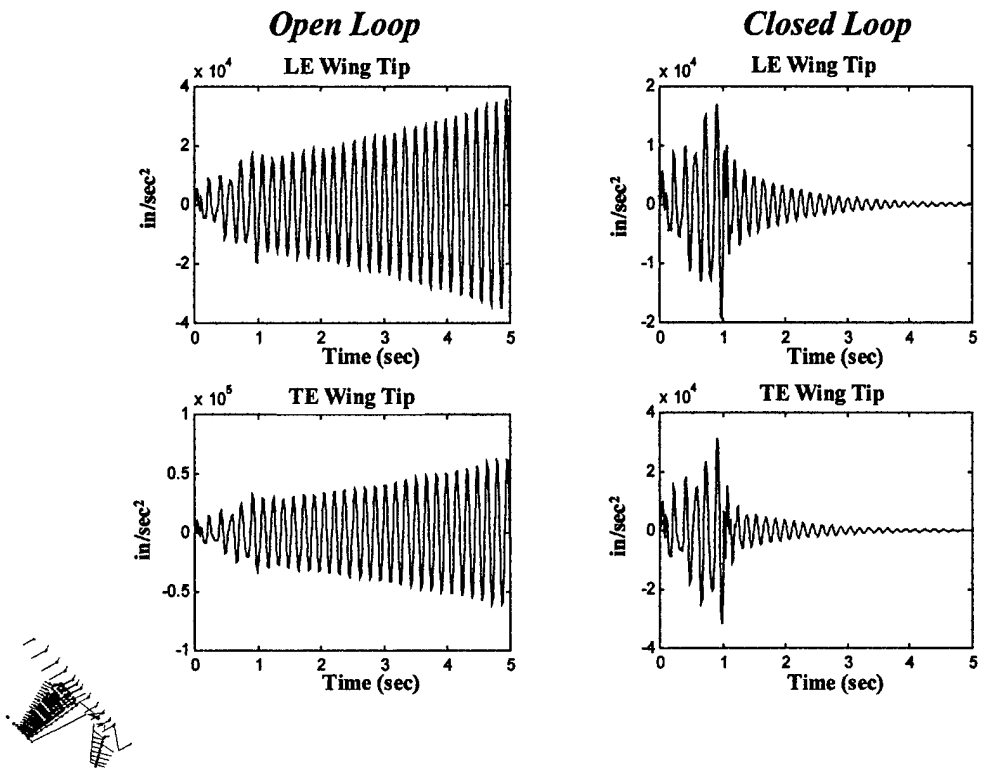

Figure 8.2 Critical Damage Case 1 – Open/Closed Loop Sensor Signal

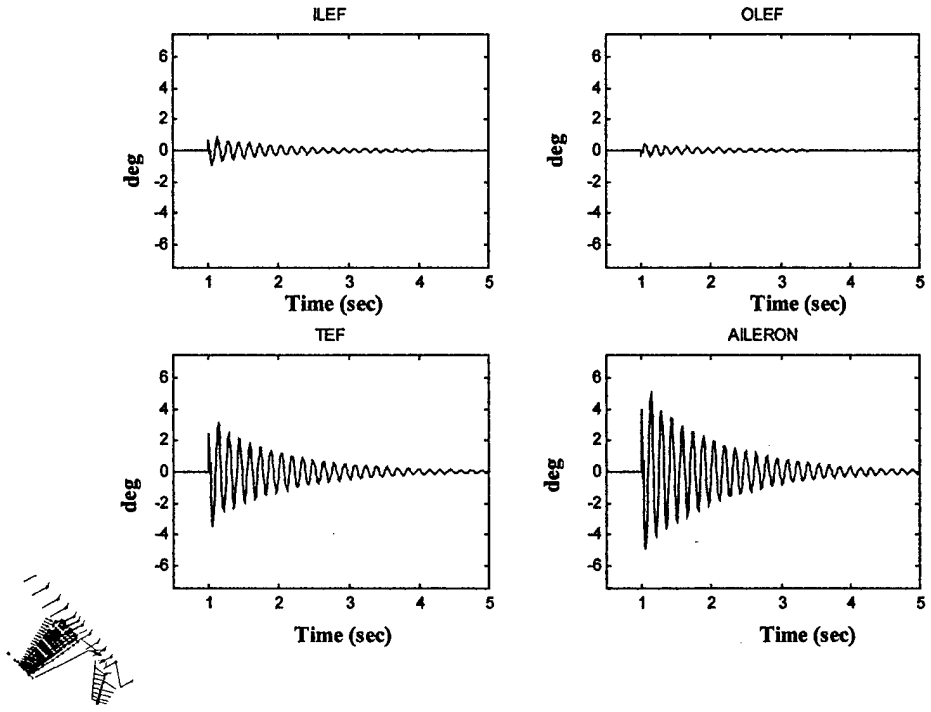

Figure 8.3 Critical Damage Case 1 – Control Surface Input

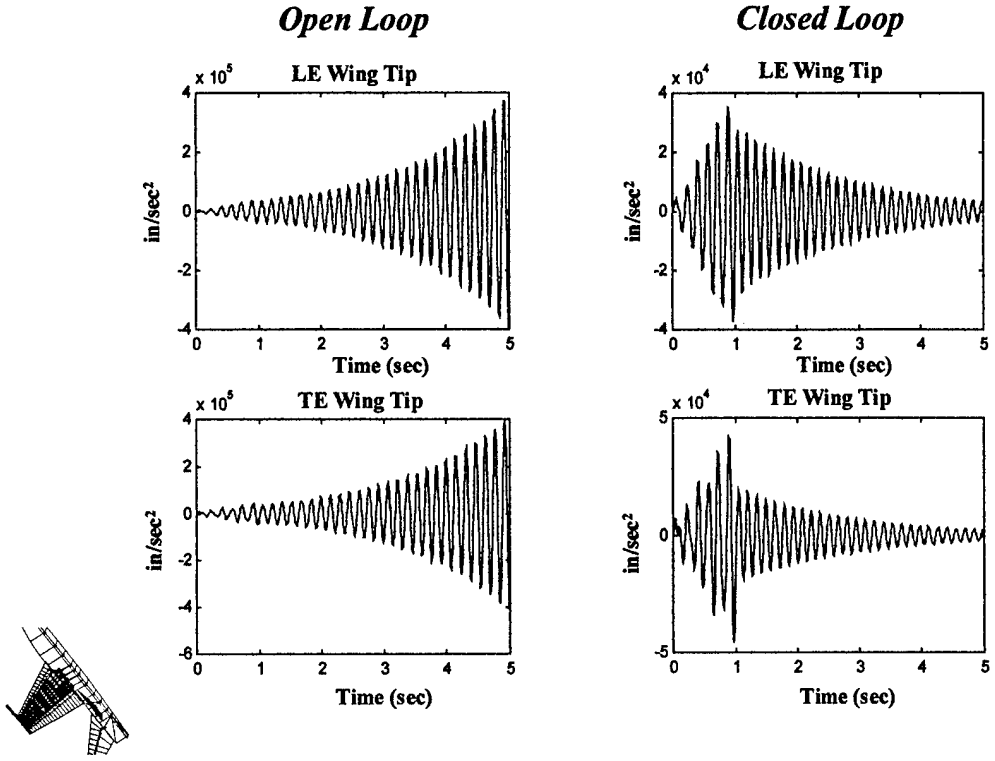

Figure 8.4 Critical Damage Case 2 – Open/Closed Loop Sensor Signal

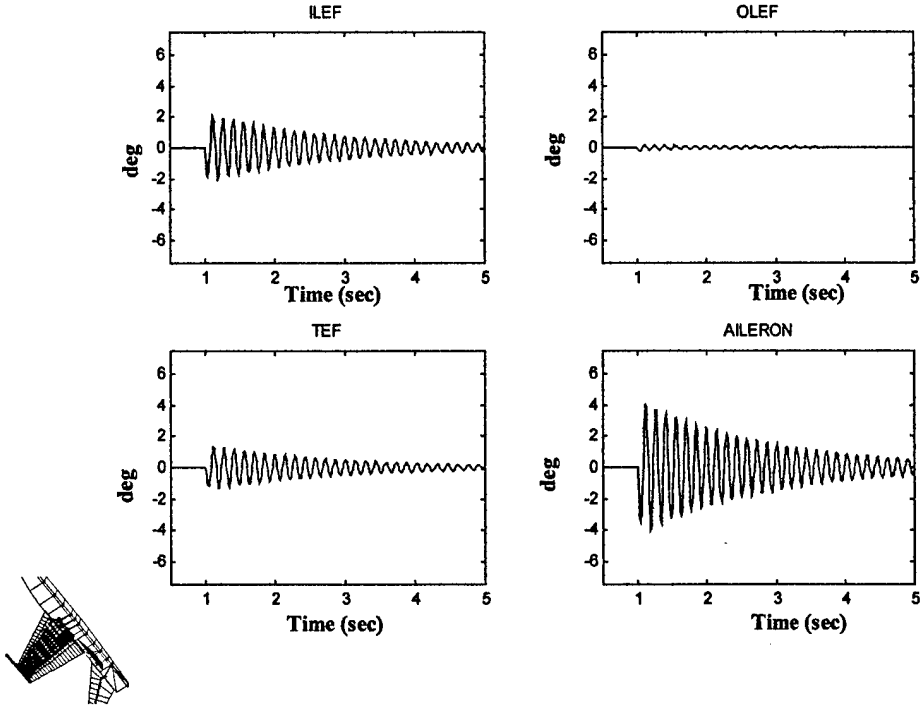

Figure 8.5 Critical Damage Case 2 – Control Surface Input

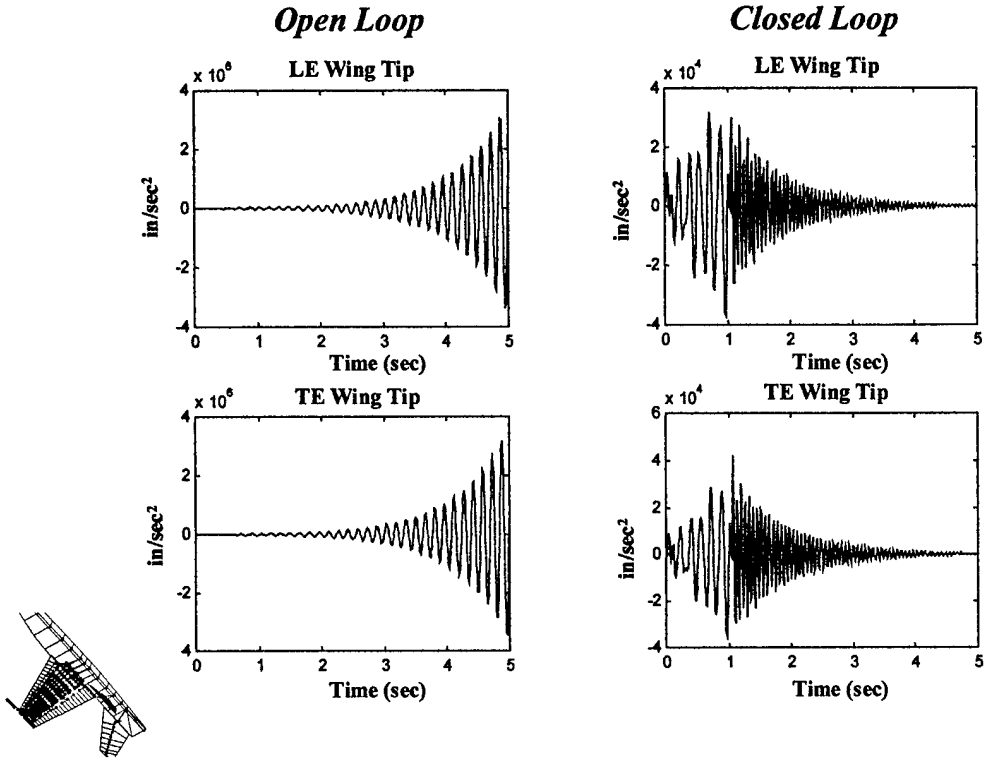

Figure 8.6 Critical Damage Case 3 – Open/Closed Loop Sensor Signal

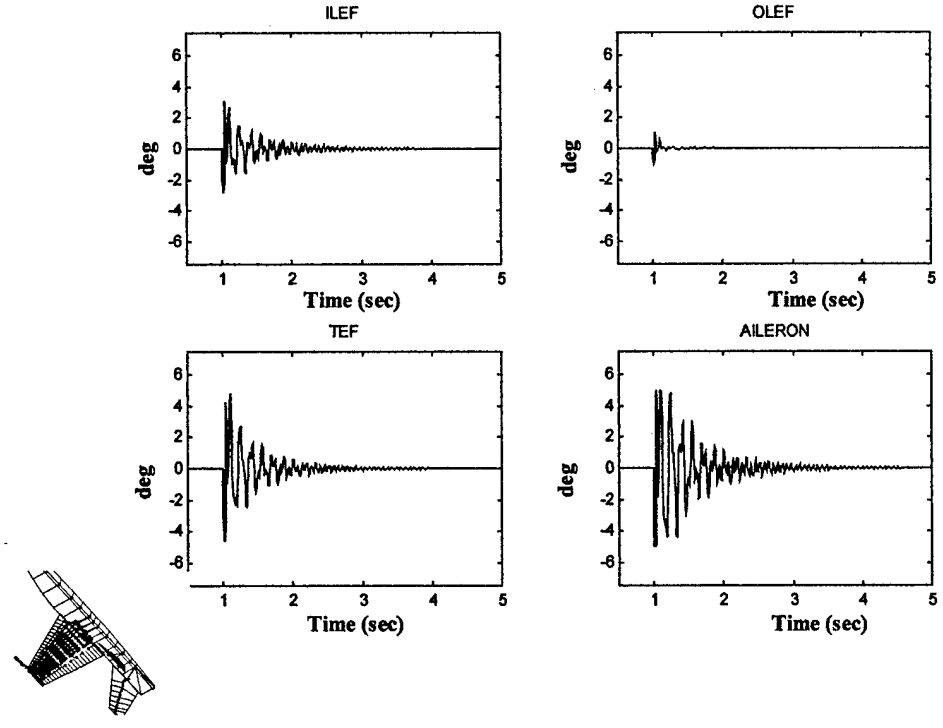

Figure 8.7 Critical Damage Case 3 – Control Surface Input

It can be seen that the developed Modal-Based Parameter Estimation (MPE) algorithm for system identification and Modified Model-Following Reconfigurable (MMFR) algorithm for reconfigurable adaptive control work well in concert for flutter suppression of all critical damage cases considered. Generally, MPE algorithm requires 1 second for system identification and the MMFR algorithm takes an additional 4 ~ 5 seconds for flutter suppression. Among the four control surfaces, the aileron requires the largest control input. This is expected since aileron has the best roll control effectiveness. Note that all three critical damage cases are rather violent flutter cases (see the open loop response in Figures 8.2, 8.4 and 8.6). The closed-loop responses on the other hand show that the developed adaptive reconfigurable control system is very effective, capable of suppressing the violent flutters within 5 seconds.

8.2 LCO Suppression of the Five LCO Cases

The sensor responses of the open-loop and closed-loop systems of the five LCO cases are presented in Figures 8.8, 8.10, 8.12, 8.14 and 8.16, respectively; and their respective control input time histories are depicted in Figure 8.9, 8.11, 8.13, 8.15 and 8.17. Note that the open-loop responses of all LCO cases here show mildly growing or likely sustained oscillations in contrast to the rather rapidly divergent oscillations of the previous critical damage cases of flutter. Therefore the developed reconfigurable adaptive control system should suppress the LCO more rapidly than the flutter instability of the damage cases. As expected, the closed-loop sensor responses show that the MPE algorithm requires only 0.2 second for system identification and the MMFR control algorithm takes approximately 2 seconds for LCO suppression. Also, the control input of the two leading edge flaps are much less effective than that of the aileron and the trailing-edge flap. This suggests that if only LCO suppression is considered, then the two leading-edge flaps can possibly be removed from the control system, thus reducing the complexity of the control system.

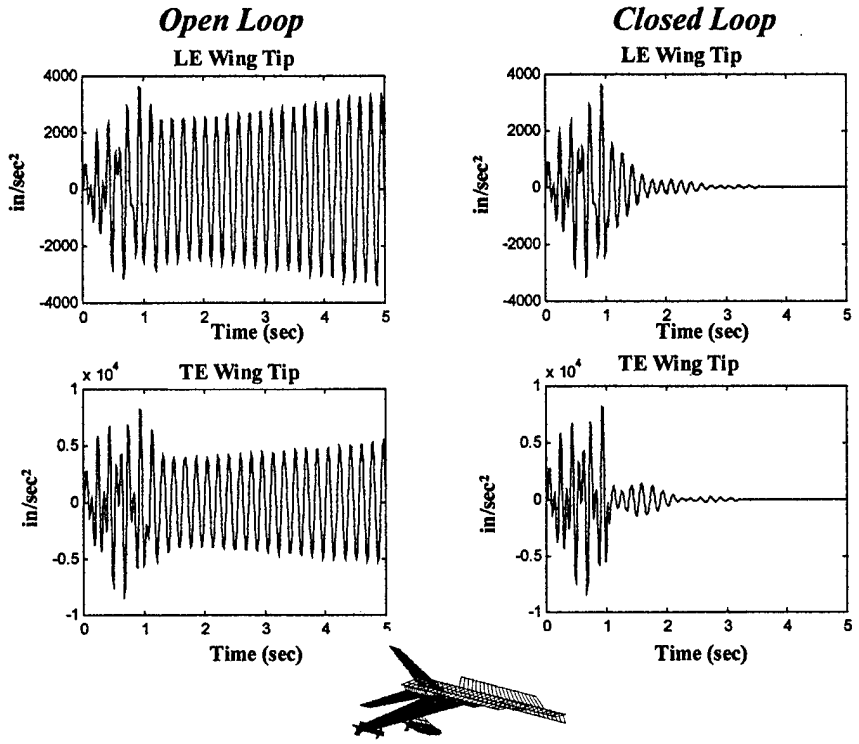

Figure 8.8 LCO Case 1 – Open/Closed Loop Sensor Signal

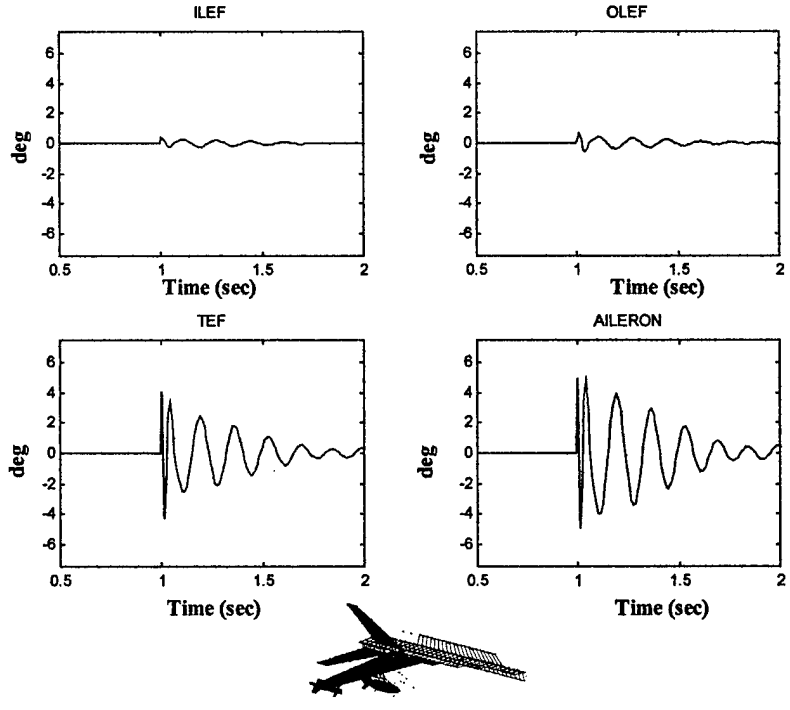

Figure 8.9 LCO Case 1 – Control Surface Input

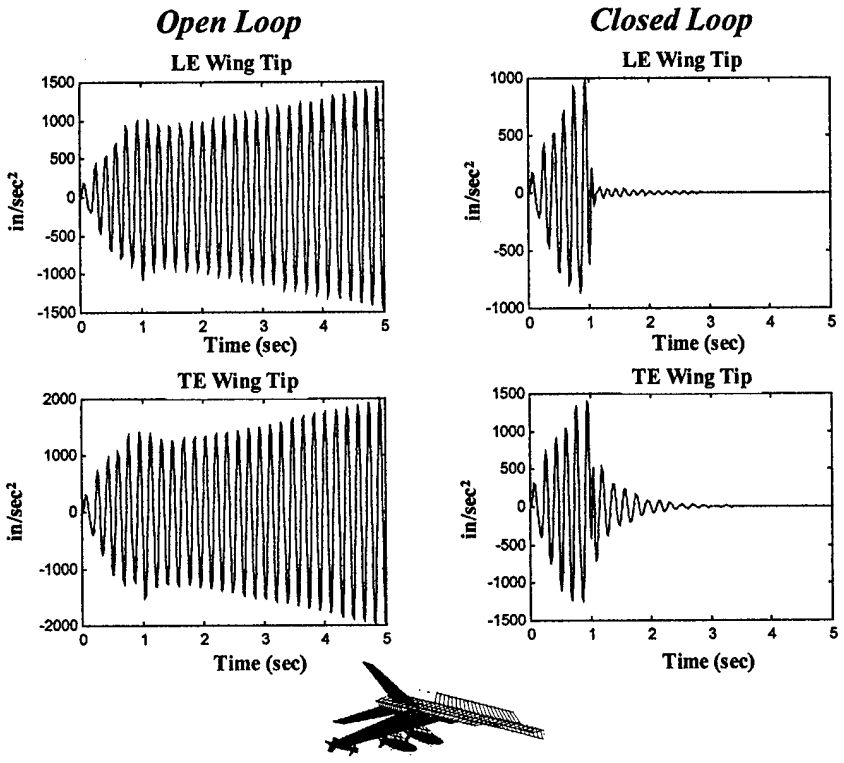

Figure 8.10 LCO Case 2 – Open/Closed Loop Sensor Signal

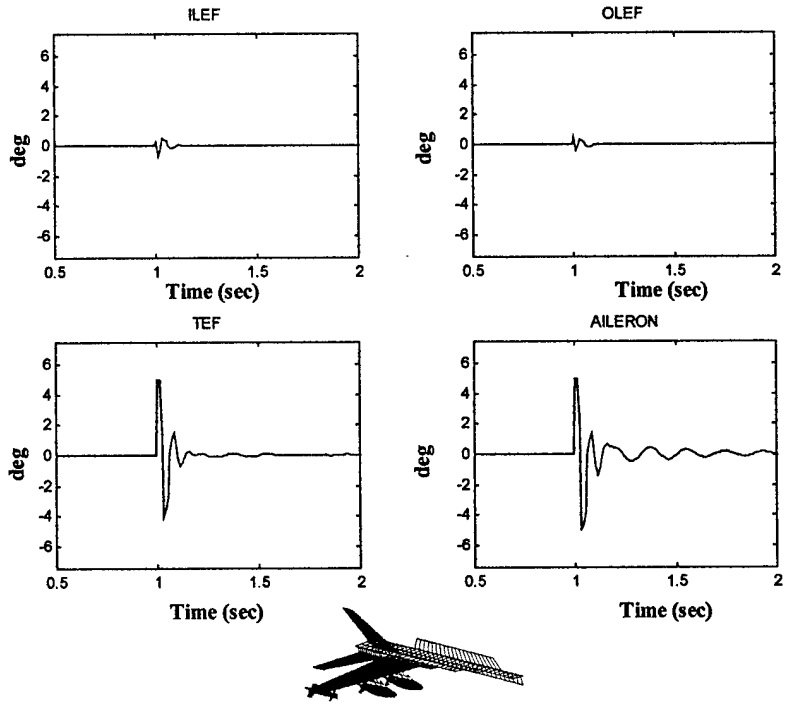

Figure 8.11 LCO Case 2 – Control Surface Input

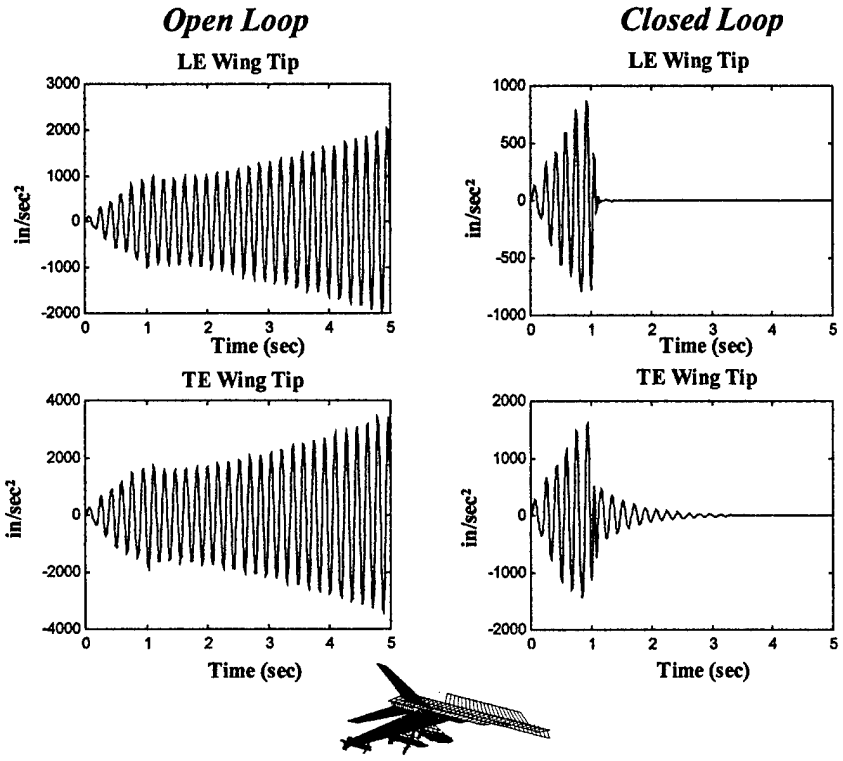

Figure 8.12 LCO Case 3 – Open/Closed Loop Sensor Signal

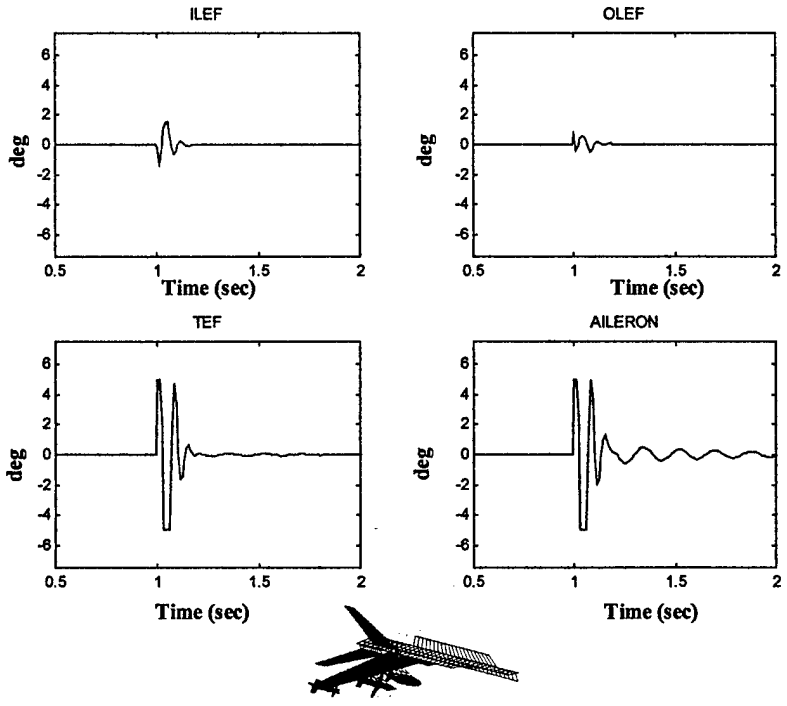

Figure 8.13 LCO Case 3 – Control Surface Input

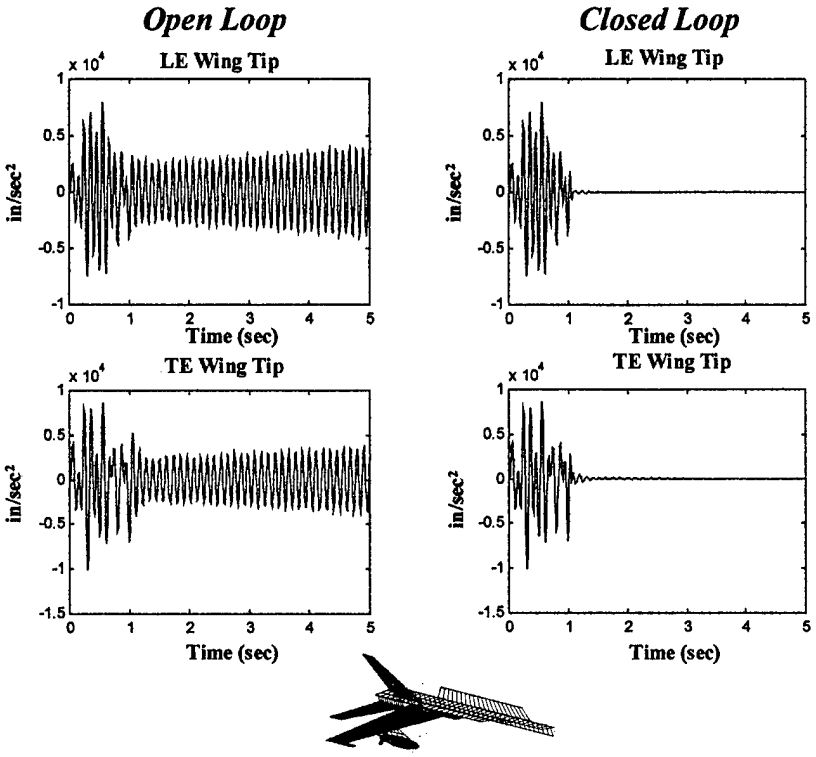

Figure 8.14 LCO Case 4 – Open/Closed Loop Sensor Signal

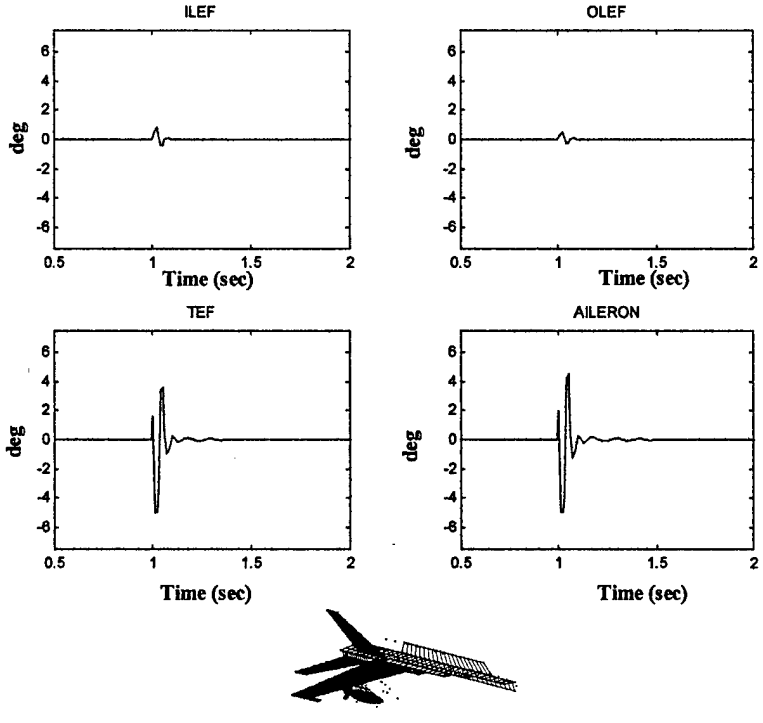

Figure 8.15 LCO Case 4 – Control Surface Input

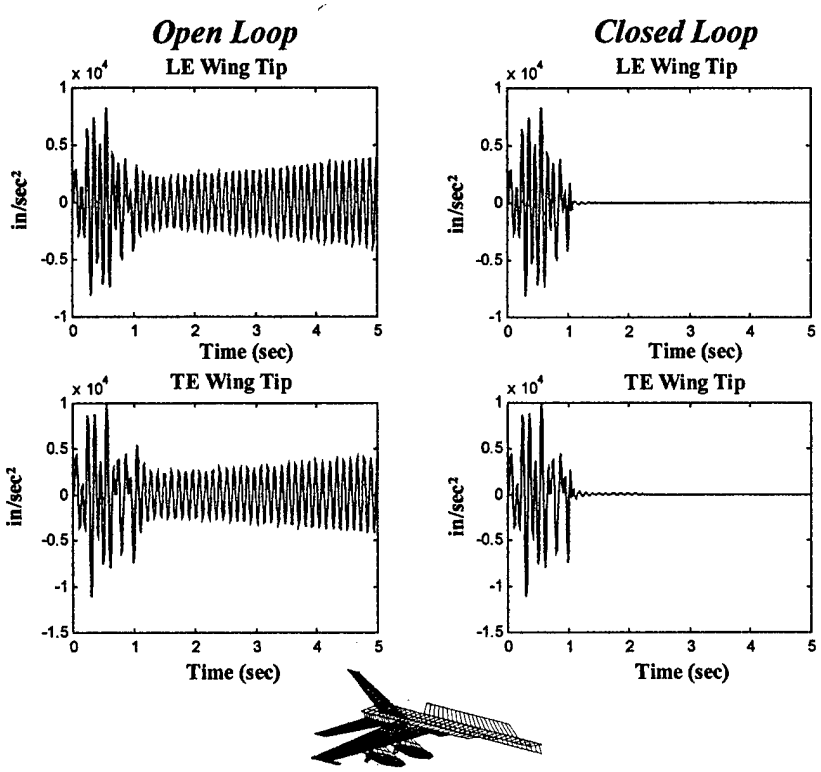

Figure 8.16 LCO Case 5 – Open/Closed Loop Sensor Signal

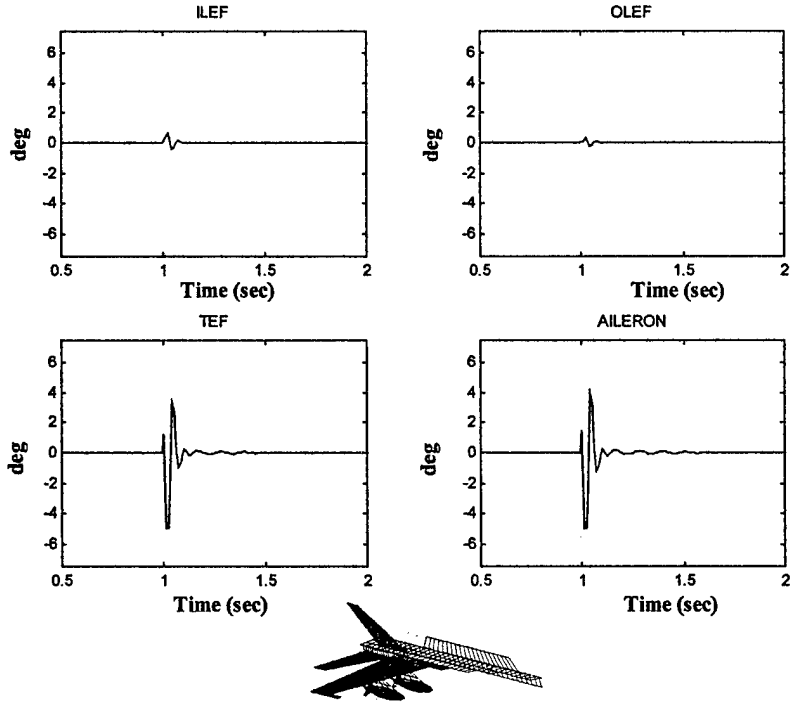

Figure 8.17 LCO Case 5 – Control Surface Input

SECTION 9

NUMERICAL SIMULATION OF THE LCO CASES WITH RIGID BODY STATES

In this section, numerical simulation results are presented to demonstrate the effectiveness of our two reconfiguration adaptive control (RAC) systems as applied to a flexible airframe system with five added airframe states of rigid-body degrees of freedom. These two control systems are:

1. The ASE alone control system without the RBF control system (Section 9.1)
2. Modular ASE control system combined with the RBF control system (Section 9.2)

Here, a case similar to the previous LCO Case 1 is considered. Explicitly, five airframe states of the rigid-body degrees of freedom, namely *Beta*, *p*, *r*, *Phi* and *Psi* are added in the ASE state-space equations.

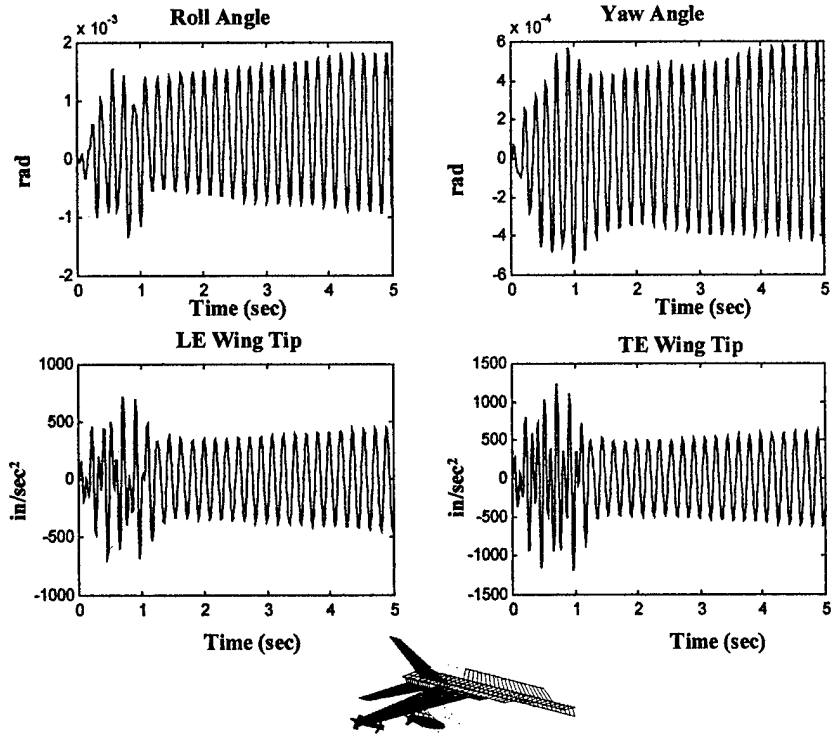

Figure 9.1 LCO/RBF System – Open Loop Sensor Signal

9.1 LCO Suppression with Rigid Body States: ASE Alone Control System Cases

The case considered here is identical to the LCO Case 1 in Section 8, except that five rigid body states are included. The present case is defined as one combines LCO with rigid body flight dynamics (LCO/RBF). Figure 9.1 shows the open-loop sensor signals of the roll angle and yaw angle measured by two sensors in the fuselage and wing-tip accelerations at the two wing-tip sensors.

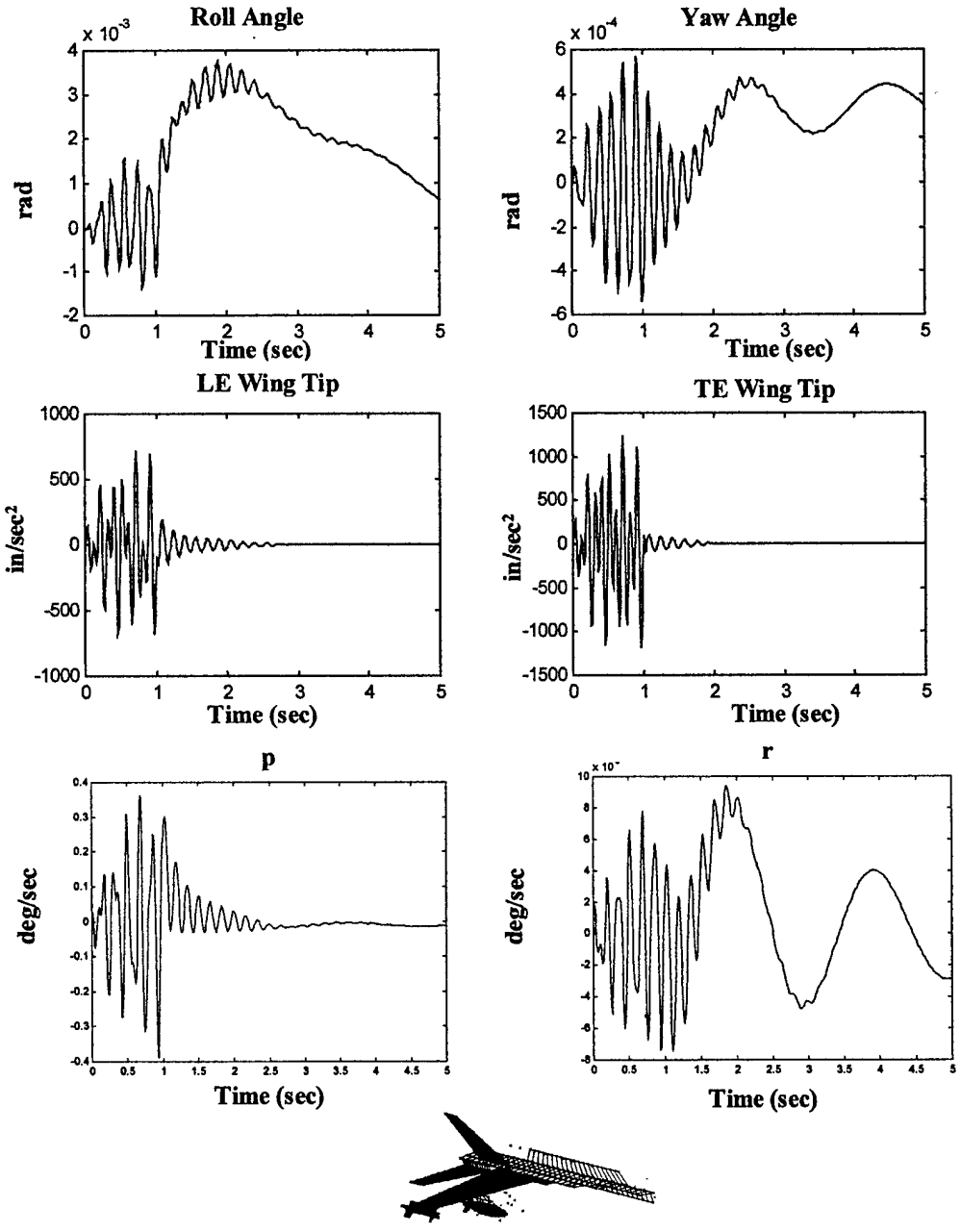

Figure 9.2 LCO/RBF System – Closed Loop Sensor Signal

From these open-loop sensor signals, the wing oscillation and the rigid body oscillation induced by LCO can be clearly seen. The sensor signals and the control input of the closed-loop system are presented in Figures 9.2 and 9.3, respectively. It can be seen that the ASE adaptive reconfigurable control system can suppress the wing oscillation within one second, but it cannot suppress the rigid-body oscillation more rapidly. This is expected since the rudders are not included as a control input in the ASE (alone) control system.

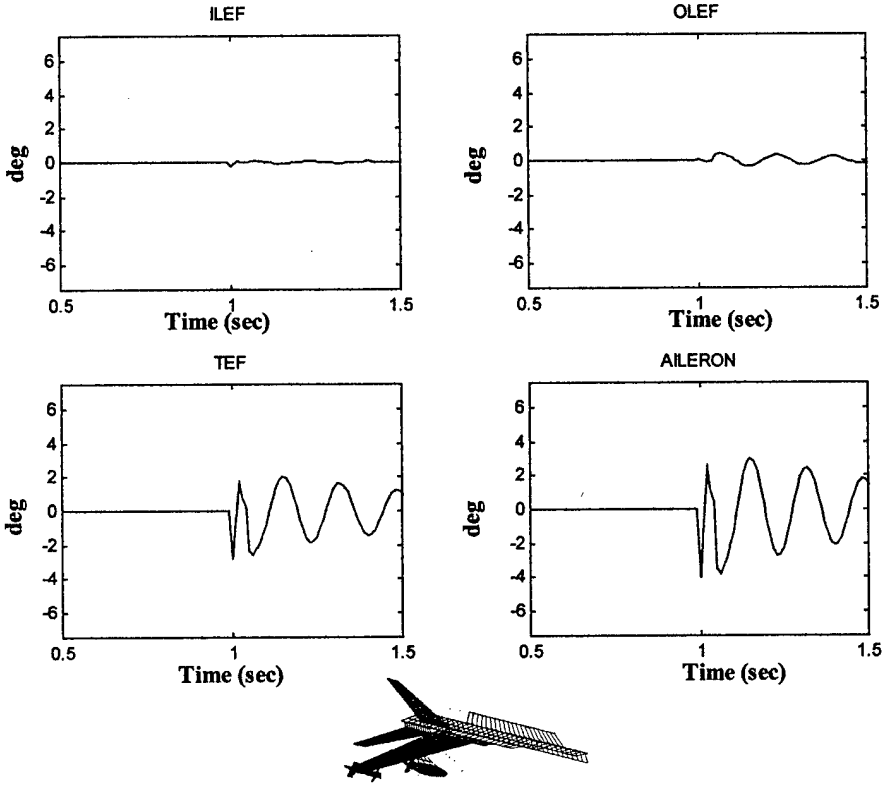

Figure 9.3 LCO/RBF System – Control Surface Input

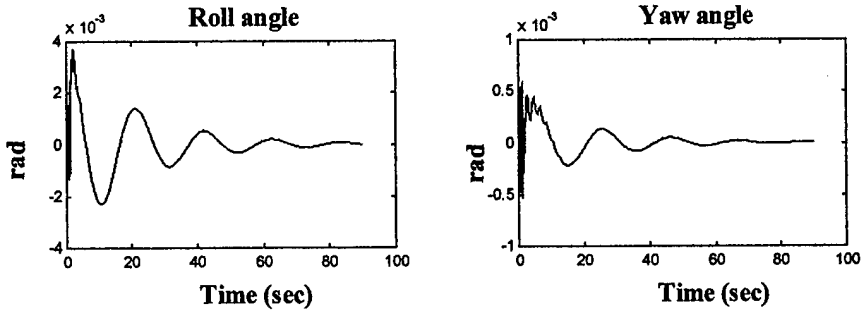

Figure 9.4 LCO/RBF System – Closed Loop Sensor Signal: 100 Seconds

Here, the four control surfaces on the wing have little yaw control effectiveness (since there is no rudder input), suppression of the lateral/direction rigid body oscillation rapidly would be difficult. However, Figure 9.4 shows that, even with little yaw control effectiveness, the ASE control system can eventually suppress the rigid-body oscillation, except that it takes much longer time (100 seconds) than it would to suppress the wing oscillation.

9.2 Modular RBF-ASE Control System for LCO Suppression

Figure 9.5 shows an existing F/A-18 lateral/directional rigid body flight dynamics (RBF) control system supplied by Boeing/St. Louis. There are 5 airframe states, 8 control surfaces and 12 outputs of the RBF control system, all of which are described in Table 9.1.

Table 9.1 States, Controls and Outputs of the F/A-18 RBF Control System

STATES	CONTROLS	OUTPUTS
Beta → Vehicle Side-Slip Angle	Surface Deflections	*Beta* → Vehicle Side-Slip Angle
p → Body Roll Rate	Aileron (AIL)	*p* → Body Axis Roll Rate
r → Body Yaw Rate	Trailing Edge Flap (TEF)	*r* → Body Axis Yaw Rate
Phi → Body Roll Attitude	Leading Edge Flap (LEF)	*Phi* → Body Roll Attitude
Psi → Body Yaw Attitude	Horizontal Stabilizer (STAB)	*Psi* → Body Yaw Attitude
		NYcg → Body Lateral Acceleration at CG
		NYsens → Body Lateral Acceleration at accelerometer g
		psens → Body Axis Roll Rate
		rsens → Body Axis Yaw Rate
		Betadot → Time Rate of Change of Side-Slip Angle
		pdot → Body Axis Roll Angular Acceleration
		rdot → Body Axis Yaw Angular Acceleration

For a given 0.2 inch stick command, the response of the F/A-18 RBF closed-loop system is computed using the MATLAB/SIMULINK tool box and shown in Figure 9.6. Note that Figure 9.6 is the results of the baseline RBF system response, whereas no LCO is present.

The objective of the case considered is to demonstrate that the developed ASE control system can work in parallel with a given RBF control system. This is to say that the RBF and ASE control systems can operate independently as two separated modules but sharing the common inputs and outputs, i.e., the control surfaces AIL, TEF, LEF and the five outputs *Beta*, *p*, *r*, *Phi* and *Psi*. The RBF system is responsible for rigid body control, whereas the ASE system for LCO suppression. Such a modular RBF-ASE control system design is shown in Figure 9.7.

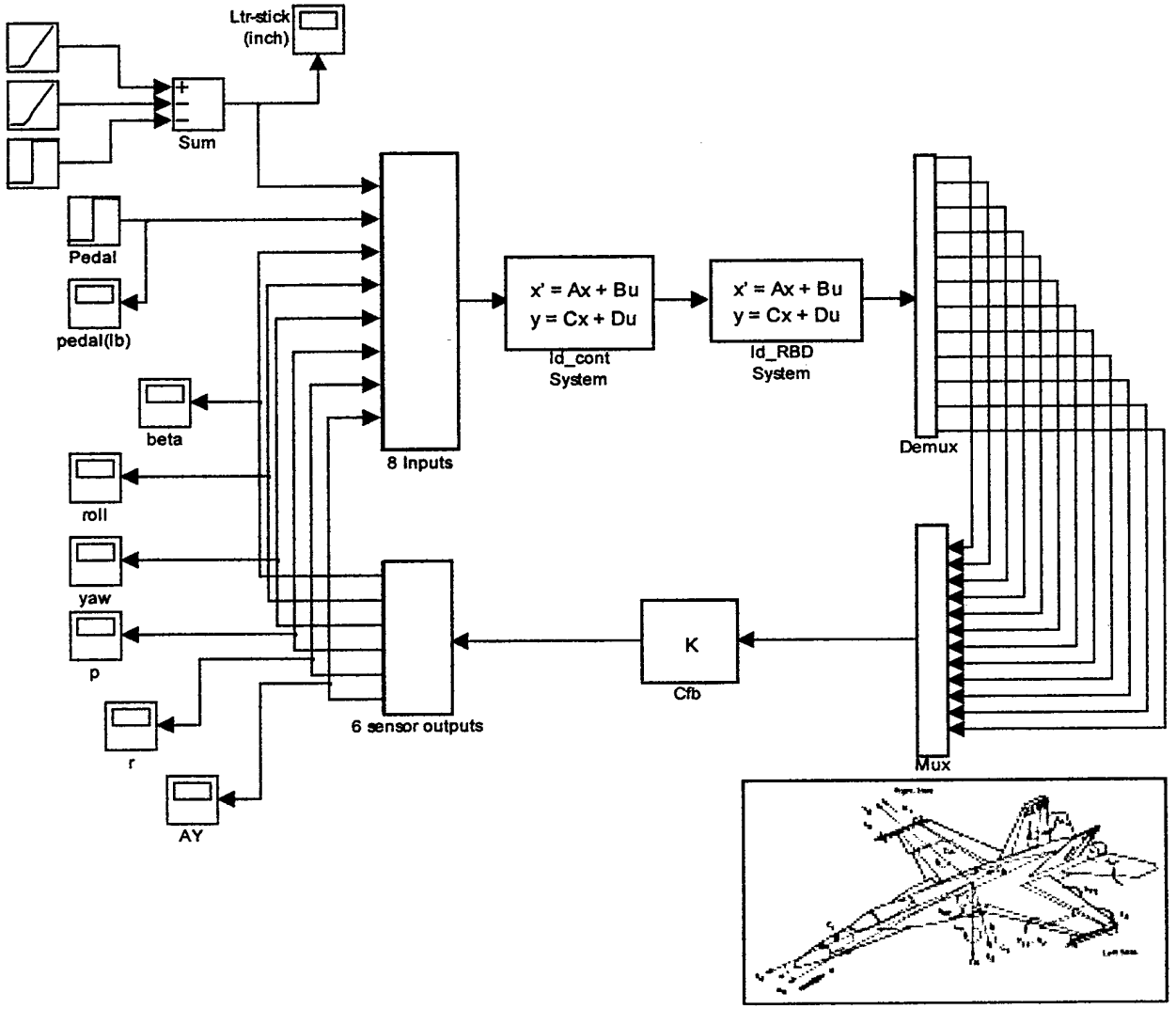

Figure 9.5 The F/A-18 Lateral/Directional Rigid-Body Flight Dynamic (RBF) Control System

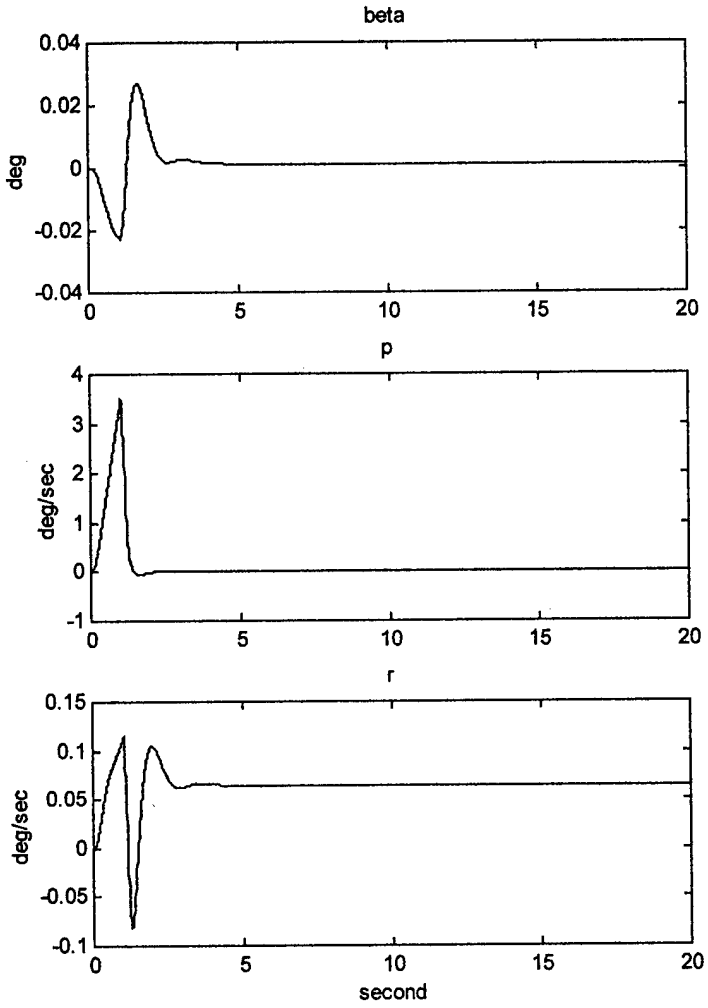

Figure 9.6 The F/A-18 RBF Response due to a 0.2 inch Stick Command

Figure 9.8 presents the rigid body responses of the modular RBF-ASE control system due to a 0.2 inch stick command. Comparing Figure 9.8 to Figure 9.6, one can see that the rigid body responses of the modular RBF-ASE control system and that of the baseline RBF control system are nearly identical, except that the RBF-ASE control system takes a slightly longer time to suppress the side-slip angle oscillation. This difference in side-slip angles is caused by the additional input from the ASE system for LCO suppression which induces additional side-slip angle oscillation.

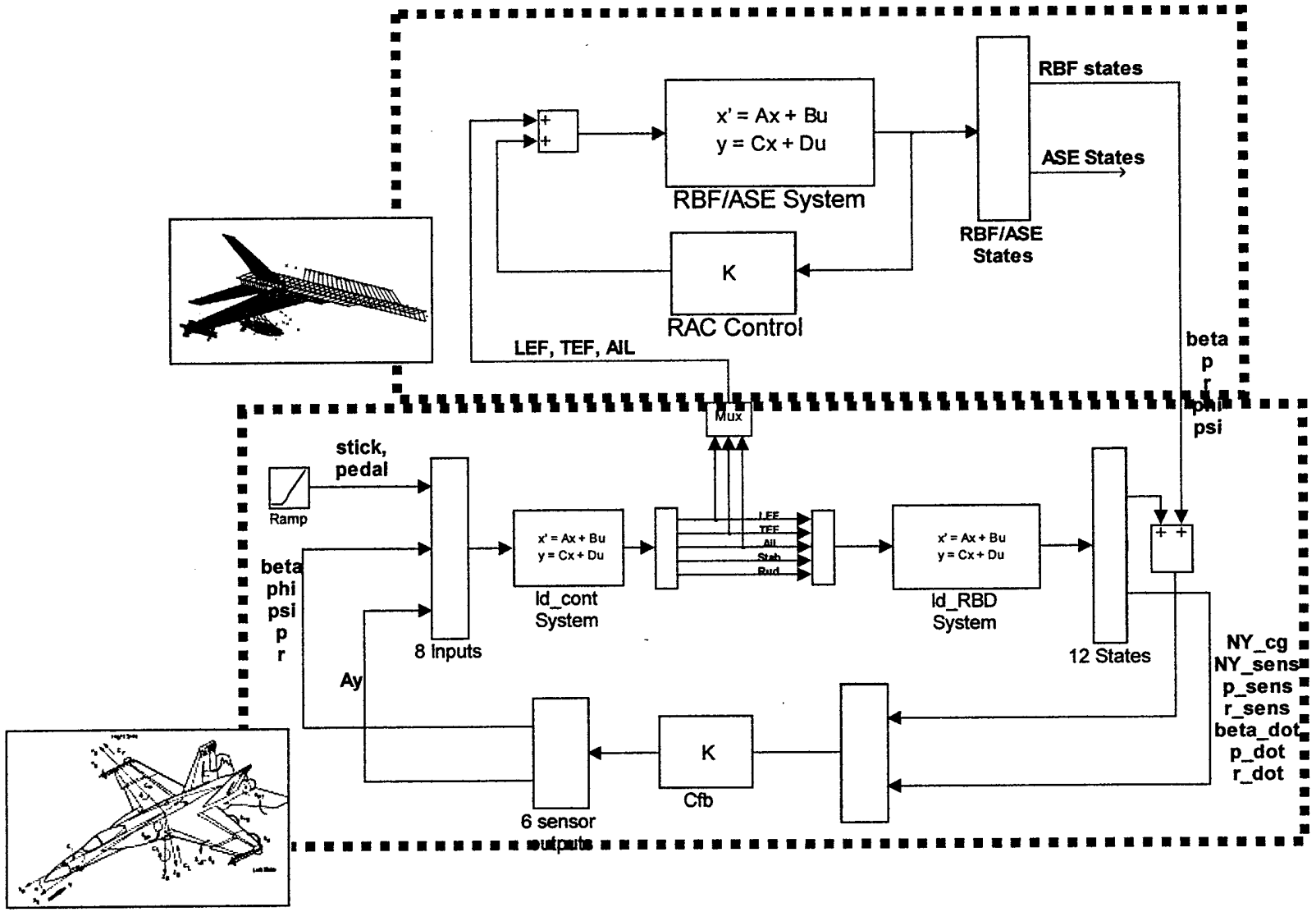

Figure 9.7 Modular RBF-ASE Control System

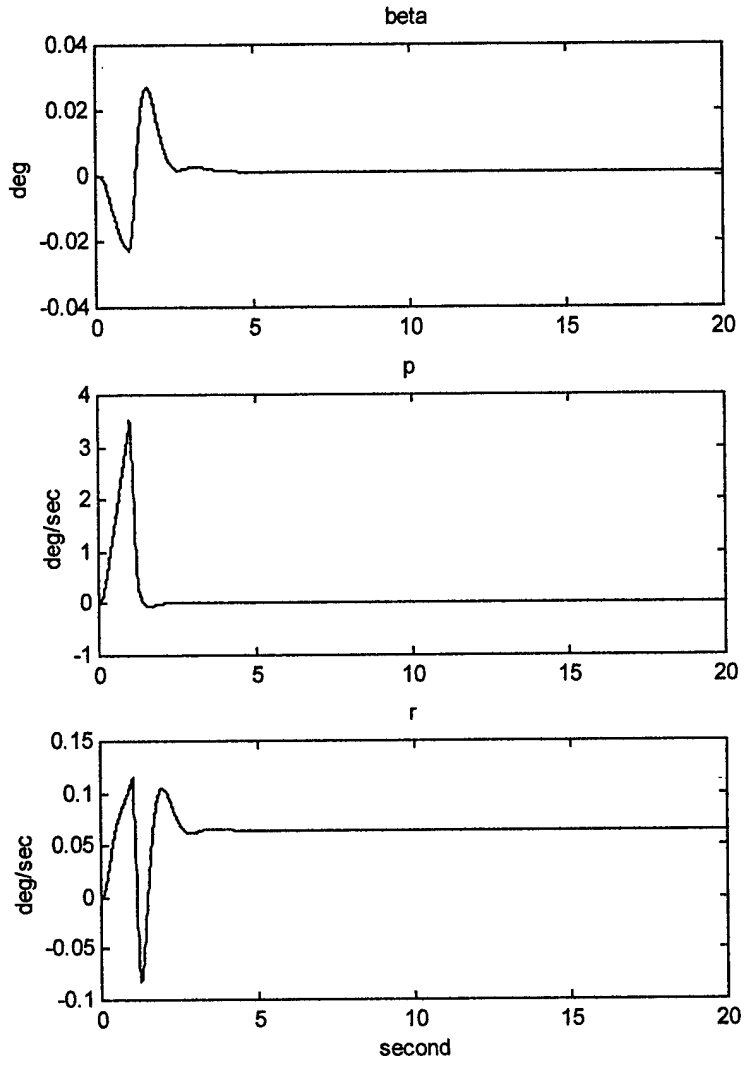

Figure 9.8 The F/A-18 RBF Response of the Modular RBF-ASE Control System

SECTION 10

CONCLUSIONS AND FUTURE WORK

We have successfully developed a reconfigurable adaptive control (RAC) system for flutter/aeroservoelasticity (ASE) instability suppression of battle-damaged aircraft and limit cycle oscillation (LCO) suppression of aircraft/store configurations.

With the F/A-18 as the baseline aircraft, rapid suppression of its critical-damage flutter and LCO (at 5.6 and 8.8 Hz) are successfully demonstrated through eight cases studied of numerical simulations including open-loop and closed-loop responses.

The developed RAC system is a modular control design in that the flutter/LCO control can be readily combined with the rigid-body flight (RBF) control, thereby minimizing the impact on the existing flight control system for retrofit.

The RAC system consists of a newly developed on-line modal parameter estimation (MPE) for system identification and on-line modified model-following reconfigurable (MMFR) algorithm for rapid flutter/LCO control (0.2 and 0.8 sec).

A massive screening technique using an expedient nonlinear unsteady transonic method (ZTAIC) to generate plant matrices permits efficient identification of critical damage cases of flutter/ASE instability. These plant matrices are validated through the correlation of the open-loop ASE analysis with flight test data.

Reduced-order state-space formulation using proper orthogonal decomposition (POD) and minimum state (MIST) methods reduce the system to seven states corresponding to three POD modes and one aerodynamic state. This allows the on-line algorithm to be operated efficiently within fractions of one second.

The number of sensor locations are minimized to two at the wing-tip for flutter/LCO control. With two additional existing sensors in the fuselage the system could operate adequately for LCO/ RBF dynamic control. Effective control surfaces for all cases studied are found to be the aileron and the trailing-edge flap.

The ZONA team's achievement of the Phase I objectives has paved the way and gained considerable technical insight for future development in real-time reconfigurable flight control. Consequently, it leads to a well-conceived plan for a Phase II development. The proposed tasks to be conducted in Phase II include:

System Definition – Prepare a simulation that contains:

- Rigid and flexible aircraft model of the F/A-18 that operates with the baseline F/A-18 control system.
- Provisions for additional aeroservoelastic (ASE) controller that operates in parallel with the primary F/A-18 controller.

Controller – Implement the Limit Cycle Oscillation (LCO) controller in the simulation, evaluate open loop (i.e., no commands to the aircraft) and closed loop response. Verify that the long term closed loop remains similar to the rigid-body F/A-18 model.

Application – Separate the controller into two design concepts:
- LCO controller for flight control using the F/A-18 sensors and control surfaces.
- FLUTTER controller using added sensors to the F/A-18 and the F/A-18 control surfaces.

Nonlinear Control Analysis – Add the flexible aircraft model to the F/A-18 six degree of freedom off-line simulation that contains all nonlinear terms such as actuator loading, control surface rates, 80 Hz software update, and Fleet Support Flight Control Computer (FSFCC). Implement the LCO and flutter controllers in the FSFCC with representative software size and sample rates. Evaluate the LCO controller in maneuver conditions and air turbulence.

Software Analysis – Determine how to implement the LCO controller in the FSFCC system. Conduct an analysis of the control architecture and projected software thru-put and timing requirements.

Flight Development Plan – Prepare a plan for flight test development of the LCO controller using a Navy F/A-18 test airplane equipped with the FSFCC system. Determine schedule and costs of the program.

Finally, ZONA and Boeing/St. Louis intend to accomplish the above tasks with close collaboration as an integral team in Phase II.

REFERENCES

1. Dornhein, M.A., "Elevon Vibration Leads to F-117 Crash," Aviation Week & Space Technology, Sep. 1997.

2. Denegri, C.M., "Limit Cycle Oscillation Flight Test Results of a Fighter with External Stores," AIAA-2000-1394.

3. Norton, William J., "Limit Cycle Oscillation and Flight Flutter Testing," Proceedings of the Society of Flight Test Engineers 21st Annual Symposium, Aug. 1990.

4. Chen, P.C., Sarhaddi, D. and Liu, D.D., "Limit-Cycle Oscillation Studies of a Fighter with External Stores," 39th Structures, Structural Dynamics and Materials Conference, AIAA-98-1727, Apr. 1998.

5. Denegri, C.M., "Correlation of Classical Flutter Analysis and Nonlinear Flutter Response Characteristics," International Forum of Aeroelasticity and Structural Dynamics, Rome, Italy, Jun. 17-20, 1997.

6. Chen, P.C., Lee, H.W., and Liu, D.D., "Unsteady Subsonic Aerodynamics for Bodies and Wings with External Stores including Wake Effect," Journal of Aircraft, Vol. 30, No. 5, Sept-Oct. 1993, pp. 618-628.

7. Chen, P.C., Sarhaddi, D., and Liu, D.D., "Transonic-Aerodynamic-Influence-Coefficient Approach for Aeroelastic and MDO Application," Journal of Aircraft, Vol. 37, No. 1, Jan-Feb. 2000, pp. 85-94.

8. Chen, P.C. and Liu, D.D., "Unsteady Supersonic Computations of Arbitrary Wing-Body Configurations Including External Stores," Journal of Aircraft, Vol. 27, No. 2, Feb 1990, pp. 108-116.

9. Liu, D.D., Yao, Z.X., Sarhaddi, D., and Chavez, F., "Piston Theory Revisited and Further Applications," Journal of Aircraft, Vol. 34, No. 3, May-Jun. 1997, pp. 304-312.

10. Chen, P.C., "A Damping Perturbation Method for Flutter Solution: The g-Method," paper presented at the Aerospace Flutter and Dynamics Council Meeting in AFRL/Wright-Patterson AFB, Oct. 15-16, 1998; also presented at the International Forum on Aeroelasticity and Structural Dynamics," Williamsburg, VA, Jun. 22-25, 1999. Also, to appear in AIAA Journal.

11. Karpel, M., "Design for Active Flutter Suppression and Gust Alleviation Using State-Space Aeroelastic Modeling," Journal of Aircraft, Vol. 19, No. 3, 1982, pp. 221-227.

12. Ward, D. and Barron, R., "Self-designing Flight Control Using Modified Sequential Least Squares Parameter Estimation and Optimal Receding Horizon Control Laws," Final Technical Report for AFOSR, Barron Associates, Inc., Mar. 1994.

13. Bobrow, J. and Murray, W., "An Algorithm for RLS Identification of Parameters that may Vary Quickly with Time," in IEEE Trans. on Automatic Control, Vol. 38, No. 2, Feb. 1993.

14. Gao, Z and Antsaklis, P.J., "Reconfigurable Control System Design via Perfect Model Following," International Journal of Control, Vol. 56, No. 4, 1992, pp. 783-798.

15. Morse, W.E. and Ossman, K.A., "Model Following Reconfigurable Flight Control System for the AFTI/F-16," Journal of Guidance, Control and Dynamics, Vol. 13, No. 6, 1990, pp. 969-976.

16. Chandler, P.R., Pachter, M., and Mears, M., "System Identification for Adaptive and Reconfigurable Control," Journal of Guidance, Control and Dynamics, Vol. 18, No. 3, 1995, pp. 516-524

17. Patton, J., "Fault Tolerant Control: the 1997 Situation (Survey)," Proceedings of IFAC SAFEPROCESS '97, IFAC, Hull, UK, 1997, pp. 1033-1055.

18. Bodson, M., and Pohlchuck, W.A., "Command Limiting in Reconfigurable light Control," Journal of Guidance, Control and Dynamics, Vol. 21, No. 4, 1998, pp. 639-646.

19. Krist, S.L., Biedron, R.T., and Rumsey, C.L., "CFL3D User's Manual Version 5.0," NASA Langley Research Center, Hampton, VA, Sept. 1997.

20. Hall, K.E., Thomas, J.P., and Dowell, E.H., "Reduced-Order Modeling of Unsteady Small-Disturbance Flows Using a Frequency-Domain Proper Orthogonal Decomposition Technique," 37th Aerospace Sciences Meeting and Exhibit, AIAA 99-0655, Jan. 1999.

21. Romanowski, M.C., "Reduced Order Unsteady Aerodynamic and Aeroelastic Models Using Karhunen-Loève Eigenmodes," AIAA Paper 96-3981, 1996.

22. Kim, T., "Frequency-Domain Karhunen- Loève Method and its Application to Linear Dynamic Systems," AIAA Journal, Vol. 36, No. 11, 1998, pp. 2117-2123.

23. Karpel, M., "Extension to the Minimum-State Aeroelastic Modeling Method," AIAA Journal, Vol. 29, No. 11, 1991, pp. 2007-2009.

24. Karpel, M., and Hoadley, S.T., "Physically Weighted Approximations of Unsteady Aerodynamic Forces Using the Minimum-State Method," NASA TP-3025, 1991.